UNIVERSITY OF OKLAHOMA

GRADUATE COLLEGE

On the Gravitational Lensing of Type Ia Supernovae

A DISSERTATION

SUBMITTED TO THE GRADUATE FACULTY

in partial fullfillment of the requirements for the

degree of

Doctor of Philosophy

By

Hamed Bagherpour
Norman, Oklahoma
2006

Downloaded from SHAREOK. Persistent Handle URL: https://hdl.handle.net/11244/1074

UMI Number: 3222153

UMI®

UMI Microform 3222153

Copyright 2006 by ProQuest Information and Learning Company.
All rights reserved. This microform edition is protected against
unauthorized copying under Title 17, United States Code.

ProQuest Information and Learning Company
300 North Zeeb Road
P.O. Box 1346
Ann Arbor, MI 48106-1346

On the Gravitational Lensing of Type Ia Supernovae

A DISSERTATION APPROVED FOR THE
DEPARTMENT OF PHYSICS AND ASTRONOMY

BY

Ronald Kantowski (Chair)

David Branch

Edward Baron

John Cowan

Patrick Skubic

Dee Fink

© Copyright by Hamed Bagherpour 2006
All Rights Reserved.

Preface

One of the consequences of Einstein's General Theory of Relativity is that light rays are deflected by gravity. Although this discovery was made the 20th century, the possibility that there could be such a deflection had been suspected much earlier, by Newton and Laplace among others. In 1804, Soldner calculated the magnitude of the deflection due to the Sun, assuming that light consists of material particles and using Newtonian gravity. Later in 1911, Einstein employed the equivalence principle to calculate the deflection angle and re-derived Soldner's formula.

Later in 1915, Einstein applied the full field equations of 'General Relativity' and discovered that the deflection angle is actually twice his previous result, the factor of two arising because of the curvature of the metric. According to this formula, a light ray which tangentially grazes the surface of the Sun is deflected by $1.7''$. Einstein's final result was confirmed in 1919 when the apparent angular shift of stars close to the limb of the Sun was measured during a total solar eclipse. The quantitative agreement between the measured shift and Einstein's prediction was immediately perceived as a compelling evidence in support of the theory of General Relativity. The deflection of light by massive bodies, and the phenomena resulting therefrom, are now referred to as *Gravitational Lensing*. The reader is refered to a very brief introduction on lensing in chapter 1.

Gravitational lensing has turned out to be an active field in astronomy, both as an abstract subject and a means to better understand and study other astronomical topics. One of the main applications of gravitational lensing is the broad field of supernovae observation. It is shown that lensing can have dramatic effects on how supernovae are observed, and therefore appear as an inevitable 'noise' in any (deep) survey carried out for purposes such as determining the equation of state for the so-called dark energy. In this dissertation we concentrate on some of these effects on the observation of type Ia supernovae.

In chapter 2, a description of the apparent light curves of microlensed SNe Ia as

extended and expanding sources is presented. It is shown that microlensing amplification can have significant effects on a small percentage of supernova observations. An uptodate model light curve is used to compare lensed and unlensed cases and we find that significant changes in shape can occur in some instances because of microlensing. The most significant effects occur when a distant supernova ($z \sim 1$) impacts well within the Einstein ring of a nearby microlens ($z \sim 0.05$). The effects of both the relative motion of the lens-SN and the atmospheric expansion are given and compared. The probability of observing such effects is discussed as well. This work is limited to spherically symmetric deflectors and indicate the quantitative effect of convergence caused by the lens's host galaxy.

A brief description of the deformed spectra of microlensed SNe Ia is presented in chapter 3. One can show that microlensing amplification can have significant effects on line profiles. The resonance-scattering code SYNOW is used to compute the intensity profile in the rest frame of the supernova. The observed (lensed) spectra are predicted assuming a simple stellar-size deflector, and are compared to unlensed cases to show what effects microlensing can have on spectral lines. Again, the work is limited to spherically symmetric deflectors.

The effects of ellipticity of matter distribution in massive halos on the observation of supernovae are presented in chapter 4. A pseudo elliptical Navarro-Frenk-White (NFW) mass model is used to calculate the introduced gain factors and observation rates of type Ia supernovae due to the strong lensing. It is investigated how and to what extent the ellipticity in mass distribution of the deflecting halos can affect surveys looking for cosmologically distant supernovae. Halo masses of $1.0\times10^{12}M_{\odot}h^{-1}$ and $1.0\times10^{14}M_{\odot}h^{-1}$ are used. The lensing halo are taken to be at redshifts $z_d = 0.2$, 0.5, and 1.0 with ellipticities of upto ϵ= 0.2.

Acknowlegement

I would like to thank my advisor Professor Ronald Kantowski who helped and supervised me all through my research. I am grateful to the members of my advisory committee, mainly professor David Branch for their time and the enlightening discussions I had with them. And last but not least, my deapest appreciations go to a great friend, Ines Cavero-Pelaez: she knows why she is being mentioned here!

Contents

1 Gravitational Lensing: An Astrophysical Tool **1**

1.1 Introduction 1

1.2 Effective Refractive Index of a Gravitational Field 2

1.3 Thin Screen Approximation 5

1.4 Lensing Geometry and Lens Equation 6

2 Light Curves of Microlensed Type Ia Supernovae **10**

2.1 Introduction 10

2.2 Light Curves of Type Ia Supernovae 11

2.3 Microlensing of Extended Sources 14

2.3.1 Basics 14

2.3.2 Amplification of an Extended Source 16

2.3.3 Probability 21

2.4 Microlensed Light Curves 24

2.4.1 Results 24

2.4.2 Observation Probability 34

2.5 Conclusion 35

3 Effects of Gravitational Microlensing on P-Cygni Profiles of Type Ia Supernovae **37**

3.1 Introduction 37

3.2 Microlensing of a Supernova as an Extended Source 38

3.2.1 Line Profiles of Type Ia Supernovae 38

3.2.2 Differential Amplification 41

3.3 Lensed Profiles 44

3.4 Conclusion 53

4 Gravitational Lensing of Type Ia Supernovae by Pseudo Elliptic NFW Halos **54**

4.1 Introduction 54

4.2 The NFW Halo Model Profile 56

4.2.1 NFW Haloes 56

4.2.2 Elliptical Potential Model 58

4.3 Gravitational Lensing: a Reminder 59

4.3.1 General Formalism 59

4.3.2 Lensing Parameters of Spherical NFW Model 60

4.3.3 Lensing Parameters of Pseudo Elliptical NFW Model 62

4.4 The Method 63

4.5 Results and Discussion 68

4.6 Conclusion 77

5 Last Words **78**

Bibliography **80**

A Probability of Distortion in a Lensed Light Curve **84**

B Lensing Equation for Elliptical NFW Haloes **87**

List of Figures

1.1 Light deflection by a prism. The refractive index $n > 1$ of the glass in the prism reduces the effective speed of light to c/n. This causes light rays to be bent around the thick end of the prism, as indicated. The dashed lines are wavefronts. 3

1.2 Light deflection by a point mass M. The unperturbed ray passes the mass at impact parameter b and is deflected by the angle $\hat{\alpha}$. Most of the deflection occurs within $\Delta z \sim \pm b$ of the point of closest approach. 4

1.3 A light ray which intersects the lens plane at $\vec{\xi}$ is deflected by an angle $\vec{\hat{\alpha}}(\vec{\xi})$. 6

1.4 Illustration of a gravitational lens system. The light ray propagates from the source S at transverse distance η from the optic axis to the observer O, passing the lens at transverse distance ξ. It is deflected by an angle $\hat{\alpha}$. The angular separations of the source and the image from the optic axis as seen by the observer are β and θ, respectively. 7

2.1 Model light curve of a supernova type Ia in its rest frame. Observed data of SN 1990N are added to show the fit. 13

2.2 Amplification curves of an extended source ($z_s = 1.0$) with a fixed radius of 178 AU (source frame), moving at 0.5 AU day^{-1} in the deflector plane ($z_d = 0.5$). The source reaches its closest approach (impact parameter) at $t = 0$. The figure shows five trajectories with different impact parameters, b (see Fig. 2.5). Here, the surface brightness and radius are assumed constant. 18

2.3 Normalized IDF profile calculated for SN Ia in U and B bands using W7 model (courtesy of Eric Lentz, University of Georgia), used to calculate the amplification curves of a supernova as an extended source with radius-dependent surface brightness. In this figure, a maximum expansion velocity of 30,000 km s^{-1} has been used to obtain the expansion velocity projected on the sky. The intensity profile used here is also presented for photospheric speeds of 13,000 km s^{-1} and 15,000 km s^{-1}. 20

2.4 Expansion speed (*upper panel*) and the radius (*lower panel*) of the photosphere of a type Ia supernova as a function of time in the source frame. 22

2.5 Geometry of the microlensing model used in § 4. 25

2.6 Alification curves (*lower panels*) and light curve (*upper panels*) of a supernova at $z_s = 1.0$, microlensed by a deflector at $z_d = 0.05$ with a mass of $m_d = 10^{-3}$ $M_\odot$ for two different lensing configurations (A and B). 26

2.7 Same as Fig. 2.6, with $m_d = 1$ $M_\odot$. 27

2.8 Same as Fig. 2.6, with $m_d = 10$ $M_\odot$. 28

2.9 This figure shows the light curves of a SN Ia (*left panels*) lensed by a moving deflector and a stationary deflector at redshift $z_d = 0.05$. The right panels show the magnitude difference of the two cases for a deflector with the same mass ($m_d = 10^{-3} M_\odot$) but at different redshifts. 31

2.10 Same as Fig. 2.9, with mass $m_d = 1 M_\odot$. 32

2.11 Same as Fig. 2.9, with mass $m_d = 10 M_\odot$. 33

3.1 Schematic view of a type Ia supernova as seen by an observer. The normalized radius P and planar speed V_r are shown. 38

3.2 Synthetic intensity profile of a type Ia supernova, showing absorption and emission features for $P < 1$, $P > 1$, and P just below 1 for $\tau = 1$ (upper panel) and $\tau = 1,000$ (lower panel). The emission feature in the upper panel is scaled up. 40
3.3 Amplification curves of any point on the projected source as a function of expansion velocity for different values of l. The value of photospheric expansion speed determines the zone (absorption or emission) with higher amplification. 43
3.4 Amplified line profile of sodium for $\tau = 1$ and $u_A = 0$. The deflector has a mass of $1M_\odot$. 46
3.5 Same as Fig. 3.4, with $\tau = 1$ and $u_A = 1/128$. 47
3.6 Same as Fig. 3.4, with $\tau = 1,000$ and $u_A = 0$. 48
3.7 Same as Fig. 3.4, with $\tau = 1,000$ and $u_A = 1/128$. 49
3.8 Amplified spectral lines of a SYNOW spectrum that resembles the maximum-light spectrum of a SN Ia, with $u_A = 0$ and $m_d = 1M_\odot$. . . 50
3.9 Same as Fig. 3.8, with $u_A = 1/128$. 51

4.1 Schematic picture of the lensing configuration by a deflecting halo. z_{halo} is the redshift of the halo and z_{limit} is the redshift corresponding to the limiting magnitude m_{limit}. The shaded area shows the volume where SNe are bright enough to be observed. 55
4.2 Multiple images produced by a $1.0\times10^{14}h^{-1}M_\odot$ halo with ellipticity $\epsilon = 0.1$. Dashed lines are the contours with constant surface density and the solid lines are the critical and caustic lines. Redshifts of deflector and source are 0.2 and 1.0, respectively (courtesy of Golse & Kneib). 64
4.3 Rates of type Ia supernovae per squared degree in intervalls of $\delta z = 0.05$. Dilution factor of $1 + z$ is taken into account (courtesy of Gunnarsson & Goobar). 65

4.4 This figure shows how the projected deflector is 'pixellated' in order to calculate the observable area behind the halo. Each pixel has dimensions of $\delta\omega \times \delta\omega$ with $\delta\omega$ being (smaller than) the angular resolution of the observation. 67

4.5 Rates of observed supernovae Ia per redshift bin $\delta_z = 0.05$ (upper panel), commulative rate (middle panel), and the lensing gain (lower panel) for a deflecting halo of mass $m_d = 1.0 \times 10^{12} h^{-1} M_\odot$ at redshifts of $z_d = 0.2$, 0.5, and 1.0 with ellipticities $\epsilon = 0.1$ and 0.2. 69

4.6 Same as Figure 5, with $m_d = 1.0 \times 10^{14} M_\odot h^{-1}$. 70

4.7 In this figure the 3 upper panels show observed rates of lensed (solid line) and unlensed (dash line) for three different ellipticies $\epsilon = 0.0$, 0.1, and 0.2. The deflecting halo has a mass of $m_d = 1.0 \times 10^{12} h^{-1} M_\odot$ and is located at redshift $z_s = 0.5$. The lowermost panel depicts the relative difference of $\epsilon = 0.1$ (solid line) and $\epsilon = 0.2$ (dash line) with respect to $\epsilon = 0.0$. 72

4.8 Same as Figure 7, with $m_d = 1.0 \times 10^{14} M_\odot h^{-1}$. 73

4.9 Rates of observed supernovae Ia as a function of survey magnitude limit m (upper panel). Results are shown for halo masses $m_d = 1.0 \times 10^{12} h^{-1} M_\odot$ and $m_d = 1.0 \times 10^{14} h^{-1} M_\odot$ with ellipticities $\epsilon = 0.1$ and 0.2. The halo is at redshift $z_d = 0.2$. The relative difference of cases with $\epsilon = 0.1$ and 0.2 with respect to $\epsilon = 0.0$ is given in the lower panel. 74

4.10 Same as Fig. 9 with $z_d = 0.5$. 75

4.11 Same as Fig. 9 with $z_d = 1.0$. 76

A.1 Area on the deflector plane within which a microlens would be close enough to a luminous SNe Ia to cause significant changes in its lightcurve. 85

List of Tables

4.1 NFW halo parameters for the two halo masses m_d at the given redshifts z_d used in this chapter. 66

Chapter 1

Gravitational Lensing: An Astrophysical Tool

1.1 Introduction

The propagation of light in arbitrary curved spacetimes is in general a complicated theoretical problem. However, for almost all cases of relevance to gravitational lensing, we can assume that the overall geometry of the universe is well described by the Friedmann-Lemaître-Robertson-Walker metric and that the matter inhomogeneities which cause the lensing are no more than local perturbations. Light paths propagating from the source past the lens to the observer can then be broken up into three distinct zones. In the first zone, light travels from the source to a point close to the lens through unperturbed spacetime. In the second zone, near the lens, light is deflected. Finally, in the third zone, light again travels through unperturbed spacetime. To study light deflection close to the lens, we can assume a locally flat, Minkowskian spacetime which is weakly perturbed by the Newtonian gravitational potential of the mass distribution constituting the lens. This approach is legitimate if the Newtonian potential Φ is small, $|\Phi| \ll c^2$, and if the peculiar velocity v of the lens is small, $v \ll c$.

These conditions are satisfied in virtually all cases of astrophysical interest. Consider for instance a galaxy cluster at redshift ~ 0.3 which deflects light from a source at redshift ~ 1. The distances from the source to the lens and from the lens to the observer are ~ 1 Gpc, or about three orders of magnitude larger than the diameter of the cluster. Thus zone 2 is limited to a small local segment of the total light path. The relative peculiar velocities in a galaxy cluster are $\sim 10^3$ km s^{-1} $\ll c$, and the Newtonian potential is $|\Phi| < 10^{-4}\, c^2 \ll c^2$, in agreement with the conditions stated above.

1.2 Effective Refractive Index of a Gravitational Field

In view of the simplifications just discussed, we can describe light propagation close to gravitational lenses in a locally Minkowskian spacetime perturbed by the gravitational potential of the lens to first post-Newtonian order. The effect of spacetime curvature on the light paths can then be expressed in terms of an effective index of refraction n, which is given by Schneider, Ehlers, & Falco (1992)

$$n = 1 - \frac{2}{c^2}\,\Phi = 1 + \frac{2}{c^2}\,|\Phi| \; . \tag{1.1}$$

Note that the Newtonian potential is negative if it is defined such that it approaches zero at infinity. As in normal geometrical optics, a refractive index $n > 1$ implies that light travels slower than in free vacuum. Thus, the effective speed of a ray of light in a gravitational field is

$$v = \frac{c}{n} \simeq c - \frac{2}{c}\,|\Phi| \; . \tag{1.2}$$

Figure 1.1 shows the deflection of light by a glass prism. The speed of light is reduced inside the prism. This reduction of speed causes a delay in the arrival time of a signal through the prism relative to another signal traveling at speed c. In addition, it causes wavefronts to tilt as light propagates from one medium to another, leading to a bending of the light ray around the thick end of the prism.

The same effects are seen in gravitational lensing. Because the effective speed of light is reduced in a gravitational field, light rays are delayed relative to propagation in vacuum. The total time delay Δt is obtained by integrating over the light path from the observer to the source:

$$\Delta t = \int_{\text{source}}^{\text{observer}} \frac{2}{c^3}\,|\Phi|\,dl \; . \tag{1.3}$$

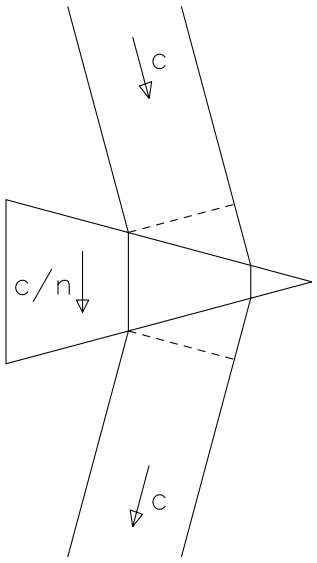


Figure 1.1: Light deflection by a prism. The refractive index $n > 1$ of the glass in the prism reduces the effective speed of light to c/n. This causes light rays to be bent around the thick end of the prism, as indicated. The dashed lines are wavefronts.

This is called the Shapiro delay (Shapiro, 1964).

As in the case of the prism, light rays are deflected when they pass through a gravitational field. The deflection is the integral along the light path of the gradient of n perpendicular to the light path, i.e.

$$\vec{\hat{\alpha}} = -\int \vec{\nabla}_\perp n \, dl = \frac{2}{c^2} \int \vec{\nabla}_\perp \Phi \, dl \; . \tag{1.4}$$

In all cases of interest the deflection angle is very small. We can therefore simplify the computation of the deflection angle considerably if we integrate $\vec{\nabla}_\perp n$ not along the deflected ray, but along an unperturbed light ray with the same impact parameter. (As an aside we note that while the procedure is straightforward with a single lens, some care is needed in the case of multiple lenses at different distances from the source. With multiple lenses, one takes the unperturbed ray from the source as the reference trajectory for calculating the deflection by the first lens, the deflected ray from the first lens as the reference unperturbed ray for calculating the deflection by the second lens, and so on.)

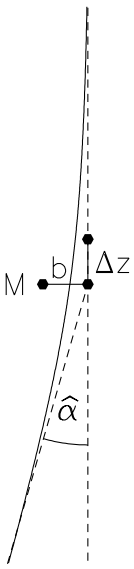


Figure 1.2: Light deflection by a point mass M. The unperturbed ray passes the mass at impact parameter b and is deflected by the angle $\hat{\alpha}$. Most of the deflection occurs within $\Delta z \sim \pm b$ of the point of closest approach.

As an example, we evaluate the deflection angle of a point mass M (Fig. 1.2). The Newtonian potential of the lens is

$$\Phi(b, z) = -\frac{GM}{(b^2 + z^2)^{1/2}} \, , \tag{1.5}$$

where b is the impact parameter of the unperturbed light ray, and z indicates distance along the unperturbed light ray from the point of closest approach. We therefore have

$$\vec{\nabla}_\perp \Phi(b, z) = \frac{GM\,\vec{b}}{(b^2 + z^2)^{3/2}} \, , \tag{1.6}$$

where $\vec{b}$ is orthogonal to the unperturbed ray and points toward the point mass. Equation (1.6) then yields the deflection angle

$$\hat{\alpha} = \frac{2}{c^2} \int \vec{\nabla}_\perp \Phi \, dz = \frac{4GM}{c^2 b} \, . \tag{1.7}$$

Note that the Schwarzschild radius of a point mass is

$$R_{\rm S} = \frac{2GM}{c^2} \, , \tag{1.8}$$

so that the deflection angle is simply twice the inverse of the impact parameter in units of the Schwarzschild radius. As an example, the Schwarzschild radius of the Sun is 2.95 km, and the solar radius is 6.96×10^5 km. A light ray grazing the limb of the Sun is therefore deflected by an angle $(5.9/7.0) \times 10^{-5}$ radians $=1.7''$.

1.3 Thin Screen Approximation

Figure 1.2 illustrates that most of the light deflection occurs within $\Delta z \sim \pm b$ of the point of closest encounter between the light ray and the point mass. This Δz is typically much smaller than the distances between observer and lens and between lens and source. The lens can therefore be considered thin compared to the total extent of the light path. The mass distribution of the lens can then be projected along the line-of-sight and be replaced by a mass sheet orthogonal to the line-of-sight. The plane of the mass sheet is commonly called the lens plane. The mass sheet is characterized by its surface mass density

$$\Sigma(\vec{\xi}) = \int \rho(\vec{\xi}, z) \, dz \, , \tag{1.9}$$

where $\vec{\xi}$ is a two-dimensional vector in the lens plane. The deflection angle at position $\vec{\xi}$ is the sum of the deflections due to all the mass elements in the plane:

$$\vec{\hat{\alpha}}(\vec{\xi}) = \frac{4G}{c^2} \int \frac{(\vec{\xi} - \vec{\xi}')\Sigma(\vec{\xi}')}{|\vec{\xi} - \vec{\xi}'|^2} \, d^2\xi' \, . \tag{1.10}$$

Figure 1.3 illustrates the situation.

In general, the deflection angle is a two-component vector. In the special case of a circularly symmetric lens, we can shift the coordinate origin to the center of symmetry and reduce light deflection to a one-dimensional problem. The deflection

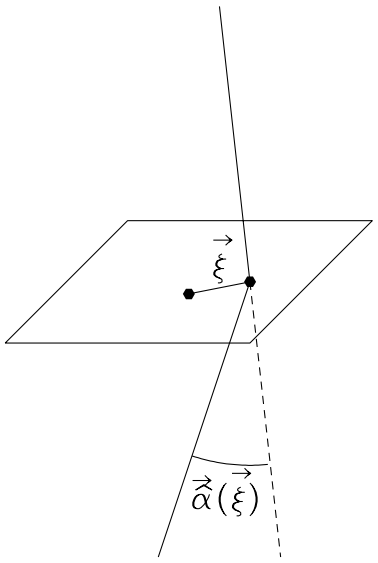


Figure 1.3: A light ray which intersects the lens plane at $\vec{\xi}$ is deflected by an angle $\vec{\hat{\alpha}}(\vec{\xi})$.

angle then points toward the center of symmetry, and its modulus is

$$\hat{\alpha}(\xi) = \frac{4GM(\xi)}{c^2\xi} \ , \tag{1.11}$$

where ξ is the distance from the lens center and $M(\xi)$ is the mass enclosed within radius ξ,

$$M(\xi) = 2\pi \int_0^{\xi} \Sigma(\xi')\xi' \, d\xi' \ . \tag{1.12}$$

1.4 Lensing Geometry and Lens Equation

The geometry of a typical gravitational lens system is shown in Figure 1.4. A light ray from a source S is deflected by the angle $\vec{\hat{\alpha}}$ at the lens and reaches an observer O. The angle between the (arbitrarily chosen) optic axis and the true source position is $\vec{\beta}$, and the angle between the optic axis and the image I is $\vec{\theta}$. The (angular diameter) distances between observer and lens, lens and source, and observer and source are $D_{\rm d}$, $D_{\rm ds}$, and $D_{\rm s}$, respectively.

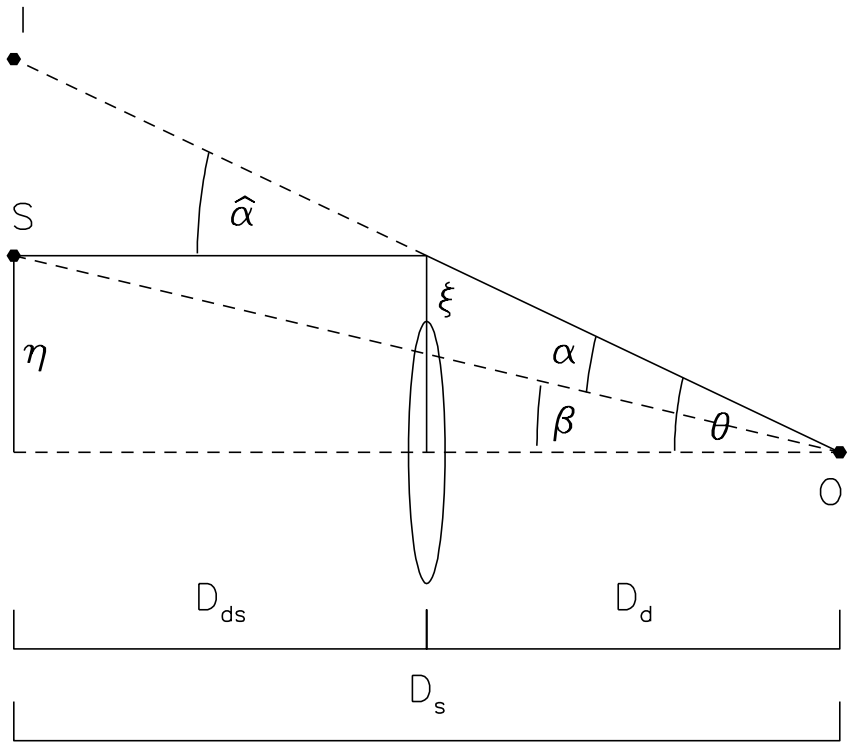


Figure 1.4: Illustration of a gravitational lens system. The light ray propagates from the source S at transverse distance η from the optic axis to the observer O, passing the lens at transverse distance ξ. It is deflected by an angle $\hat{\alpha}$. The angular separations of the source and the image from the optic axis as seen by the observer are β and θ, respectively.

It is convenient to introduce the reduced deflection angle

$$\vec{\alpha} = \frac{D_{\rm ds}}{D_{\rm s}}\,\hat{\vec{\alpha}}\ . \tag{1.13}$$

From Figure 1.4 we see that $\theta D_{\rm s} = \beta D_{\rm s} - \hat{\alpha} D_{\rm ds}$. Therefore, the positions of the source and the image are related through the simple equation

$$\vec{\beta} = \vec{\theta} - \vec{\alpha}(\vec{\theta})\ . \tag{1.14}$$

Equation (1.14) is called the *lens equation*, or ray-tracing equation. It is nonlinear in the general case, and so it is possible to have multiple images $\vec{\theta}$ corresponding to a single source position $\vec{\beta}$. As Fig. 1.4 shows, the lens equation is trivial to derive and requires merely that the following Euclidean relation should exist between the angle enclosed by two lines and their separation,

$$\text{separation} = \text{angle} \times \text{distance}\ . \tag{1.15}$$

It is not obvious that the same relation should also hold in curved spacetimes. However, if the distances $D_{\rm d,s,ds}$ are *defined* such that eq. (1.15) holds, then the lens equation must obviously be true. Distances so defined are called angular-diameter distances, and eqs. (1.13), (1.14) are valid only when these distances are used. Note that in general $D_{\rm ds} \neq D_{\rm s} - D_{\rm d}$.

As an instructive special case consider a lens with a constant surface-mass density. From eq. (1.11), the (reduced) deflection angle is

$$\alpha(\theta) = \frac{D_{\rm ds}}{D_{\rm s}}\,\frac{4G}{c^2\xi}\,(\Sigma\pi\xi^2) = \frac{4\pi G\,\Sigma}{c^2}\,\frac{D_{\rm d}D_{\rm ds}}{D_{\rm s}}\,\theta\ , \tag{1.16}$$

where we have set $\xi = D_{\rm d}\theta$. In this case, the lens equation is linear; that is, $\beta \propto \theta$.

Let us define a critical surface-mass density

$$\Sigma_{\rm cr} = \frac{c^2}{4\pi G}\,\frac{D_{\rm s}}{D_{\rm d} D_{\rm ds}} = 0.35\,{\rm g\,cm^{-2}}\,\left(\frac{D}{1\,{\rm Gpc}}\right)^{-1}\,, \tag{1.17}$$

where the effective distance D is defined as the combination of distances

$$D = \frac{D_{\rm d} D_{\rm ds}}{D_{\rm s}}\,. \tag{1.18}$$

For a lens with a constant surface mass density $\Sigma_{\rm cr}$, the deflection angle is $\alpha(\theta) = \theta$, and so $\beta = 0$ for all θ. Such a lens focuses perfectly, with a well-defined focal length. A typical gravitational lens, however, behaves quite differently. Light rays which pass the lens at different impact parameters cross the optic axis at different distances behind the lens. Considered as an optical device, a gravitational lens therefore has almost all aberrations one can think of. However, it does not have any chromatic aberration because the geometry of light paths is independent of wavelength.

A lens which has $\Sigma > \Sigma_{\rm cr}$ somewhere within it is referred to as being *supercritical*. Usually, multiple imaging occurs only if the lens is supercritical, but there are exceptions to this rule. See, for example, Subramanian & Cowling (1986).

Throughout the following chapters, more theoretical aspects of gravitational lensing employed for our calculations will be presented.

Chapter 2

Light Curves of Microlensed Type Ia Supernovae

2.1 Introduction

Out of a number of distance indicators, supernovae have emerged as the most promising standard candles. Due to their significant intrinsic brightness and relative ubiquity they can be observed in the local and distant universe. Several teams including the High-z Supernova Search (Schmidt et al., 1998) and the Supernova Cosmology Project (Perlmutter et al., 1999) have been searching for supernovae at higher redshifts since the early 1990's. Light emitted from these 'standard candles' is subject to lensing by intervening objects while traversing the large distances involved (Kantowski, Vaughan, & Branch, 1995); the further the light source, the higher its chance of being significantly lensed. In fact, for cosmologically distant sources, the probability is high that a distant point source will be 'imaged' (Press & Gunn, 1973; Bourassa & Kantowski, 1976; Wyithe & Turner, 2002), particularly by stellar-size objects (microlensing). While the systematic errors introduced by K-correction, selection effects, and possible evolution can be removed, lensing might ultimately limit the accuracy of luminosity distance measurements (Perlmutter & Schmidt, 2003). Only a large sample of SNe at each redshift can be used to characterize the lensing distribution and to correct for the effect of lensing.

Properties of microlensed supernovae have been studied previously. Schneider & Wagoner (1987) presented the time-dependent amplification of supernovae caused by the expansion of the photosphere, and showed that the related polarization of a supernova is not likely to exceed 1%. For cosmologically distant supernovae a 1% effect is practically impossible to detect at this time. Linder, Schneider, & Wagoner

(1988) studied amplification of supernovae and developed approximate formulae for the amplification probability distribution. Rauch (1991) studied microlensing of SNe Ia by compact objects and calculated the resulting amplification probability distributions using Monte Carlo simulations. Kolatt & Bartelmann (1998) performed a non-detailed investigation on the light curves of type Ia supernovae microlensed by intracluster MACHO's assuming the point-deflector (with shear) model of Chang-Refsdal (Chang & Refsdal, 1984).

In this chapter, we demonstrate how microlensing by a single stellar-size deflector can affect light curves of cosmologically distant SNe Ia. We use the simple Schwarzschild lens model to calculate amplifications. We ignore the additional amplification caused by the macrolensing introduced by the hosting galaxy, and concentrate on the time dependent effects caused by a single moving stellar-size deflector. We model the SNe Ia by expanding light sources with realistic radial surface intensity profiles.

In the next section, we present a model light curve for type Ia supernovae. § 3 is devoted to a brief review of the gravitational lensing effect, and in § 4 we present the results of our calculations. Throughout, we assume a flat Friedmann-Lamaître-Robertson-Walker cosmological model with $\Omega_m = 0.3$, $\Omega_\Lambda = 0.7$, and $h_{100} = 0.67$ to calculate the distances to the source and deflector.

2.2 Light Curves of Type Ia Supernovae

In general, spectacular supernovae explosions can be interpreted in terms of two concepts (Arnett, 1996): A shock wave running through a stellar envelope, and the radioactive decay of newly synthesized ^{56}Ni to ^{56}Co and then to ^{56}Fe. The nature of the explosion is the expansion away from the region of energy release. The explosion becomes more spherically symmetric with time, trending toward a small-scale Hubble type flow.

In the meantime, various aspects of the event including shock emergence, radiative diffusion, heating, and recombination determine the evolution of the luminosity, i.e., the light curve, which is usually exhibited as the absolute magnitude as a function of time. In the case of SNe Ia, it is the shape of the light curve that can be used to measure cosmological parameters such as Hubble constant; see, for instance, Riess, Press, & Kirshner (1995).

To model the intrinsic Type Ia supernova light curve we used a combination of two existing analytical models; for the peak of the light curve (early time) we used the model of Arnett (1982) while for the tail of the light curve (late time) we used the deposition function described by Jeffery (1999). The basic assumptions made in this model are:

1. a homologous expansion of the photosphere
2. radiation pressure dominates at early times
3. the diffusion approximation is valid at early times
4. the optical opacity is constant for the light curve peak and the gamma-ray opacity is constant for the tail
5. ^{56}Ni is present in the ejecta and its distribution is peaked toward the center of the ejected mass at small initial radius.

The details of this combined model are given by Richardson, Branch, & Baron (2005). The model parameters have been fixed for a typical SN Ia: the kinetic energy is 1 foe (10^{51} erg), the total ejected mass is 1.4 $M_\odot$, and the ^{56}Ni mass has been set to 0.6 $M_\odot$. These values produce a SN Ia with a peak absolute magnitude of about -19.5.

To test the model we varied the kinetic energy, nickel mass, and the rise time until we achieved the best χ^2 fit to the observed data of a few SNe Ia. The model worked well as can be seen in Figure 2.1, where the fit of SN1990N is shown with $E_k = 0.60$ foe, $M_{Ni} = 0.62$ $M_\odot$, $t_{rise} = 21$ days, and the reduced $\chi^2 = 0.43$. We use

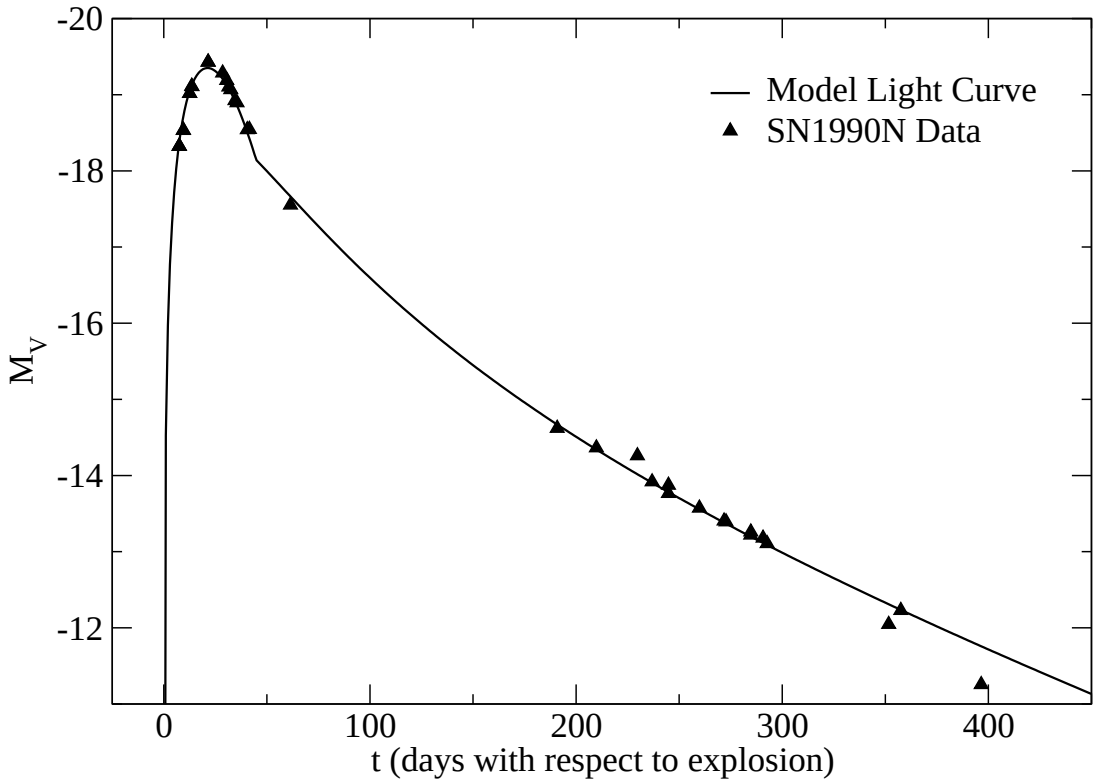


Figure 2.1: Model light curve of a supernova type Ia in its rest frame. Observed data of SN 1990N are added to show the fit.

this supernova because it was well observed (the light curve had good coverage) and it is photometrically characteristic of most SNe Ia. It should be mentioned that in this paper, the model light curve is merely serving as an interpolation device.

2.3 Microlensing of Extended Sources

2.3.1 Basics

The linearized Einstein theory for a static gravitational field gives a bending angle for light rays passing through a weak gravitational field of

$$\boldsymbol{\alpha} = -\frac{2}{c}\int_{-\infty}^{+\infty} \boldsymbol{\nabla}\phi \, dt \,, \tag{2.1}$$

where ϕ is the Newtonian gravitational potential satisfying the boundary conditions $\phi \to 0$ at infinity, and where the integral is performed along the light path in the absence of the gravitational field. Bourassa, Kantowski, & Norton (1973), and Bourassa & Kantowski (1974, 1976) used the 2-component nature of $\boldsymbol{\alpha}$ to replace it with the complex scattering function $I(z)$, where $z = x + iy$ is the complex equivalent of the 2-d vector $\mathbf{r} = x\hat{\imath} + y\hat{\jmath}$. Using $I(z)$, the relation between the source position, z, and image position, z_o, when both are projected onto the plane of the deflector (also called the sky plane) is

$$z = z_o - \frac{4GD}{c^2} I^*(z_o) \,. \tag{2.2}$$

The scaled (effective) distance D is defined as $D = D_{ds}D_d/D_s$, where the deflector-source distance, D_{ds}, the observer-deflector distance, D_d, and the observer-source distance, D_s, are all the same type distances, e.g., apparent size distances.

In the case of a point deflector (on which we focus here), the scattering function takes a very simple form:

$$I(z_o) = \frac{m_d}{z_o} \,, \tag{2.3}$$

and the equation (2.2) reduces to

$$z = z_o - \frac{r_E^2}{z_o^*}\,, \tag{2.4}$$

where $r_E \equiv \sqrt{4Gm_d D\, c^{-2}} = \sqrt{2r_S D}$ is the Einstein ring radius, and r_S is the deflector's Schwarzschild radius. This equation has two separate solutions (images) for any source position $r = |z|$,

$$r_\pm = |z_\pm| = \frac{1}{2}\left(\sqrt{r^2 + 4r_E^2} \pm r\right)\,. \tag{2.5}$$

Both images are in line with source and deflector. The 'primary' image, r_+, lies on the same side of the deflector while the 'secondary' image, r_-, is on the other side. In the case of microlensing, the angular separation of the two images is of the order of micro arcseconds. Consequently, the two images are seen as a single object (§ 3.2). The Einstein ring occurs when source and deflector are aligned with the observer ($r = |z| = 0$) for which $r_+ = r_- = r_E$, and due to the symmetry of the lensing configuration the image is actually a ring.

The effect of gravitational lensing on the apparent brightness of a distant source can be computed in various ways. For extended sources like supernovae it is best to employ the fact that the apparent brightness is proportional to the image's apparent area, meaning that the brightness of a source is amplified by a factor A:

$$A = \frac{\mathcal{A}_o}{\mathcal{A}}\,, \tag{2.6}$$

where $\mathcal{A}_o$ is the area of the image and $\mathcal{A}$ is the area of the source both projected on the deflector plane. For a point mass deflector and a small point-like source the combined amplification of the unresolved primary and secondary images is

$$A \equiv A_+ + A_- = \frac{r^2 + 2r_E^2}{r\sqrt{r^2 + 4r_E^2}}\,. \tag{2.7}$$

If the source is not small, i.e., if r/r_E varies significantly across the source, differential amplification must be taken into account. Measuring this amplification from a single observation is not possible since it is practically impossible to figure out the original source flux. However, if the luminosity of the source varies with time in a predictable way as with SNe or if the source is of constant brightness and the lens is moving with respect to the line of sight to the source (as with observation of bulge stars; see, for instance, Sumi et al. (2004)), the amplification will change with time in a predictable way and it is possible to determine the amplification.

2.3.2 Amplification of an Extended Source

As implied in the last section, to obtain the total flux received from an extended source, an integral of intensity across the source may be required:

$$A = \frac{\int_{image} I \, d\mathcal{A}_o}{\int_{source} I \, d\mathcal{A}} \, . \tag{2.8}$$

If the surface brightness is constant across the source or if there is no differential amplification, the net amplification is simply given by equation (2.6), where $\mathcal{A}_o$ can be the primary, secondary, or total image area, giving respectively the primary, secondary, or total amplification. In the case of a circular extended source with a projected radius of a at a distance l from the center of a spherically symmetric deflector (a and l are measured in the deflector plane), the total area of the combined and unresolvable images is

$$\mathcal{A}^{(total)} = \int_{-\frac{\pi}{2}}^{\frac{\pi}{2}} a \left(a + l \, \sin\varphi\right) \sqrt{1 + \frac{4r_E^2}{l^2 + a^2 + 2al \, \sin\varphi}} d\varphi \tag{2.9}$$

After a rather long calculation, the total amplification of a uniform disc is found to be

$$A_{disc}[a, \, l, \, r_E] = \eta \left\{ \mu_1 K\left(k\right) + \mu_2 E\left(k\right) + \mu_3 \Pi\left(n, \, k\right) \right\} \, , \tag{2.10}$$

(Witt & Mao, 1994; Mao & Witt, 1998),where K, E, and Π are respectively the first, second, and third complete elliptic integral with

$$k = \frac{16alr_E^2}{(l+a)^2\left((l-a)^2+4r_E^2\right)}\,,$$

$$n = \frac{4al}{(a+l)^2}\,,$$

and constants

$$\eta = \frac{1}{2\pi a^2\sqrt{(l-a)^2+4r_E^2}}\,,$$

$$\mu_1 = (l-a)\left(a^2-l^2-8r_E^2\right)\,,$$

$$\mu_2 = (l+a)\left((l-a)^2+4r_E^2\right)\,,$$

$$\mu_3 = \frac{4\,(l-a)^2\,(a^2+r_E^2)}{l+a}\,.$$

Figure 2.2 is a plot of the amplification curves of an extended source moving with speed 0.5 AU per day (1 AU day^{-1} $\simeq 1.73\times10^3$ km s^{-1}) with respect to a deflector of mass 1 $M_\odot$. To illustrate the combined effect of relative motion and finite size on amplification, in Figure 2.2 we have assumed a constant surface brightness across the source (no limb darkening) and a fixed radius of 178 AU (source frame) at redshift $z_s = 1.0$, corresponding to that of a supernova with a constant atmospheric speed of 30,000 kilometer per second at eighteen days after the explosion. In this figure, the source approaches the deflector ($z_d = 0.5$) with various impact parameters (closest approach), producing different amplification curves.

In what follows we use a more realistic supernova model to calculate amplification curves. We assume a ring-like structure for the intensity I of a spherically expanding photosphere like that of a SN Ia (Höflich, 1990). To model the 2-dimensional brightness profile across the source we assume that the emissivity of light coming from any

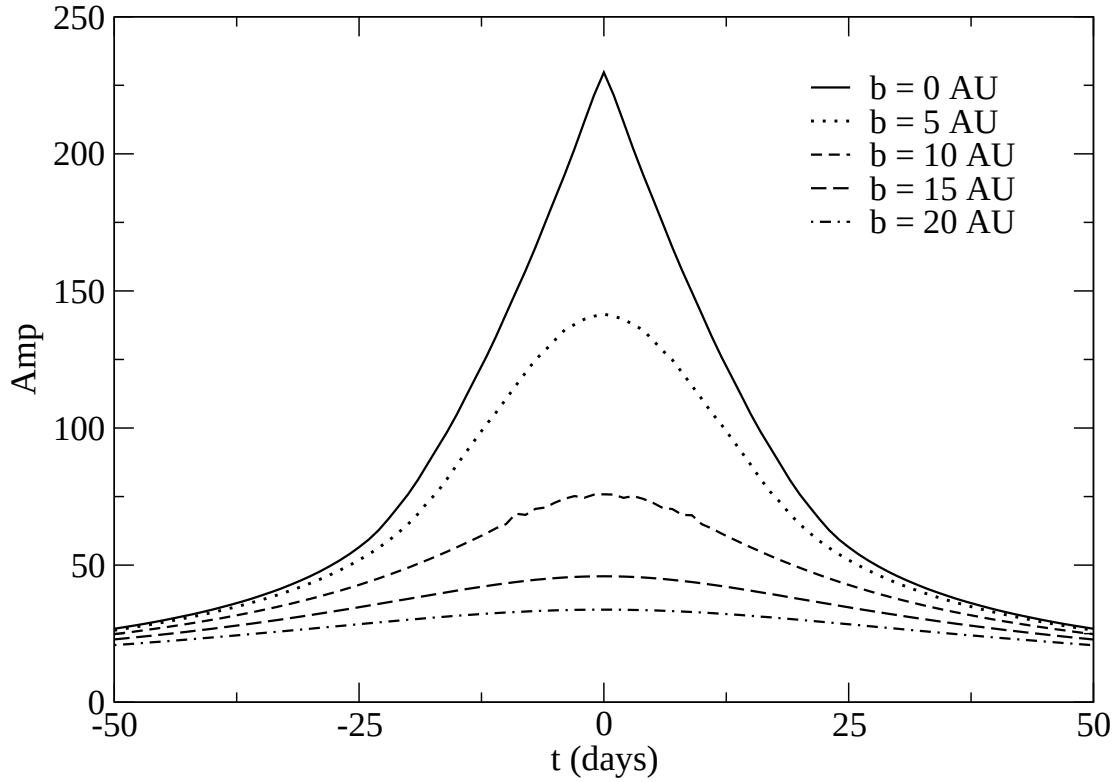


Figure 2.2: Amplification curves of an extended source ($z_s = 1.0$) with a fixed radius of 178 AU (source frame), moving at 0.5 AU day^{-1} in the deflector plane ($z_d = 0.5$). The source reaches its closest approach (impact parameter) at $t = 0$. The figure shows five trajectories with different impact parameters, b (see Fig. 2.5). Here, the surface brightness and radius are assumed constant.

volume element in the photosphere of a type Ia supernova is constant and find

$$I(r) = I_o \sqrt{1 - \left(\frac{r}{r_{ph}}\right)^2}\,, \tag{2.11}$$

where I_o is the intensity at the center and r_{ph} is the radius of the photosphere. This profile is in agreement with one of the commonly used family of limb-darkening profiles (Allen, 1973; Claret, Díaz-Corovés, & Gimémez, 1995). The assumption that emissivity per volume in SNe Ia is constant is a reasonable assumption during the nebular phase ($t > 150$ days). To see whether the obtained intensity profile is also applicable to photospheric phase ($t < 150$ days) we compared it to a normalized intensity distribution function (IDF) calculated using W7 model (Nomoto, Thielemann, & Yokoi, 1984) for SNe type Ia in U and B bands (courtesy of E. Lentz). The result of this IDF calculation as well as our intensity profile can be seen in Figure 2.3.

The amplification of a thin ring of radius a can be computed using Eq. (10) as

$$A_{ring}\left(a, l, r_E\right) = \frac{1}{2\pi a}\frac{d}{da}\left[\pi a^2 A_{disc}\left(a, l, r_E\right)\right]\,, \tag{2.12}$$

and the net amplification for a limb-darkened source where photospheric radius is r_{ph} as

$$A_I\left(r_{ph}, l, r_E\right) = \frac{-\int_0^{r_{ph}} \frac{d}{da}\left[I(a)\right]\pi a^2 A_{disc}\left(a, l, r_E\right) da}{\int_0^{r_{ph}} I(a) 2\pi a da}\,. \tag{2.13}$$

For the intensity profile $I(r)$ given in Eq. (2.11), A_I simplifies to:

$$A_I\left(r_{ph}, l, r_E\right) = \frac{3}{2}\int_0^{\pi/2} \sin^3\varphi\, A_{disc}[r_{ph}\sin\varphi,\, l,\, r_E]\, d\varphi \tag{2.14}$$

where A_{disc} is the function introduced in Eq. (2.10).

We also estimated the characteristic radius of the optical image of a type Ia supernova as a function of time. For the photospheric phase, we assumed homologous expansion ($r = vt$) and obtained the radius of the photosphere as a function of time since explosion by integrating the speed at the photosphere, as determined empirically

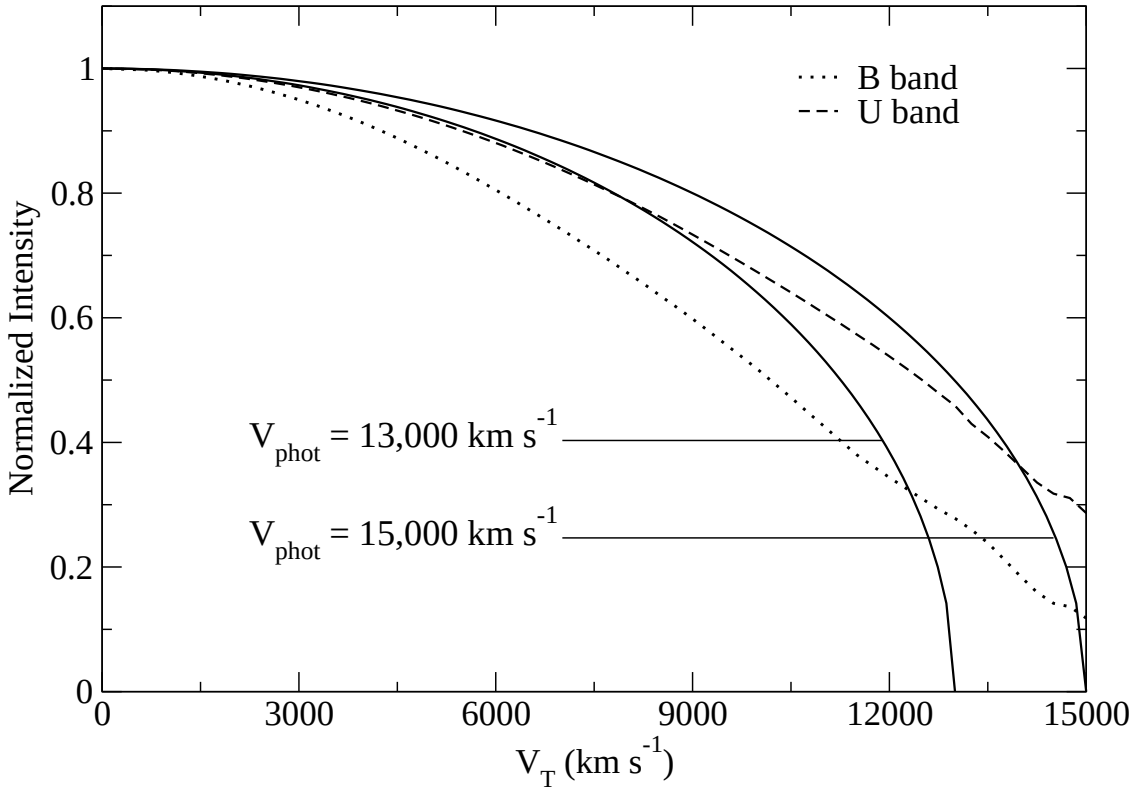


Figure 2.3: Normalized IDF profile calculated for SN Ia in U and B bands using W7 model (courtesy of Eric Lentz, University of Georgia), used to calculate the amplification curves of a supernova as an extended source with radius-dependent surface brightness. In this figure, a maximum expansion velocity of 30,000 km s^{-1} has been used to obtain the expansion velocity projected on the sky. The intensity profile used here is also presented for photospheric speeds of 13,000 km s^{-1} and 15,000 km s^{-1}.

by Branch et al. (2005). For the nebular phase, we assumed that the radius of the iron–group core expands at a constant velocity of 6000 km s^{-1}. A good fit for the speed is an exponential:

$$v(t) = 9.1\, e^{(-t/36.5\,\mathrm{days})} + 6.0\,, \tag{2.15}$$

in units of 10^3 km s^{-1}, from which the photospheric radius in AU is given by:

$$r_{ph}(t) = 190\,(1 - e^{(-t/36.5\,\mathrm{days})}) + 3.5\,t\,. \tag{2.16}$$

Figure 2.4 shows the expansion velocity as well as the radius as a function of time.

2.3.3 Probability

The relevant quantity in seeing a microlensing event is the optical depth τ. It is defined as the probability that a point source (or equivalently the center of an extended source) falls inside the Einstein ring of some deflector. The brightness of a point source within r_E is amplified by a factor of at least 1.34. For randomly located point deflectors the optical depth depends on the mass density of the deflectors and not on their number density (Press & Gunn, 1973).

Typical values of the optical depths for microlensing of nearby luminous sources are remarkably small. For instance, Sumi et al. (2003) calculated an optical depth $\tau = 2.59^{+0.84}_{-0.64} \times 10^{-6}$ toward the Galactic Bulge (GB) in Baade's window for events with time scales between 0.3 and 200 days. Because of the small value of τ, millions of stars need to be monitored when searching for microlensing in areas such as the GB, the Large Magellanic Cloud, or the Small Magellanic Cloud. The value of τ is much higher for cosmologically distant sources. Assuming that the ordinary stellar populations of galaxies are the dominant causes of microlensing events, Wyithe & Turner (2002) concluded that in a flat universe, at least 1% of high-redshift sources ($z_s \geqslant 1$) are microlensed by stars at any given time. Zakharov, Popović, & Jovanović

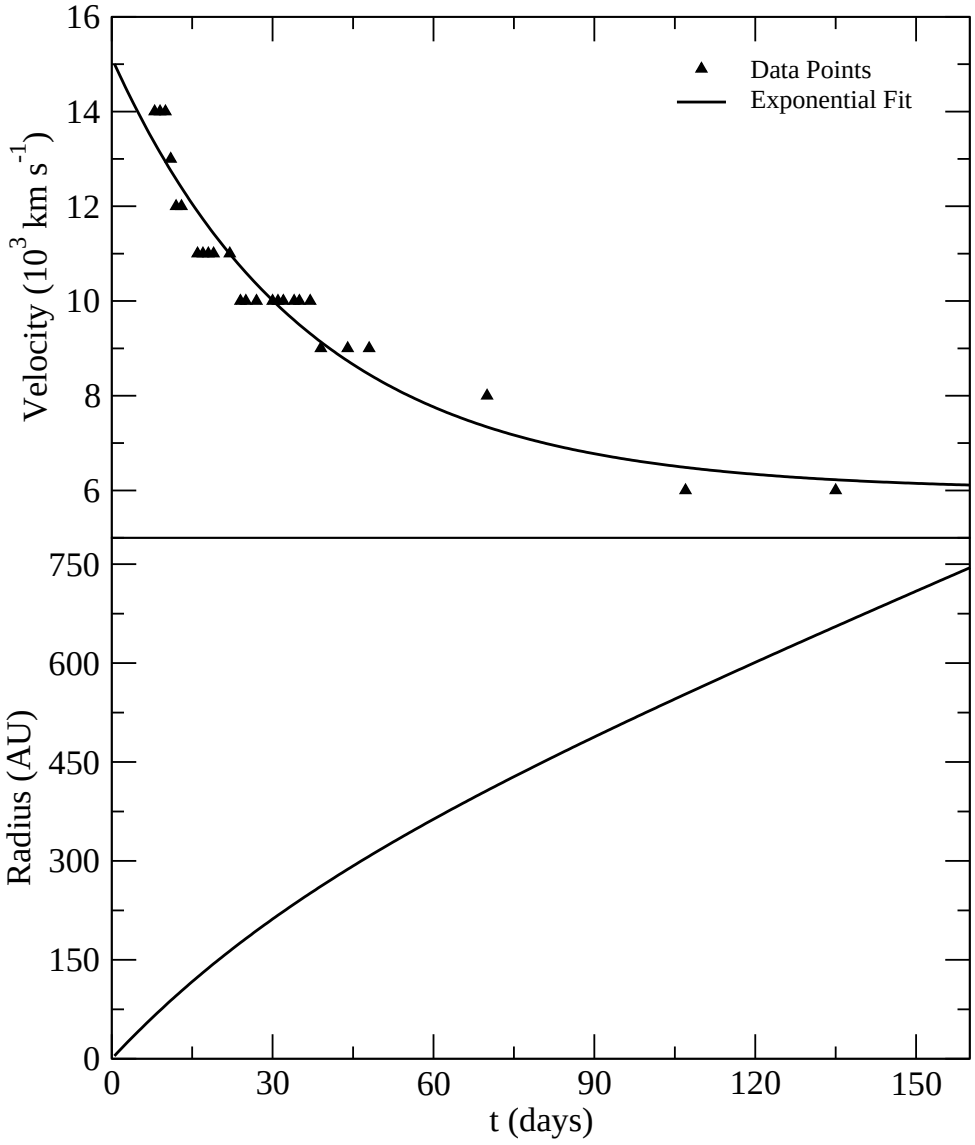


Figure 2.4: Expansion speed (*upper panel*) and the radius (*lower panel*) of the photosphere of a type Ia supernova as a function of time in the source frame.

(2004) estimated that the optical depth for microlensing caused by deflectors both localized in galaxies and distributed uniformly, might reach 10% for sources at $z_s \sim 2$. If we look at bulge-bulge lensing , Han & Gould (2003) give a model for the bulge from which a value of $\tau = 0.98 \times 10^{-6}$ is computed. They additionally compute an effective column density for deflectors $\Sigma_* = 2086\ \mathrm{M}_\odot \mathrm{pc}^{-2}$ and a characteristic source-lens separation $\overline{D} = 782\,\mathrm{pc}$ defined by

$$\tau = \frac{4\pi G}{c^2}\Sigma_* \overline{D}. \tag{2.17}$$

If we simply look at the bulge of a similar galaxy at $z = 0.05$ we expect a similar Σ_* but $\overline{D}$ becomes the distance to the deflector D_d and hence increased by a factor $\approx 2.7 \times 10^5$. This would bring the optical depth up to 27% when looking through such a galaxy. At this distance the size of the bulge is ~ 1 arcsec and clearly resolvable. The downside is one of alignment. What is the chance of a host galaxy being appropriately aligned with a foreground galaxy? The best place to see this effect seems to be the foregrounds of dense clusters. Because the typical galaxy is expected to contain a SN Ia every 10^3 years, some $3700(1+z)$ alignments would have to be followed for a year to see one event.

As mentioned above, the amplification of a point source falling inside the Einstein ring r_E is larger than 1.34. The probability of a larger amplification is proportionally smaller. The probability of having an amplification larger than A for a given lensing configuration is

$$p(A) = u_A^2\, \tau(z_s)\,, \tag{2.18}$$

where $u_A \equiv b_A/r_E$ is the normalized impact parameter, resulting in amplification A (Paczyński, 1986a,b) and $\tau(z_s)$ is the optical depth for a source at redshift z_s. For a point source, the result is

$$u_A = \sqrt{2\left(\frac{A}{\sqrt{A^2-1}} - 1\right)}\,. \tag{2.19}$$

In the next section we use (2.18) to reduce the optical depth to probabilities appropriate for higher amplifications, also see Appendix A.

2.4 Microlensed Light Curves

2.4.1 Results

In this section we use the model light curve of § 2.2 and the microlensing theory of § 2.3 to predict the shape of lensed light curves of type Ia supernovae for both moving and stationary lenses. We have calculated absolute magnitudes of the lensed SNe type Ia in the V-band. We assume that the source is at redshift $z_s = 1.0$, hence introducing a time dilation factor of $(z+1)^{-1} = 0.5$, and is lensed by a deflector located at redshift $z_d = 0.05$. Figure 2.5 shows the geometry of our model. To calculate the amplification as a function of time (eq. [2.10]), we need to know the distance l between the supernova and the deflector, projected on the plane of the deflector,

$$l(t) = \sqrt{l_o^2 + vt\left(vt \mp 2\sqrt{l_o^2 - b^2}\right)}\,, \tag{2.20}$$

where the minus sign is used when the supernova source explodes ($t = 0$ and $l = l_o$) before getting to the point of closest approach, b, and the plus sign when it explodes after. We also need the Einstein ring radius r_E which is determined by the mass of the deflector m_d and the distances of the supernova and the deflector from the observer.

We plot light curves for various values of the parameters m_d, b, l_o, and v (the relative speed of source and deflector projected on the deflector's plane). Our sample deflector masses are 10^{-3} $M_\odot$, 1 $M_\odot$, and 10 $M_\odot$. In the moving-lens scenario we take the source to move in the deflector plane for 1,000 days (observer time) with three relative projected speeds of the source v, 0.1 AU day^{-1}, 0.5 AU day^{-1}, and 1.0 AU day^{-1}.

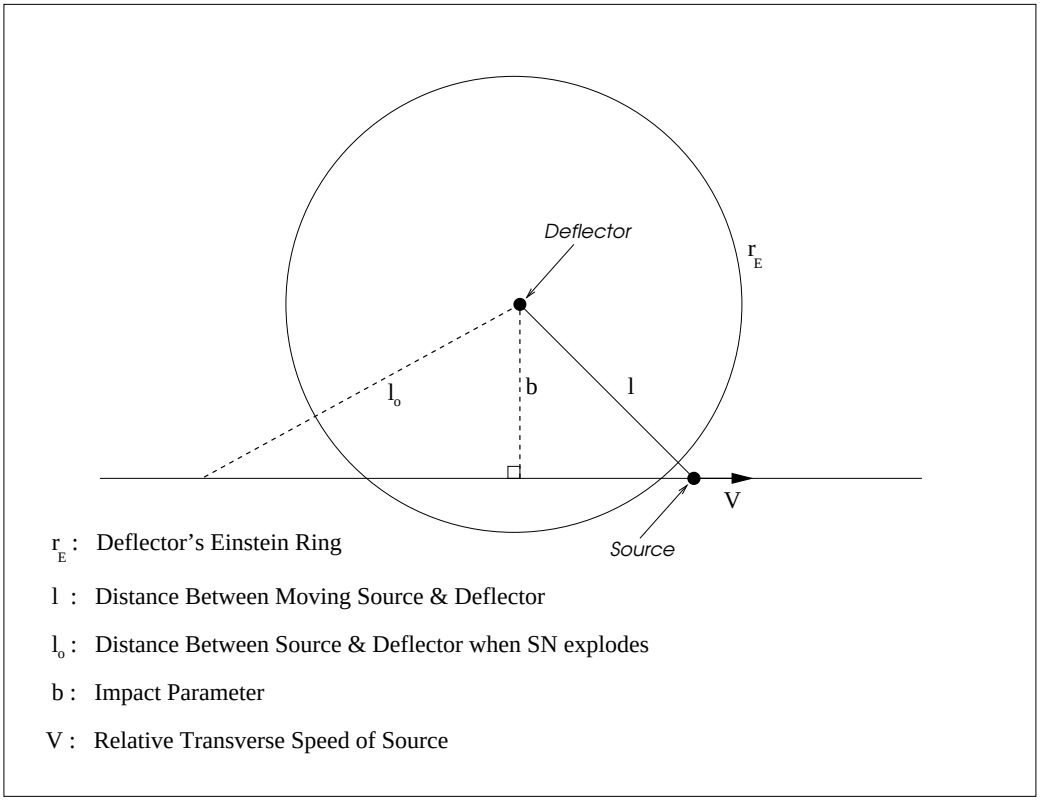


Figure 2.5: Geometry of the microlensing model used in § 4.

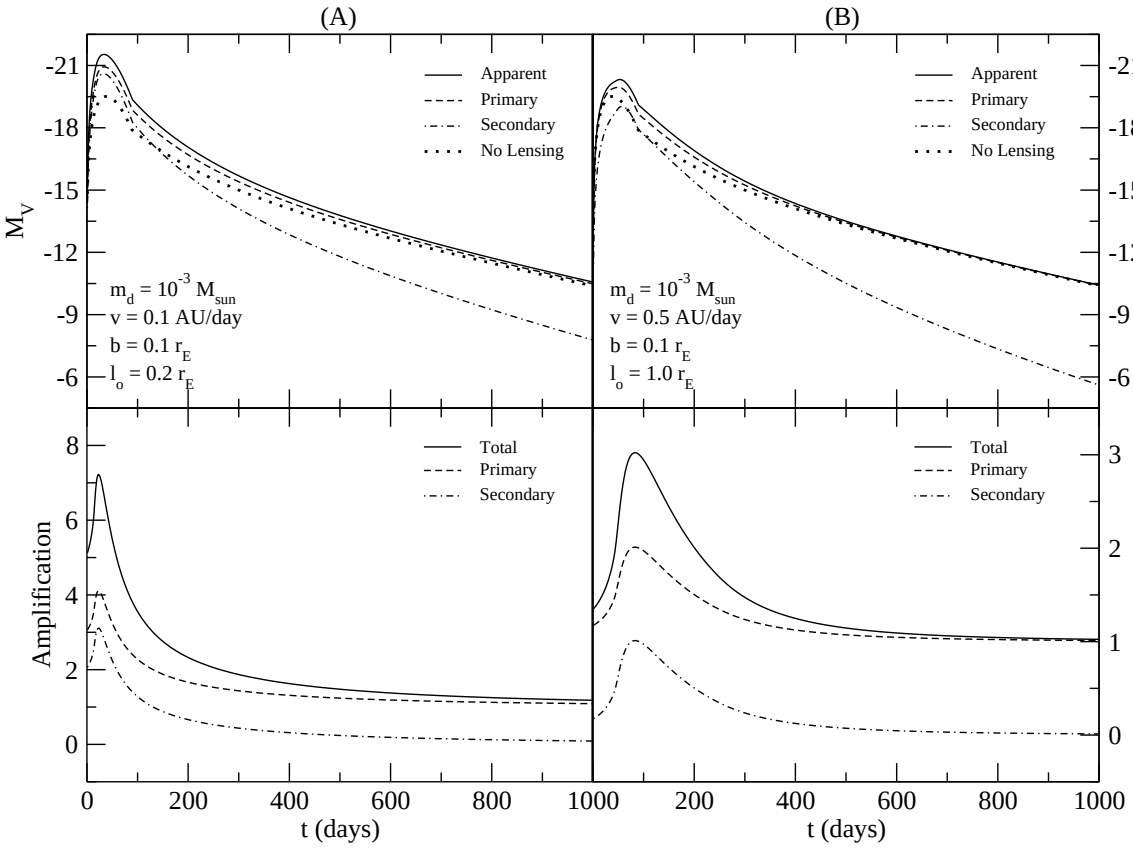


Figure 2.6: Alification curves (*lower panels*) and light curve (*upper panels*) of a supernova at $z_s = 1.0$, microlensed by a deflector at $z_d = 0.05$ with a mass of $m_d = 10^{-3}$ $M_\odot$ for two different lensing configurations (A and B).

Moving Lens

Figures 2.6 through 2.8 show the amplification curves (lower panels) and the light curves (upper panels) of lensed supernova for six different sets of input parameters with moving lens. Each figure contains two diagrams (A and B) for each given mass. These interesting cases have been selected from a large number of configurations. The bottom panel of each figure shows the amplification of the primary and secondary images as well as their sum (total amplification), and the top panel includes light curves of the two images and their sum (the apparent light curve) as well as the original (unlensed) light curve of the supernova.

We are plotting amplified absolute magnitudes of the supernova in the V-band,

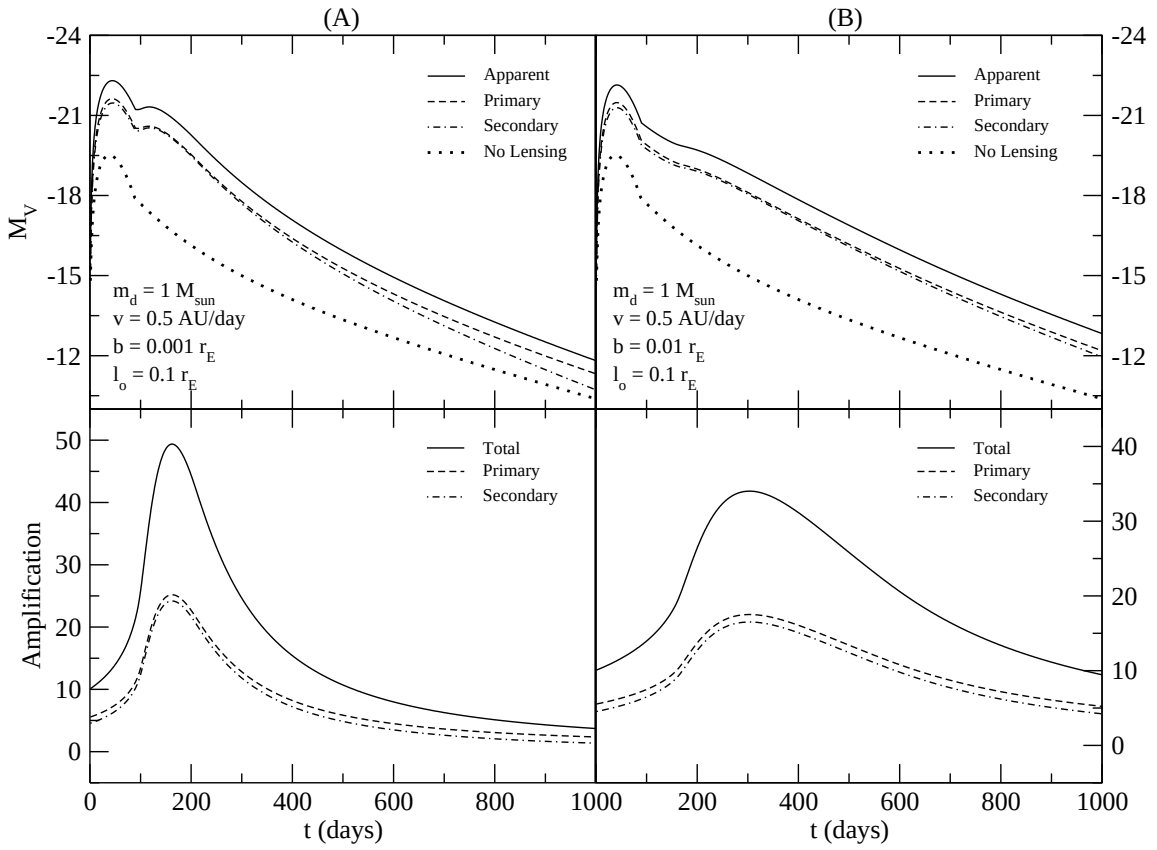


Figure 2.7: Same as Fig. 2.6, with $m_d = 1$ $M_\odot$.

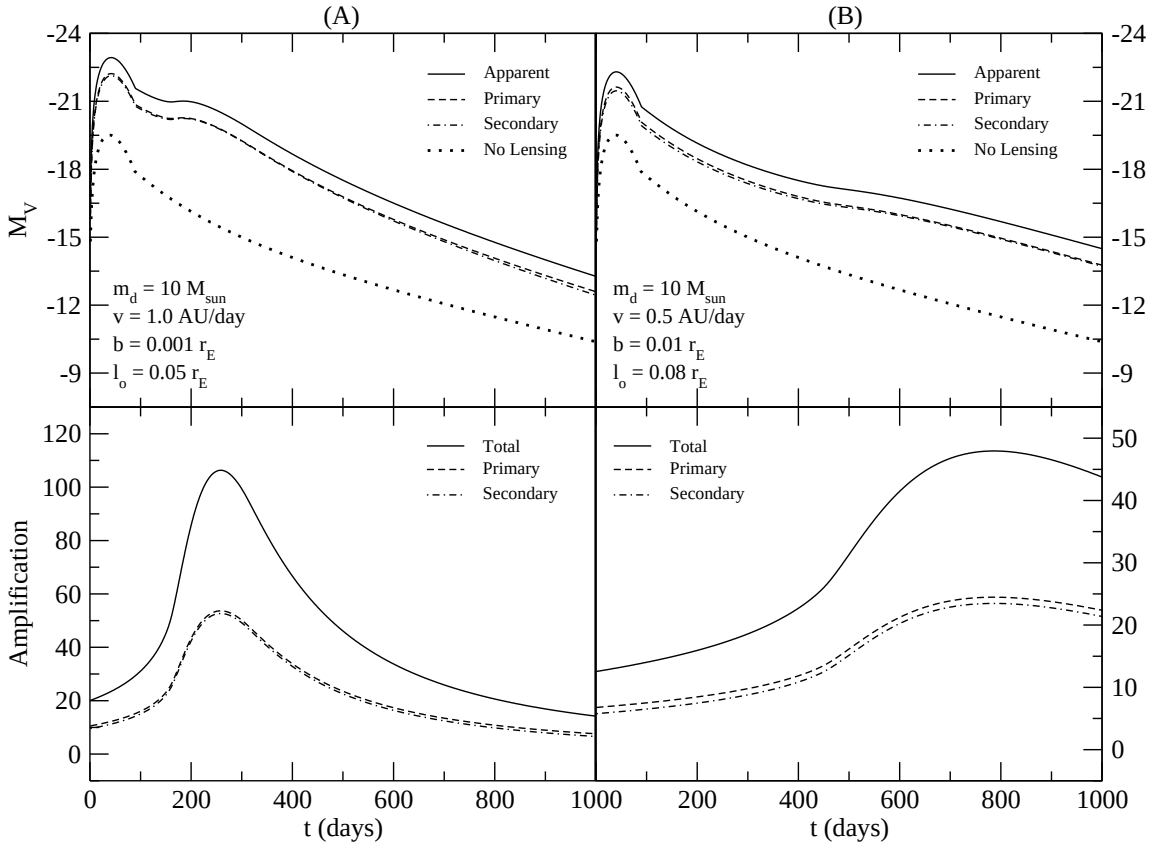


Figure 2.8: Same as Fig. 2.6, with $m_d = 10\ \mathrm{M}_\odot$.

however, due to the redshift of the source, these light curves would be observed in the I-band. With the source located at $z_s = 1$, $M_V > -15.5$ is too dim to be seen. Nonetheless, we include the complete amplification and light curves to show their trends over a period of 1,000 days after the supernova explosion. It should be noticed that amplification curves are not symmetric (like that of a point source) since we are taking into account the expansion of the source as well as intensity profile across it.

For many cases, microlensing has a less dramatic effect on the light curve's shape; it simply provides an overall increase in its magnitude, and would be difficult to distinguish from amplification due to the galaxy hosting the microlens. However in more interesting cases, we can easily match the features in the light curve in each figure to the corresponding peak of the amplification curve. Figures 2.6A and 2.6B show an overal amplification around the peak as well as a slight twist in the peak itself as a result of a narrow-width rise in the amplification of supernova light at the same time.

Figure 2.7A shows a huge overall increase in the brightness of the whole light curve together with a double peak occuring about 100 days after the original (first) one. The presence of this second peak (which can easily be distinguished from the original one) is the result of an enormous amplification around the time the lens moves in the vicinity of impact paramater. It should be mentioned that at lower speeds, the amplification curve would flatten out and this feature would disappear.

A double peak can also be seen in figure 2.8A, where a moving 10 $M_\odot$ deflector reaches the impact parameter at a high speed of 1 AU day^{-1} well within the Einstein ring ($b = 0.001 r_E$). This second peak is bright enough to be seen 200 days after the original peak. In this case if the impact parameter is reduced to $b = 0$ the second peak would actually be larger than the first. Here, the magnitude of the 'narrowed' peak would reach $M_V \sim -23$ which is comparable to the magnitude of a weak quasar. Such huge amplifications can cause a bias in observing supernovae, allowing one to observe more distant objects (Oguri, Suto, & Turner, 2003), and as a result, to increase the

depth (volume) of any supernova survey. Notice that this light curve looks different from those of strongly lensed supernovae in which, the lensed curve merely has an overall magnitude shift upward due to the static magnification introduced by the microlens' parent galaxy.

In Figures 2.7B and 2.7B, the lensed light curve hits a plateau before falling back on the expected trend of a type Ia supernova. The plateau in figure 2.8B can be observed almost two years after the peak of the light curve, assuming the survey followup on this supernova would last that long.

Stationary Lens

The interesting cases described above occurred because the supernova exploded within the Einstein ring of a deflector, while the deflector proceeded to move on a time scale comparable to the life of the supernova. Schneider & Wagoner (1987) found, in some instances, some modifications to the light curve caused by the supernova's photosphere expanding into a deflector's critical point, in the absence of relative motion of lens and source.

It is, however, easy to see how ignoring the relative motion can result in understimating the effect of lensing on the SNe light curves. To show the understimate, we calculated the light curve of an expanding type Ia supernova lensed by stationary deflectors with masses 10^{-3} $M_\odot$ (Fig. 2.9), 1 $M_\odot$ (Fig. 2.10), and 10 $M_\odot$ (Fig. 2.11). These figures show the results of both moving and stationary scenarios for a few lensing configurations (left panels) in the V band with a deflector at redshift z_d=0.05. Magnitude differences (right panels) are given for z_d=0.05, 0.10, 0.15, 0.20, and 0.25. In all cases the source is at redshift z_s=1.0. In the stationary cases the (projected) location of the source on deflector plane remains at $l = l_o$.

As can be seen, the stationary light curves do not show features such as bumps or plateaus observed in the corresponding moving cases. This is due to the fact that the amplification curves for stationary lenses are rather flat and show little change in

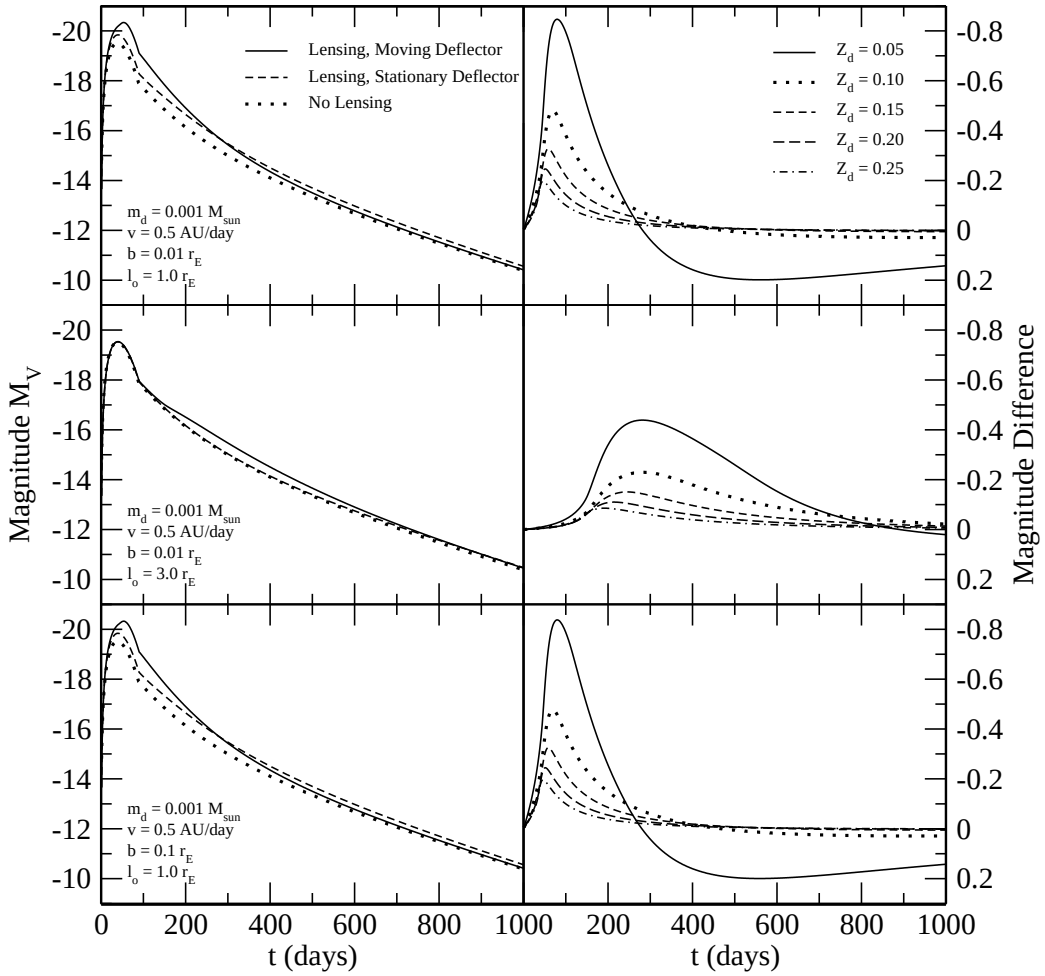


Figure 2.9: This figure shows the light curves of a SN Ia (*left panels*) lensed by a moving deflector and a stationary deflector at redshift $z_d = 0.05$. The right panels show the magnitude difference of the two cases for a deflector with the same mass ($m_d = 10^{-3} M_\odot$) but at different redshifts.

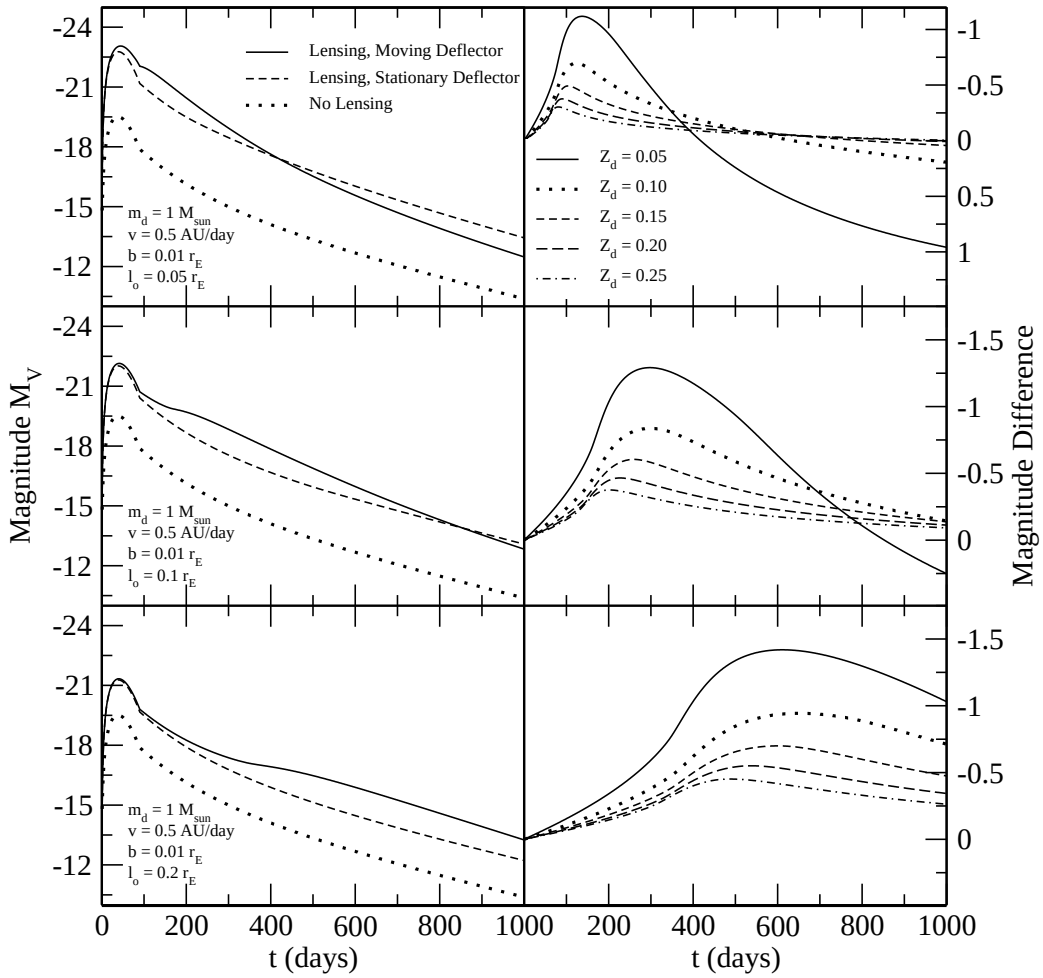


Figure 2.10: Same as Fig. 2.9, with mass $m_d = 1M_\odot$.

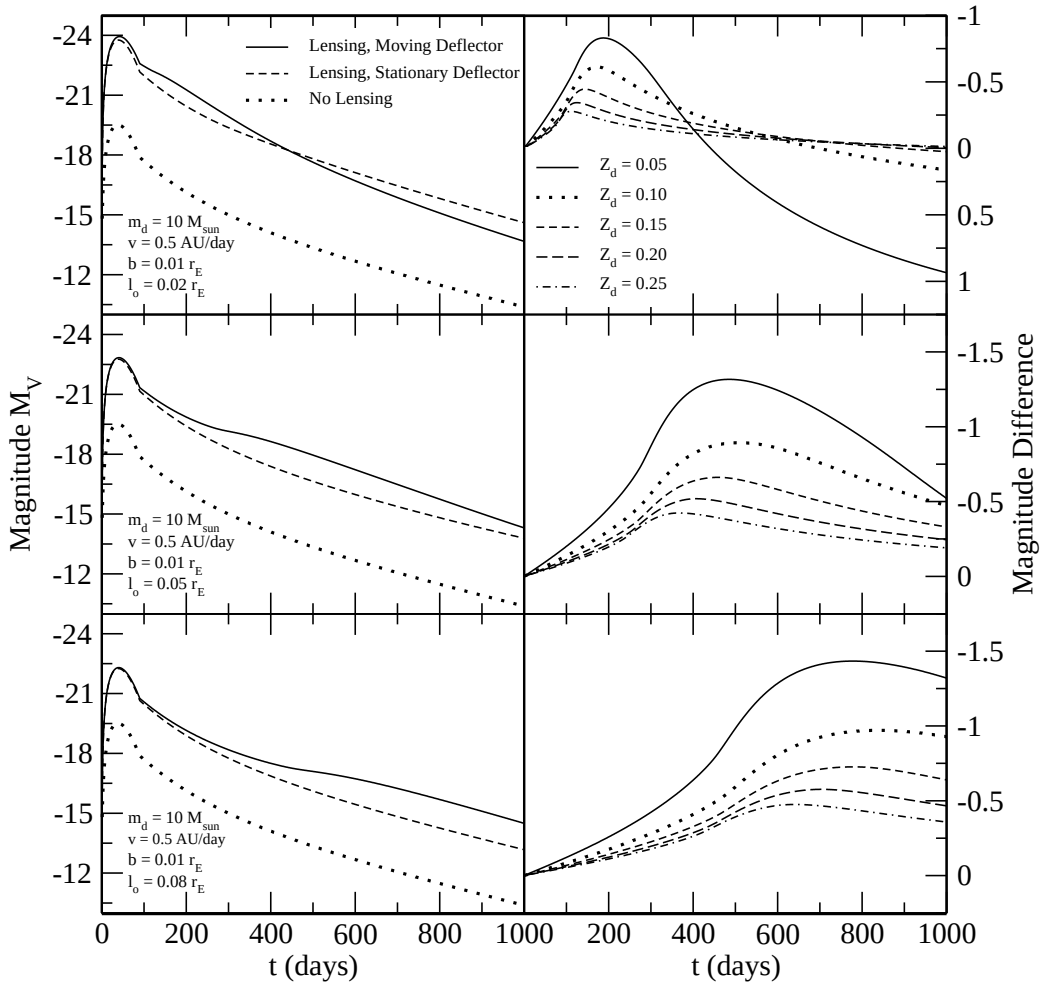


Figure 2.11: Same as Fig. 2.9, with mass $m_d = 10M_\odot$.

amplification as the photosphere expands beyond the deflector. The effect of amplification by stationary deflectors appears as an overall upward shift in the supernova's light curve. A look at the right panels in Figures 2.9 through 2.11 shows that within the current accuracy of $\delta m = 0.1$ in the observation of absolute magnitudes (Astier et al., 2006), the magnitude difference of the moving and stationary scenarios is measurable for the deflector being at least as far as z_d=0.25.

Also, it should be noticed that a supernova lensed by a stationary deflector is brighter than one lensed by a moving deflector beyond the time when the projected distance of source and deflector is greater than l_o; see, for instance, upper right panels of Figures 2.9, 2.10, and 2.11.

2.4.2 Observation Probability

The standard optical depth τ significantly overestimates the probability that the above interesting cases will occur. Using § 2.3 we can correct for the overestimate. For these lensing configurations, the normalized impact parameter u_A does not exceed 0.1 ($A \approx 9$) which, using equation (2.18), gives a maximum probability of $\sim 10^{-4}$ for $z_s \geqslant 1$ ($\tau = 0.01$), and $\sim 10^{-3}$ for $z_s = 2$ ($\tau = 0.1$) if Zakharov, Popović, & Jovanović (2004) are correct.

The numbers above are somewhat higher than Linder, Schneider, & Wagoner (1988) were predicting for Type I SN but not for Type II. With a supernova rate of $R_{SNeIa} = 2,000$ yr^{-1} the SN lensing rate at redshift $z = 1$ is $\sim 10^{-4}\Omega$ yr^{-1} (Oguri, Suto, & Turner, 2003). Rates likes this, together with time scales of some cases studied here, imply that such effects may not be observed unless a large number of cosmologically distant (around 10^4 for $z_s \geqslant 1$) type Ia supernovae are followed for a period of up to 2 years. For the high amplification cases with a second peak, a seperate probability estimate can be made (see Appendix A).

2.5 Conclusion

In this chapter we have shown that microlensing can significantly affect light curves of some cosmologically distant type Ia supernovae. We restricted our calculation to $z_s = 1$ and $z_d = 0.05$ in the currently accepted $\Omega_m = 0.3$, $\Omega_\Lambda = 0.7$ flat cosmological model. We found that microlensing can not only increase the magnitude of the light curve but also can cause a change in its shape. Relative transverse motion of the SN and lens, added to the expanding photosphere (as studied by Schneider & Wagoner (1987)) can result in features such as a narrow but high peak, a plateau following the peak, or even the presence of a second peak.

In § 2.4 we concluded that for microlensing by compact masses distributed through the cosmos, the optical depth is 0.01 ($z_s \sim 1$) but might reach 0.1 ($z_s \sim 2$), meaning that the overall chance of a distant supernova type Ia being microlensed is not negligible. Any multi-band supernova survey aimed at finding supernovae at redshifts around $z = 1$ (and above), could discover and identify *one* microlensed SN Ia event out of roughly *a hundred* events. However, the low impact parameters required to produce the special features depicted in § 2.4 demand observation of $\sim 10^4$ supernovae at $z_s \geqslant 1$. And, to see unusual features such as double peaks, the lensed supernova must be followed for an extended period of ~ 2 years. In the Appendix A we have made an optical depth type estimate to include double peak events. For microlensing by stars in the bulge of a galaxy at $z_d = 0.05$ we find a max probability of $\sim 1.7 \times 10^{-3}$. This is an ideal deflector distance for observing double peaks due to transverse motion. As expected this number is only slightly smaller than the 27% optical depth estimate made in § 2.3.3 for bulge lensing when corrected for an impact parameter of $u = 0.1$. These estimates do not take into account the observational bias in favor of amplified events (see, for instance, Gunnarsson & Goobar (2003)) nor the possibly enhanced probability due to evolution of the rate at which Type-Ia supernovae have occurred. It is interesting to note that according to OGLE III (Udalski, 2003) a histogram of u values for Bulge lensing peaks at $u \sim 0.1$ (probably due to amplification biasing).

Notice that we have not taken into account macrolensing shear or convergence effects caused by the deflector's host galaxy. The effects of convergence are relatively easy to include, e.g., in our case, the amplifications given in Figure 2.11 would increase by $\sim$30% if the lens galaxy ($z_s = 0.05$) has a surface mass density of $\Sigma = 1000\ \mathrm{M_\odot pc^{-2}}$ at the image. The effects of shear are more complex and demand more complex lens model.

Chapter 3

Effects of Gravitational Microlensing on P-Cygni Profiles of Type Ia Supernovae

3.1 Introduction

It is known that amplification of a light source due to microlensing can affect the spectral line profiles if different parts of the profile originate from different emitting regions of the source (as is believed to be the case with type Ia supernovae) and if the sizes of these regions are comparable to the characteristic lensing radius (Kayser, Refsdal, & Stabell, 1986). Evidence of such effects on line profiles of broad-absorption-line (BAL) quasars was suggested by spectroscopic observations of the multiple images of the strongly lensed quasar H1413+117 (Angonin et al., 1990). Spectral differences observed between the four images of this quasar were investigated by Hutsemékers (1993) using the lens model of Chang-Refsdal (Chang & Refsdal, 1984).

One expects these 'chromatic amplifications' to be observed in a microlensed type Ia supernova as well. SNe Ia are well-studied extended light sources consisting of a central continuum source surrounded by a rapidly expanding atmosphere. The atmosphere accounts for the formation of the observed P-Cygni profiles in the spectral lines of these objects. In § 2 we show how microlensing by a simple (point-mass) Schwarzschild deflector can deform these P-Cygni line profiles. Results of lensing a source at $z_s = 1$ by a deflector at $z_d = 0.05$ are presented in § 3. A flat Friedmann-Lamaître-Robertson-Walker cosmological model with $\Omega_m = 0.3$, $\Omega_\Lambda = 0.7$, and $h_{100} = 0.67$ is assumed to calculate source and deflector distances.

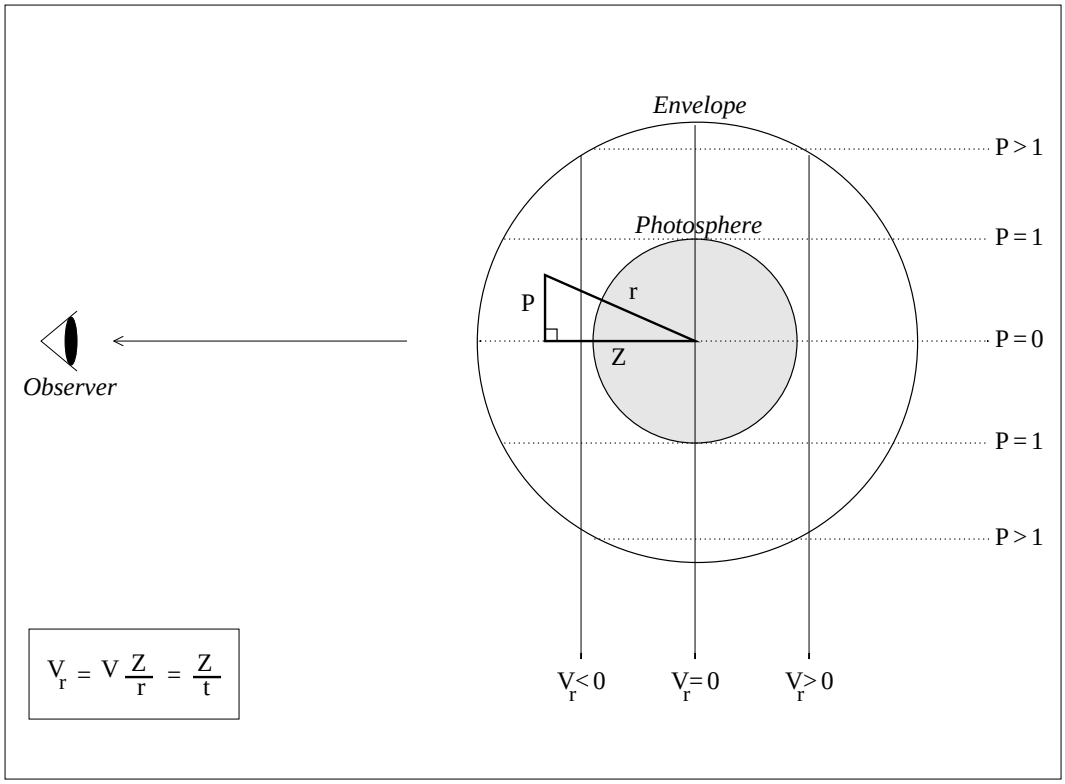


Figure 3.1: Schematic view of a type Ia supernova as seen by an observer. The normalized radius P and planar speed V_r are shown.

3.2 Microlensing of a Supernova as an Extended Source

3.2.1 Line Profiles of Type Ia Supernovae

P-Cygni profiles are characterized by emission lines together with corresponding blueshifted absorption lines. The latter is produced by material moving away from the source with either relativistic velocities (Hutsemékers & Surdej, 1990) or non-relativistic velocities (Beals, 1929). For an explosive expansion the material in each plane perpendicular to the line of sight has a fixed component of velocity V_r toward the observer (Fig. 3.1).

Using the normalized, projected radius P (i.e., the photosphere is at $P = 1$, see

Fig. 3.1), the unlensed flux is defined as

$$F_\lambda = \int_0^{2\pi} \int_0^{P_{max}} I_\lambda(P,\theta)\, P\, dP\, d\theta\,, \tag{3.1}$$

where P_{max} is the normalized, projected radius of the supernova and the plane polar angle θ is measured in the projected source plane.

To compute the intensity I_λ, we used a resonance-scattering synthetic spectrum produced with the fast, parameterized supernova synthetic-spectrum SYNOW. This code is often used for making and studying line identifications and initial coarse analysis of the spectra during the photospheric phase of the supernova (Branch et al., 2003, 2005). The code assumes a spherically symmetric and sharp photosphere that emits a blackbody continuum characterized by temperature T_{bb}.

In SYNOW, the expansion velocity is proportional to radius (homologous expansion: $v = r/t$), as expected for matter coasting at a fixed velocity after an impulsive ejection with a range of velocities. Line formation is treated in the Sobolev approximation (Sobolev, 1958) and occurs by resonance scattering of photons originating from the photosphere. Line blending is treated in a precise way, within the context of the Sobolev approximation. Each line optical depth τ is taken to decrease exponentially with radius (See Jeffery & Branch (1990) and Fisher (2000) for more details). The code does not calculate ionization ratios or rate equations; it takes line identifications to estimate the velocity at the photosphere and the velocity interval within which ions are detected. These quanities give constraints on the composition structure of the ejected matter.

SYNOW calculates the intensity emitted from each zone (concentric annuli) of the projected source. These intensity profiles show the absorption features for various $P < 1$ as well as emission features for $P > 1$. The weighted sum of these intensities over the projected surface of the supernova (eq. [3.1]) gives the synthetic flux profile. Figure 3.2 shows the calculated intensity profiles of sodium. These profiles are obtained for optical depths of $\tau = 1$ (upper panel) and $\tau = 1,000$ (lower panel). The intensities

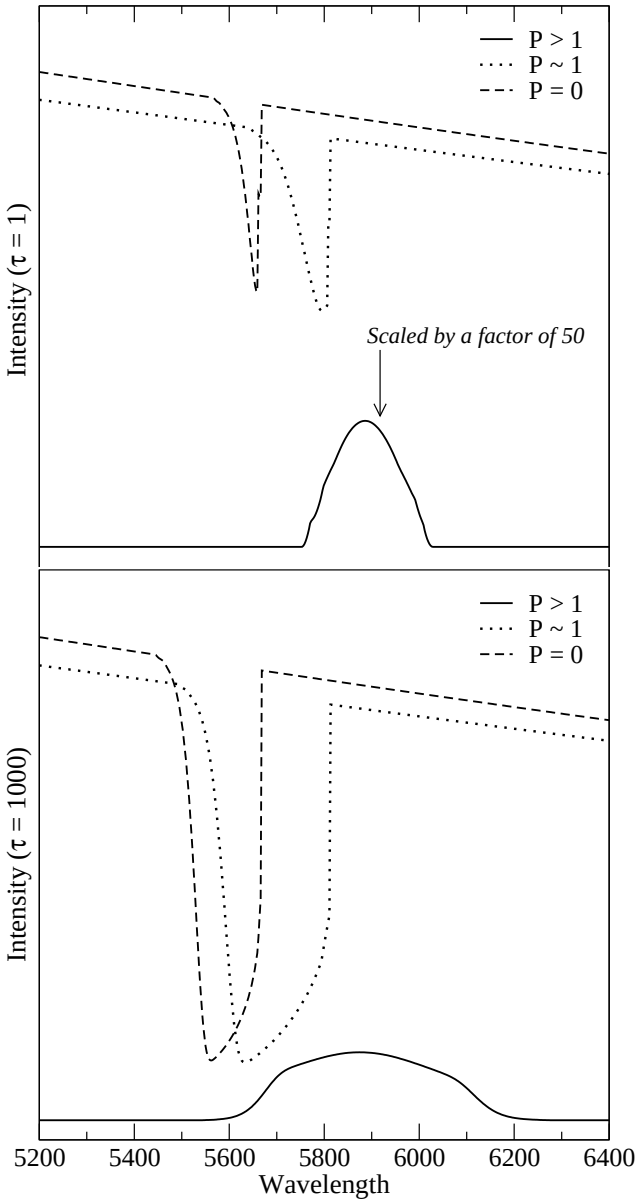


Figure 3.2: Synthetic intensity profile of a type Ia supernova, showing absorption and emission features for $P < 1$, $P > 1$, and P just below 1 for $\tau = 1$ (upper panel) and $\tau = 1,000$ (lower panel). The emission feature in the upper panel is scaled up.

are calculated for $P > 1$, $P = 0$, and P just below 1. The asymmetry seen in the emission features is caused by applying the relativistic Sobolev method (Jeffery, 1993) in the SYNOW code which, in turn, introduces a Doppler boosting in the profiles. Note that to relate the quantities in the comoving and observer frame, one has to use the transformation

$$I_\lambda = I_{\lambda_o} \frac{\lambda_o^5}{\lambda^5}\,, \tag{3.2}$$

where the quantities with subscript 'o' denote those measured in the comoving frame (Mihalas, 1978).

3.2.2 Differential Amplification

Microlensing of an extended source such as a type Ia supernova by an isolated compact mass results in two images, both in line with the source and deflector projected on the sky plane. The 'primary' image, r_p, lies on the same side of the deflector as the source while the 'secondary' image, r_s, is on the opposite side. For solar-mass size deflectors the angular separation of the two images is of the order of micro arcseconds (for redshifts we consider) and as a result, they are seen as a single object (Schneider, Ehlers, & Falco, 1992). The apparent brightness of this 'single' image differs from that of the unlensed source and is proportional to the apparent area of the image, meaning that the brightness of a source is amplified by a factor

$$Amp = \frac{A_o}{A}\,, \tag{3.3}$$

where A_o is the area of the image and A is the area of the source both projected on the sky plane. See last chapter for details.

If the different parts of the spectral profile come from different parts of the source (which is the case for the concentric annuli of an isotropically expanding type Ia supernova), and if the emitting regions are not much bigger than the characteristic lensing radius (Kayser, Refsdal, & Stabell, 1986), one may expect to see not only a

rescaling in the observed flux, but also a deformation in the line profiles. For a lensed supernova, the observed line profile becomes

$$F_\lambda = \int_0^{2\pi} \int_0^{P_{max}} I_\lambda(P,\theta)\, Amp(P,\theta)\, P\, dP\, d\theta\,, \tag{3.4}$$

where $Amp(P,\theta)$ is the amplification of the surface element centered at point (P,θ). Assuming that a supernova explodes isotropically, the altered flux becomes

$$F_\lambda = \int_0^{P_{max}} I_\lambda(P)\, Amp(P)\, P\, dP\,, \tag{3.5}$$

where

$$Amp(P) \equiv \int_0^{2\pi} Amp(P,\theta)\, d\theta\,. \tag{3.6}$$

For an annulus with the width δP bounded by inner and outer radii of $P_- \equiv P - \frac{\delta P}{2}$ and $P_+ \equiv P + \frac{\delta P}{2}$, the amplification becomes

$$Amp(P) = \frac{S_+ - S_-}{\pi\,(P_+^2 - P_-^2)}\,, \tag{3.7}$$

where

$$S_\pm = \int_{-\frac{\pi}{2}}^{\frac{\pi}{2}} P_\pm\,(P_\pm + l\,\sin\varphi)\sqrt{1 + \frac{4r_E^2}{l^2 + P_\pm^2 + 2P_\pm l\,\sin\varphi}}\,d\varphi\,. \tag{3.8}$$

In the above equation, l is the distance between the deflector and supernova, and r_E is the radius of Einstein ring. All distances are projected on the deflector plane.

The amplification can be calculated using elliptical integrals as mentioned in Chapter 2. Figure 3.3 shows amplification as a function of the expansion velocity of the projected annuli for several values of l in terms of the Einstein ring r_E. Notice that each curve peaks at the velocity corresponding to the annulus which intercepts the line of sight from observer to deflector.

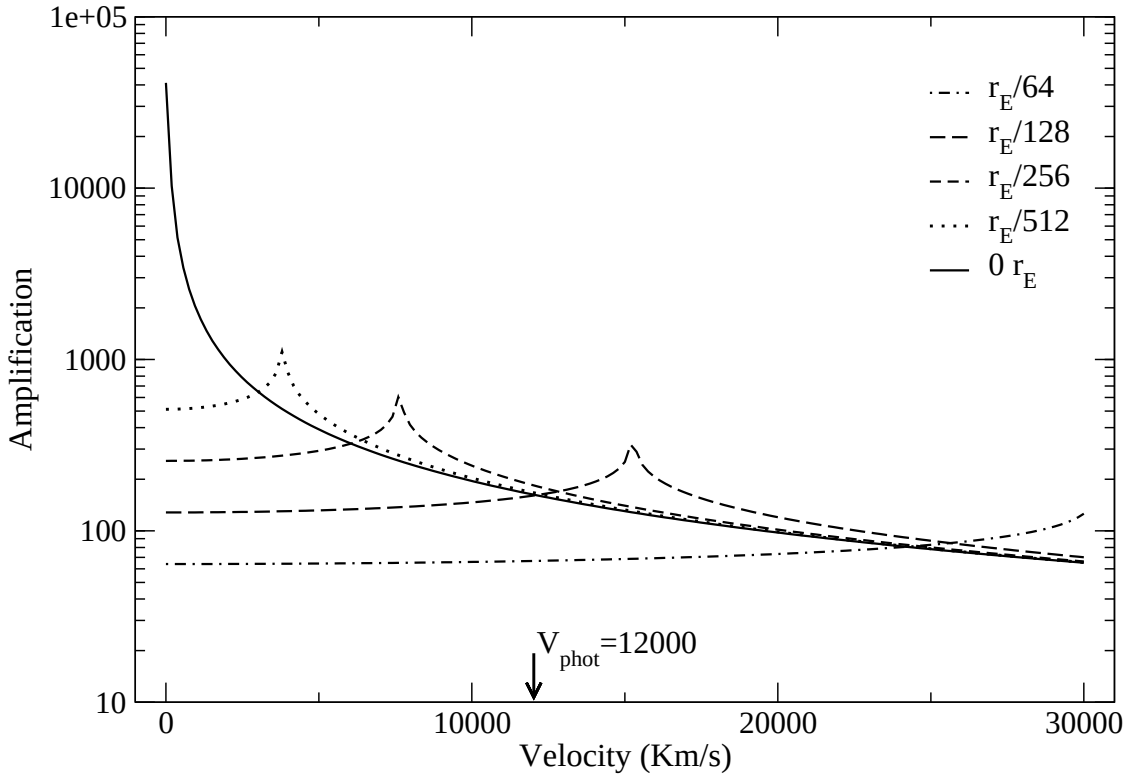


Figure 3.3: Amplification curves of any point on the projected source as a function of expansion velocity for different values of l. The value of photospheric expansion speed determines the zone (absorption or emission) with higher amplification.

3.3 Lensed Profiles

In this section we calculate the deformed spectral profiles of microlensed SNe Ia. To calculate the differential amplification, we need to specify the distance l between the supernova and the deflector projected on the plane of the deflector (sky plane), normalized by the Einstein ring radius r_E,

$$u_A \equiv \frac{l}{r_E}\,. \tag{3.9}$$

The radius r_E is determined by the mass of the deflector m_d and the weighted distance (of luminosity distances) D,

$$r_E = \sqrt{\frac{4Gm_dD}{c^2}}\,, \tag{3.10}$$

where $D \equiv D_{ds}D_d/D_s$ in which, D_s, D_d, and D_{ds} are the respective observer-source, observer-deflector, and deflector-source distances. These are either luminosity distances or angular size distances calculated adopting a concordance (Ω_m, Ω_Λ, h) = (0.3, 0.7, 0.67) cosmology. We assume that the source is at redshift $z_s = 1.0$ and is lensed by a deflector located at redshift $z_d = 0.05$. The point-like deflector has a mass of 1 $M_\odot$ and when positioned at different projected distances it magnifies parts of the extended source differently. The Einstein radius r_E for the above deflector mass and distances is $\sim$ 1301 AU.

We have considered an SN Ia with fixed radius of 178 AU, corresponding to that of a supernova with a maximum atmospheric speed of 30,000 km s^{-1} at eighteen days after the explosion. The radius of the supernova projected on the deflector plane, r_{SN}, is $\sim$ 20 AU, with a photospheric radius of $r_{Ph} \approx 8$ AU. The black body continuum temperature T_{bb} is taken to be 14,000 degrees. Optical depths τ are taken to vary exponentially for each line as

$$\tau(v) = \tau_o\, exp\left(-\frac{v}{v_e}\right)\,, \tag{3.11}$$

where v is the expansion velocity of each layer and v_e is the corresponding e-folding velocity (e.g., 1,000 km s^{-1} for sodium).

We used SYNOW to calculate the unlensed sodium lines as well as their corresponding lensed profile for different optical depths τ_o and normalized distances u_A to show the effect microlensing can have on a single, clean line. Figures 3.4 through 3.7 show the results of such calculations for $\tau_o = 1$ and $1,000$, and $u_A = 0$ and $1/128$ (≈ 0.008)[1]. In these diagrams, flux is plotted in an arbitrary unit as a function of wavelength. As can be seen in Figure 3.4, the emission feature is reduced with respect to the absorption feature because the $P < 1$ region is magnified much more than the $P > 1$ region. The narrowing of the absorption dip as well as an overall shift of the lensed curve to the left is due to the extreme amplification of the $P = 1$ annulus. This is the result of the source-deflector alignment (Fig. 3.3) which causes the area with the highest blueshift ($P = 1$) to get the highest amplification. With $u_A = 1/128$ (Fig. 3.5), the emission feature of the apparent line profile is magnified while the absorption feature does not change remarkably because the amplification curve maximizes outside $P < 1$ region and flattens inside (Fig. 3.3). Figure 3.6 is the same as Figure 3.4 with $\tau = 1,000$. In this figure, we once again notice the effect of extreme amplification of the central zone of the source in the form of a slight shift of the apparent curve toward lower wavelengths. Contrary to Figure 3.4, we do not encounter sharp dips here because each dip in the (unlensed) intensity curve is 7,000 km s^{-1} wide. As expected, moving the deflector away from the line of sight to the source results in a stronger emission component while the absorption dip does not vary remarkably (Fig. 3.7).

Figures 3.8 and 3.9 show the same calculations as those of Figures 3.4 to 3.7 for a SYNOW synthetic spectrum that resembles that of a SN Ia near maximum light with $u_A = 0$ and $1/128$, respectively. We have normalized the lensed profile at $\lambda = 7,000$ Å. Because noticeable deformation of the profiles appear only when the deflector is

[1]We let u_A approach zero as 2^{-n}.

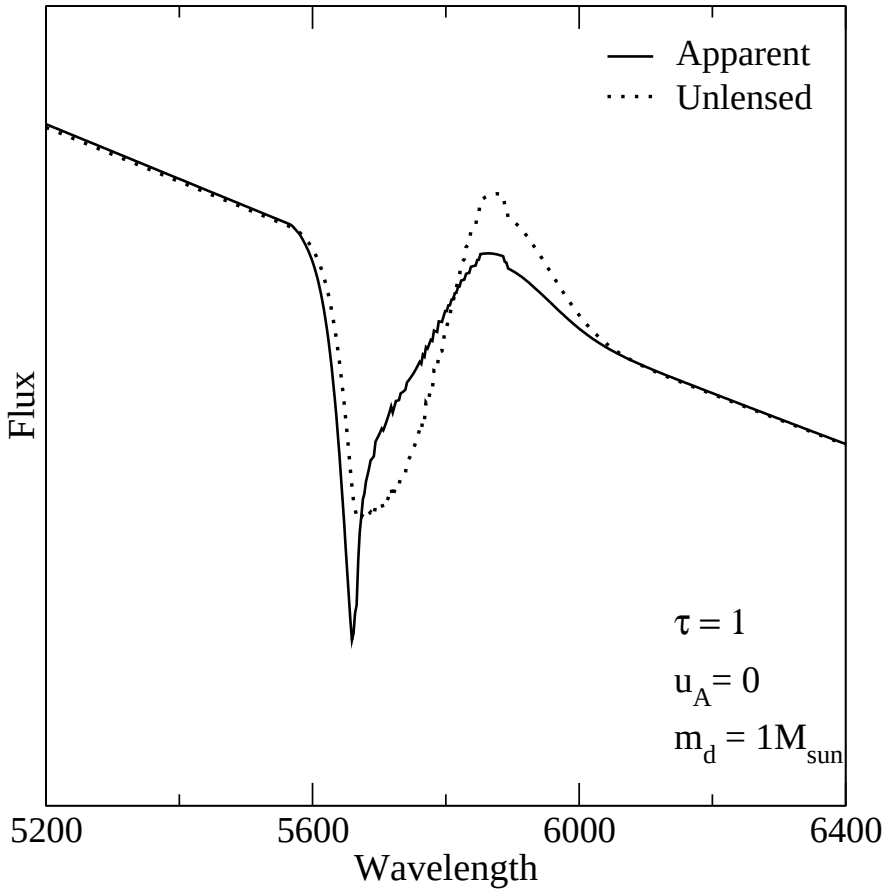


Figure 3.4: Amplified line profile of sodium for $\tau = 1$ and $u_A = 0$. The deflector has a mass of $1M_{\odot}$.

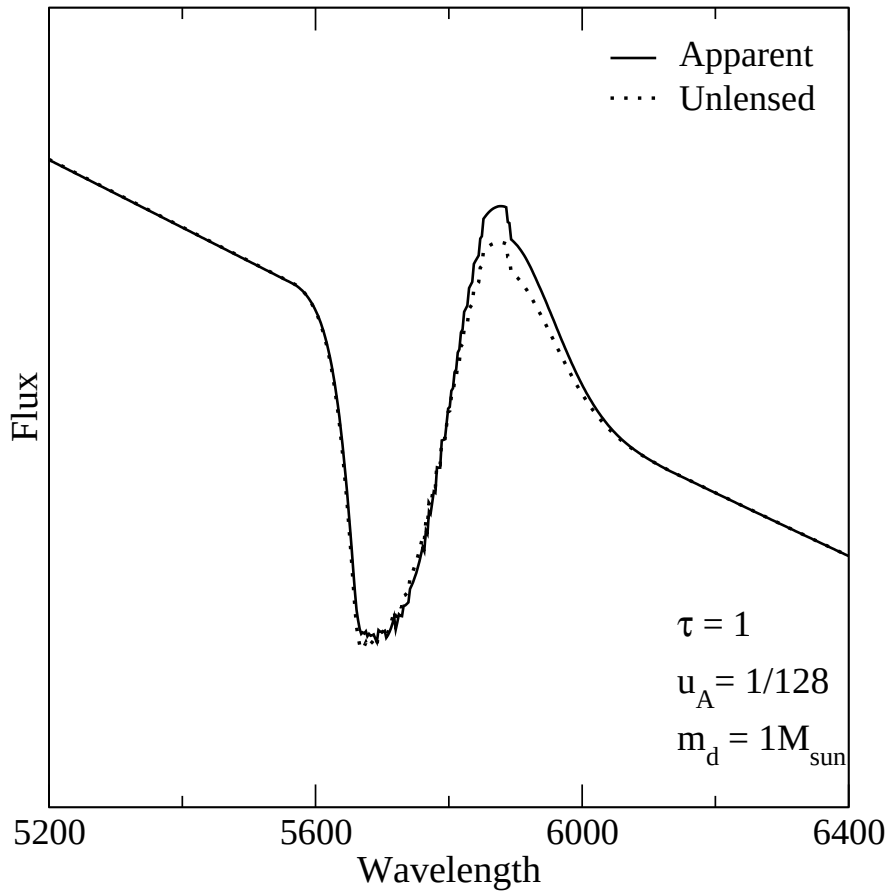


Figure 3.5: Same as Fig. 3.4, with $\tau = 1$ and $u_A = 1/128$.

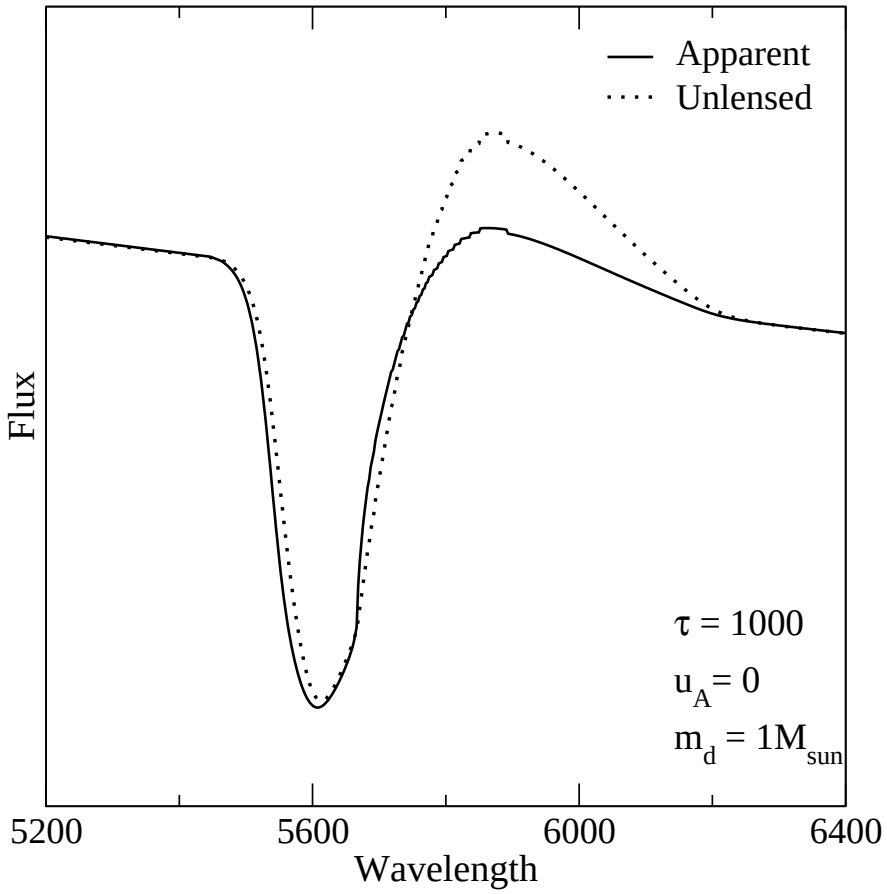


Figure 3.6: Same as Fig. 3.4, with $\tau = 1,000$ and $u_A = 0$.

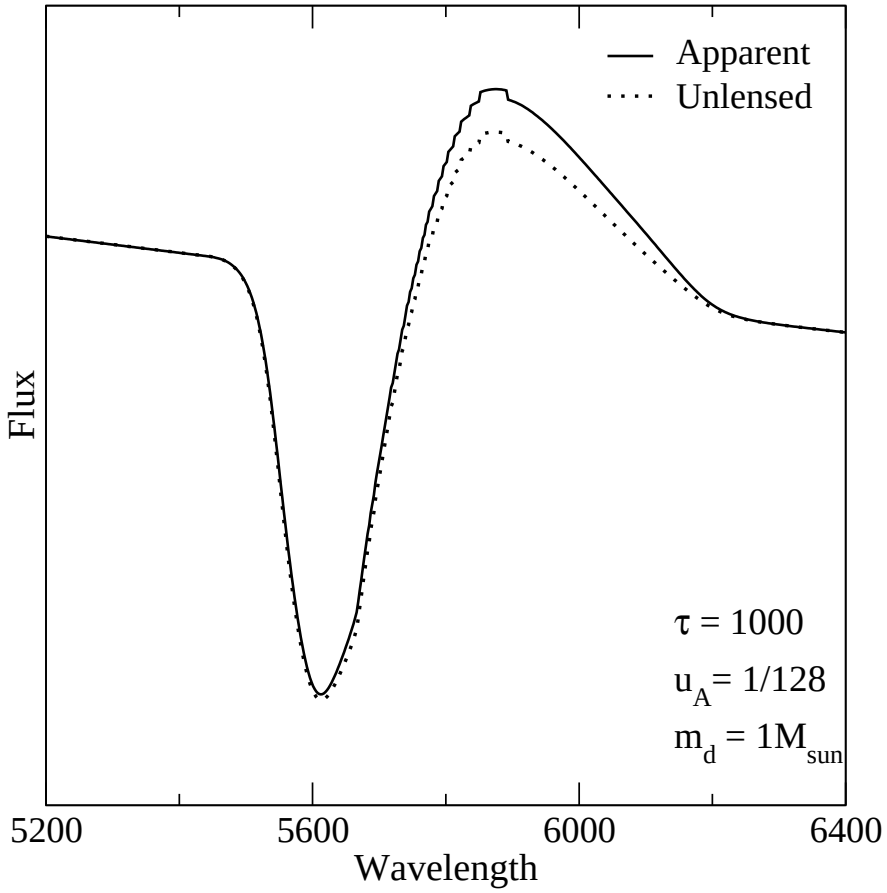


Figure 3.7: Same as Fig. 3.4, with $\tau = 1,000$ and $u_A = 1/128$.

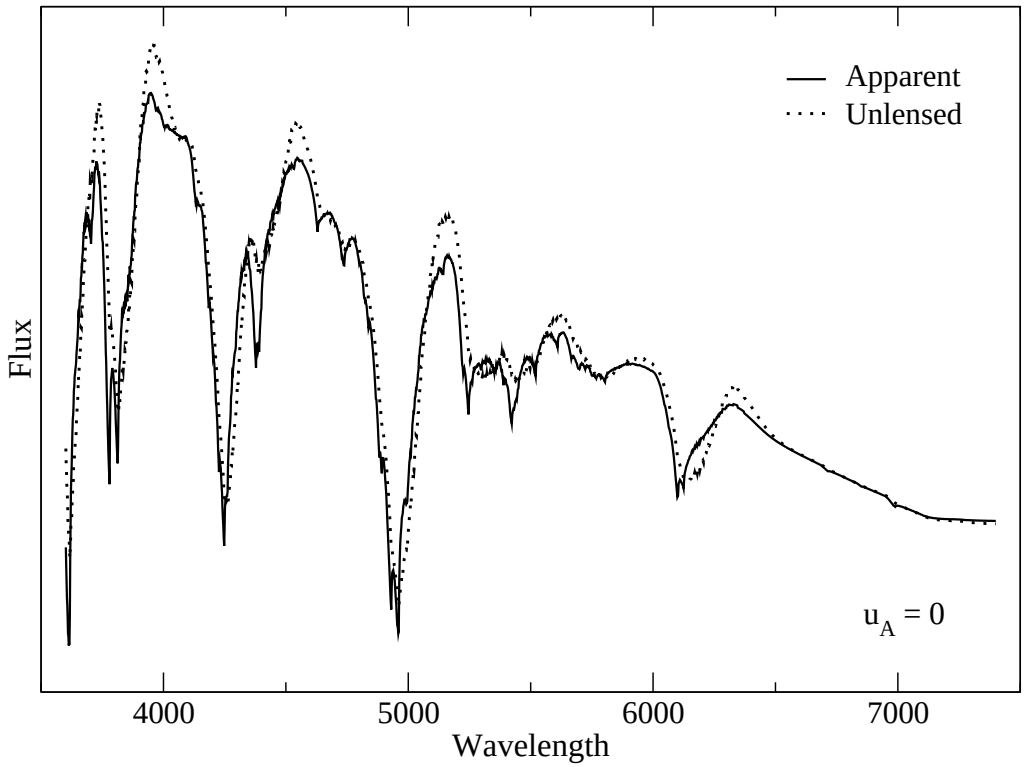


Figure 3.8: Amplified spectral lines of a SYNOW spectrum that resembles the maximum-light spectrum of a SN Ia, with $u_A = 0$ and $m_d = 1M_\odot$.

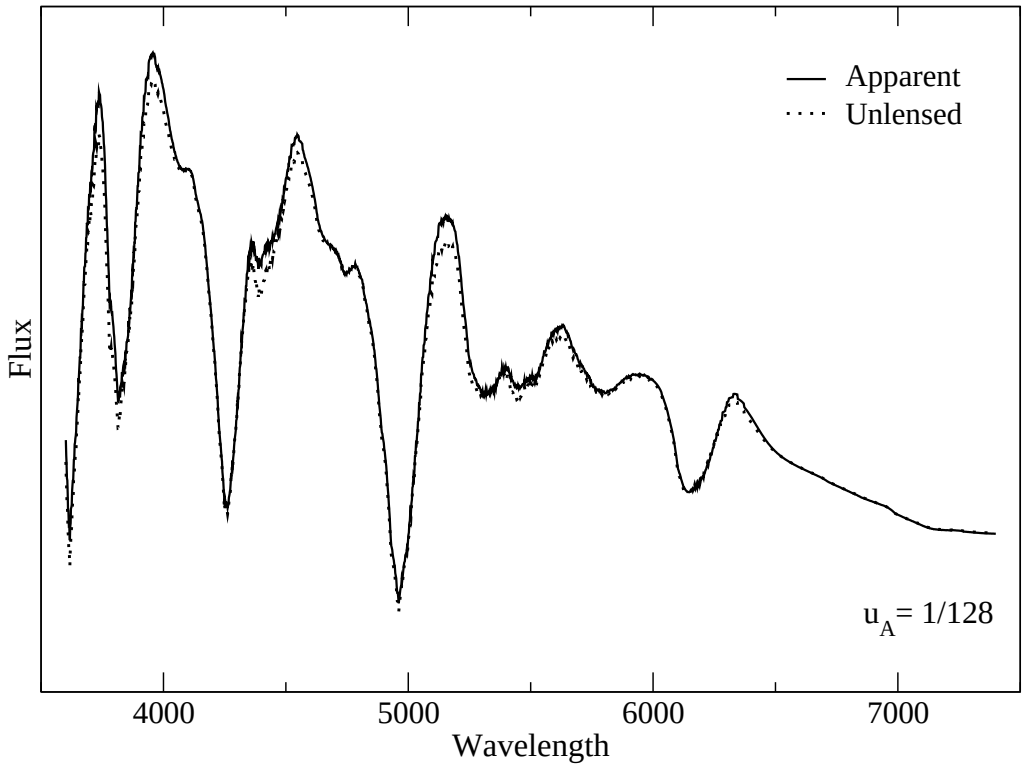


Figure 3.9: Same as Fig. 3.8, with $u_A = 1/128$.

almost aligned with the source (small values of u_A), we did not include results for $u_A > 1/128$ (i.e., $l > 10.17$ AU). With $u_A = 0$ (Fig. 3.8), central parts of supernova are amplified more than the rest which, as explained for Figures 3.4 and 3.6, results in a slight shift toward lower wavelengths. Again, emission features are demagnified with respect to the absorption components. The observed spectral lines show sharp dips because the input value of optical depth τ for each line is not too high. Figure 3.9 is the same as Figure 3.8 but with $u_A = 1/128$. Here, the light coming from the $P > 1$ area carrying emission features has higher amplification compared to the blueshifted light emitted from $P < 1$ and, as expected, the emission component of the P-Cygni features is magnified more than the absorption part.

The change in the profiles can, in general, be summarized as a net increase or decrease of the absorption component relative to the emission one. The apparent change in either component may be so strong that an emission feature could look like a typical P-Cygni profile. To see this effect, the projected source (supernova) must be very close to the deflector on the deflector plane ($l \ll r_E$). Larger impact parameters produce less dramatic deviations from the unlensed profile and could easily be attributed to the intrinsic diversity in spectra of type Ia supernovae rather than gravitational lensing. The deflector redshift used here ($z_d = 0.05$) is not the most likely redshift for microlensing but results in a remarkable amplification gradient necessary for noticeable deformation of P-Cygni profiles. In general, the probability of microlensing cosmologically distant light source is not negligible, and can exceed 1% for a source located at $z_s = 1$ and beyond (Myers et al., 1995; Wyithe & Turner, 2002; Zakharov, Popović, & Jovanović, 2004). However, for the small values of u_A used here the probability of observing such deformations drops below 0.001%.

It should be noted that we have ignored any contribution to lensing from nearby stars and the deflector's parent galaxy. For most microlensing events the amplification due to the host galaxy is expected to introduce a small amplification gradient across the supernova which merely rescales the line profile without introducing any

significant deformation effects. Macrolensing by the galaxy should mainly bias the supernovae detection. The rescaling effect is compensated for by normalizing the lensed profile in order to compare the lensed and unlensed profiles, as done in Figures 3.4 through 3.9. When large amplification gradients are introduced, either by the galaxy or by microlensing stars nearby, a more complicated lens models will be required.

3.4 Conclusion

We have shown that microlensing can significantly affect the P-Cygni profile of a cosmologically distant type Ia supernova. We restricted our calculation to $z_s = 1$ and $z_d = 0.05$ in the commonly used $\Omega_m = 0.3$, $\Omega_\Lambda = 0.7$ flat cosmological model with $h_{100} = 0.67$. We found that microlensing can not only increase the flux magnitude but also can cause a change in its line profiles. Microlensing can cause the features in the spectral lines to be blueshifted with respect to the original spectrum and in general, results in a net increase or decrease of the absorption component relative to the emission component.

We calculated the deformed line profiles for special cases where the deflector is extremely close to the line of sight to the source. Due to the low probability of microlensing events occuring with such small values of u_A, a large population of supernovae (around 10^5) would have to be surveyed to observe a single case of deformation in P-Cygni profiles of type Ia SNe. Also, large deformations demand using more complicated lensing models.

Chapter 4

Gravitational Lensing of Type Ia Supernovae by Pseudo Elliptic NFW Halos

4.1 Introduction

Supernovae have emerged as the most promising standard candles. Due to their significant intrinsic brightness and relative abundance they can be observed in the local and distant universe. Observational efforts to detect high-redshift supernovae have proved their value as cosmological probes. The systematic study and observation of these faint supernovae (mainly type Ia) has been utilized to constrain the cosmic expansion history (Goobar & Perlmutter, 1995; Perlmutter et al., 1999; Schmidt et al., 1998). Light emitted from any celestial object is subject to lensing by intervening objects while traversing the large distances involved (Kantowski, Vaughan, & Branch, 1995) and the farther the light source, the higher its chance of being significantly lensed. Apart from the fact that gravitational lensing can limit the accuracy of luminosity distance measurements (Perlmutter & Schmidt, 2003), it can change the observed rate of supernovae as well.

Studying supernovae and their rates at high redshifts provide us with much needed information for constraining the measurements of the elusive dark energy, as well as understanding the cosmic star formation rate and metal enrichment at high redshifts. In order to observe and, hence, study the faint high-redshift supernovae, one can raise the chance of observation by looking through clusters of galaxies or even massive galaxies (see Smail, et al. (2002) and the references therein). These 'gravitational telescopes' amplify the high-redshift supernovae and thereby increase the chance of

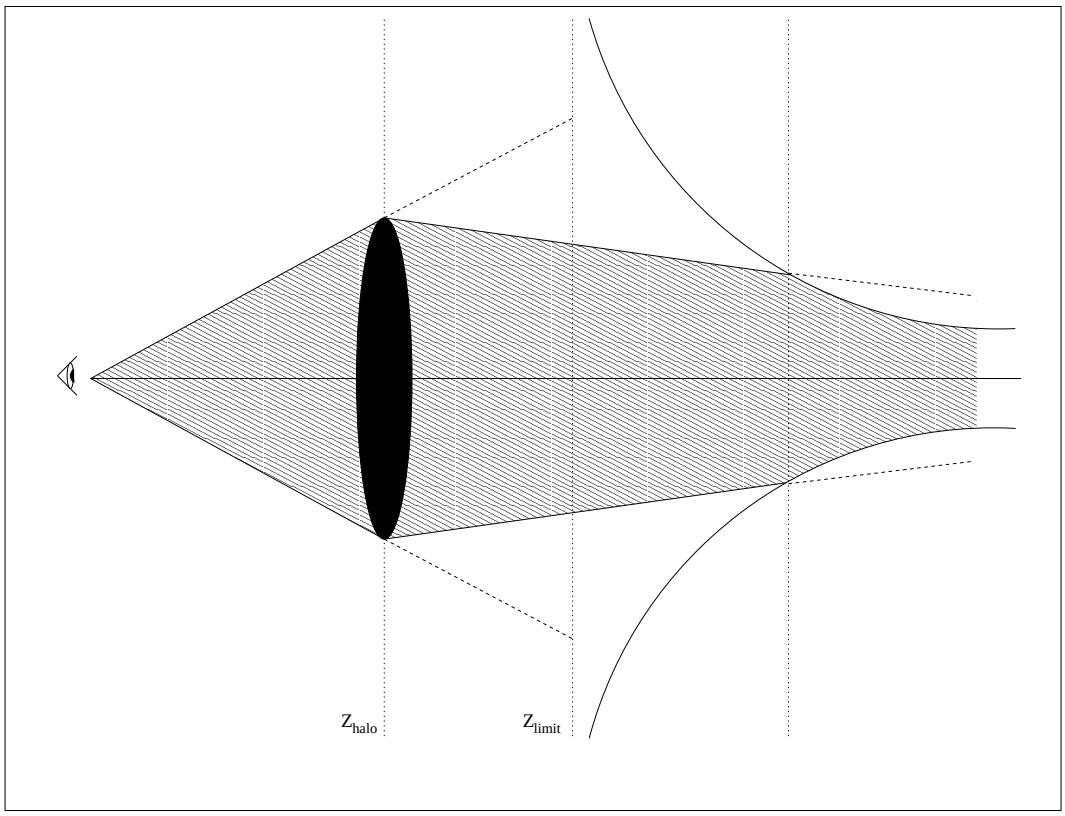


Figure 4.1: Schematic picture of the lensing configuration by a deflecting halo. z_{halo} is the redshift of the halo and z_{limit} is the redshift corresponding to the limiting magnitude m_{limit}. The shaded area shows the volume where SNe are bright enough to be observed.

their detection. However, this boost in observation is offset by the competing effect of depletion (Fig. 4.1), due to the field being spread by the deflector (amplification bias). For an assumed lens model and a given filed of view it is not obvious which effect dominates the observation of supernovae through the halo. The net result depends on the deflector and source parametrs as well as the observational setup (Gunnarsson & Goobar, 2003).

Some research has been conducted on the feasibility of observing supernovae through cluster of galaxies (see, for instance, Saini, Raychaudhary, & Shchekinov, 2002; Gal-Yam, Maoz, & Sharon, 2002; Gunnarsson & Goobar, 2003). These studies have not taken into account how the morphology (mainly the ellipticity) of these

clusters as gravitational telescopes could change the expected supernova rate. In this chapter, we investigate whether introducing ellipticity into the mass distribution of the deflecting halos can affect the observation of supernovae. For this purpose, we use a pseudo elliptical Navarro-Frenk-White (NFW) halo model with different values of ellipticity. Throughout the paper we assume the so-called concordance cosmology where $\Omega_m = 0.3$, $\Omega_\Lambda = 0.7$, and $h_{100} = 0.67$, with $h_{100} = H_0/100$ km s^{-1}Mpc^{-1}. In § 2 we briefly go over the NFW model and show how an analytical formalism for a pseudo elliptical NFW mass profile can be introduced. Strong lensing by thin deflectors as well as the way ellipticity can afffect the amplification is explained in § 4.3. We present and discuss the results of our calculations in § 4.4.

4.2 The NFW Halo Model Profile

4.2.1 NFW Haloes

High resolution N-body numerical simulations (Navarro, Frenk, & White, 1995, 1996, 1997) have indicated the existence of a universal density profile for dark matter halos resulting from the generic dissipationless collapse of density fluctuations. This density profile does not (strongly) depend on the mass of halo, on the power spectrum of initial fluctuations, or on the cosmological parameters. These halo models which are formed through hierarchical clustering diverge with $\rho \propto r^{-1}$ near the halo center and behave as $\rho \propto r^{-3}$ in its outer regions. Inside the virial radius, this so-called NFW halo profile appears to be a very good description of the mass distribution of objects spanning 9 orders of magnitude in mass: ranging from globular clusters to massive galaxy clusters (see Wright & Brainerd (2000) and references therein). The NFW halo model is similar to Hernquist profile (Hernquist, 1990) that gives a good description of elliptical galaxy photometry. However, the two models differ significantly at large radii, possibly due to the fact that elliptical galaxies, countrary to the dark halos, are relatively isolated systems.

The spherically symmetric NFW density profile takes the form of

$$\rho(r) = \frac{\delta_c \rho_c}{\frac{r}{r_s}(1+\frac{r}{r_s})^2} \tag{4.1}$$

where $\rho_c = [3H^2(z)]/(8\pi G)$ is the critical density for closure of the universe at the redshift z of the halo, $H(z)$ is the Hubble parameter at the same redshift, and G is the universal gravity constant. The scale radius $r_s \equiv r_{200}/c$ is the charactristic radius of the halo where c is a dimensionless number refered to as the concentration parameter, and

$$\delta_c = \frac{200}{3}\frac{c^3}{\ln(1+c) - \frac{c}{1+c}} \tag{4.2}$$

is a charactristic overdensity for the halo. The virial radius r_{200} is defined as the radius inside which the mass density of the halo is equal to $200\rho_c$. It is then easy to see that

$$M(r_{200}) \equiv M_{200} = \frac{800}{3}\rho_c r_{200}^3 \,. \tag{4.3}$$

Therefore, NFW halos are defined by two parameters; c, and either r_{200} or M_{200}. For any spherical NFW profile with a given mass, the concentration parameter c can be calculated using the Fortran 77 code charden.f publicly available on the webpage of Julio Navarro[1].

NFW halos can be shown to always produce odd number of images, as opposed to the commonly-used singular isothermal sphere (SIS) model which produces either one or two images (Schneider, Ehlers, & Falco, 1992). Although baryons are expected to isothermalize the matter distribution for halos of galaxy mass and below (Kochanek & White, 2001), taking all of the matter in the universe in isothermal spheres is a great oversimplification (Holz, 2001). It is, hence, reasonable to model halos (at least massive halos) with NFW mass profile instead of SIS model.

[1] http : //pinot.phys.uvic.ca/~jfn/mywebpage/jfn_I.html

4.2.2 Elliptical Potential Model

Here we present the introduced ellipticity ϵ in the circular lensing potential $\varphi(\theta)$, assuming that angular position θ can be scaled by some scale radius/angle θ_s. The reader is encouraged to see Golse & Kneib (2002) and Meneghetti, Bartelmann, & Moscardini (2003) for illuminating discussions. We first introduce the dimensionless radial coordinates $\mathbf{x} = (x_1, x_2) = \mathbf{R}/r_s = \boldsymbol{\theta}/\theta_s$ where $\mathbf{R}$ is the radial coordinate in the deflector plane, and $\theta_s = r_s/D_d$. Then, one can introduce the ellipticity in the expression of the lens potential by substituting x_ϵ for x, using the following elliptical coordinate system:

$$\left\{ \begin{array}{lcl} x_{1\epsilon} & = & \sqrt{a_{1\epsilon}}\, x_1 \\ x_{2\epsilon} & = & \sqrt{a_{2\epsilon}}\, x_2 \\ x_\epsilon & = & \sqrt{x_{1\epsilon}^2 + x_{2\epsilon}^2} \;=\; \sqrt{a_{1\epsilon} x_1^2 + a_{2\epsilon} x_2^2} \\ \phi_\epsilon & = & \arctan\left(x_{2\epsilon}/x_{1\epsilon}\right) \end{array} \right. \tag{4.4}$$

where $a_{1\epsilon}$ and $a_{2\epsilon}$ are the two parameters used to define the ellipticity, as explained below.

From the elliptical lens potential $\varphi_\epsilon(x) \equiv \varphi(x_\epsilon)$, we can calculatete the elliptical deflection angle (see § 3.2):

$$\boldsymbol{\alpha}_\epsilon(\mathbf{x}) = \left(\begin{array}{l} \dfrac{\partial \varphi_\epsilon}{\partial x_1} = \alpha(x_\epsilon)\sqrt{a_{1\epsilon}}\cos\phi_\epsilon \\ \dfrac{\partial \varphi_\epsilon}{\partial x_2} = \alpha(x_\epsilon)\sqrt{a_{2\epsilon}}\sin\phi_\epsilon \end{array} \right) \tag{4.5}$$

Notice that the expressions above hold for any definition of $a_{1\epsilon}$ and $a_{2\epsilon}$. Here, we follow Golse & Kneib (2002) who, in order to be able to analytically derive the convergence and shear, chose the following elliptical parameters:

$$a_{1\epsilon} = 1 - \epsilon \tag{4.6}$$

$$a_{2\epsilon} = 1 + \epsilon \tag{4.7}$$

which for small values of ellipticity ϵ results in the same ellipticity along the x_1 as the standard elliptical model of

$$a_{1\epsilon} = 1 - \epsilon \tag{4.8}$$

$$a_{2\epsilon} = 1/(1 - \epsilon) \tag{4.9}$$

with $\epsilon = 1 - b/a$, where a and b are the semi-major and semi-minor axis of the projected elliptic potential, respectively.

4.3 Gravitational Lensing: a Reminder

4.3.1 General Formalism

In the thin-lens approximation, we define $\mathfrak{z}$ as the optical axis and $\Phi(R, \mathfrak{z})$ as the 3-dimensional Newtonian potential, with $r = \sqrt{R^2 + \mathfrak{z}^2}$. The so-called reduced 2-dimensional potential which is defined in the deflector plane is given by

$$\varphi(\theta) = \frac{2}{\mathfrak{c}^2} \frac{D_{ds}}{D_d D_s} \int_{-\infty}^{+\infty} \Phi(D_d\, \theta, \mathfrak{z})\, d\mathfrak{z} \tag{4.10}$$

(Schneider, Ehlers, & Falco, 1992) where $\mathfrak{c}$ is the speed of light, and $\boldsymbol{\theta} = (\theta_1, \theta_2)$ is the angular position in the image plane. D_d, D_s, and D_{ds} are angular distances of observer-deflector, observer-source, and deflector-source, respectively. The deflection angle α, convergence κ and the shear γ are given by the following set of equations:

$$\begin{cases} \boldsymbol{\alpha}(\theta) = \nabla_\theta \varphi(\theta) \\ \kappa(\theta) = \dfrac{1}{2}\left(\dfrac{\partial^2 \varphi}{\partial \theta_1^2} + \dfrac{\partial^2 \varphi}{\partial \theta_2^2}\right) \\ \gamma^2(\theta) = \|\gamma(\theta)\|^2 = \dfrac{1}{4}\left(\dfrac{\partial^2 \varphi}{\partial \theta_1^2} - \dfrac{\partial^2 \varphi}{\partial \theta_2^2}\right)^2 + \left(\dfrac{\partial^2 \varphi}{\partial \theta_1 \partial \theta_2}\right)^2. \end{cases} \tag{4.11}$$

The lensing equation then reads:

$$\boldsymbol{\beta} = \boldsymbol{\theta} - \boldsymbol{\alpha} = \boldsymbol{\theta} - \nabla_\theta \varphi(\theta) \tag{4.12}$$

where $\beta = (\beta_1, \beta_2)$ is the angular location of the source. The amplification *amp* of a point image formed at θ is:

$$amp(\theta) = \frac{1}{(1-\kappa)^2 - \gamma^2} \tag{4.13}$$

To calculate the angular distances in our work, we use the solution to the Lamé equation for the distance-redshift equation in a partially filled beam Friedmann-Lemaître-Robertson-Walker (FLRW) cosmology. For a filled-beam flat FLRW cosmology, the angular distance D as a function of redshift z is

$$D(z) = \frac{2\mathfrak{c}z}{(1+z)H_0\left(g(z)\right)^{1/2}} \, {}_2F_1\left(\frac{1}{6}, \frac{1}{2}; \frac{7}{6}, -\left[\frac{(\Omega_m^2 \Omega_\Lambda)^{1/3} z^2}{g(z)}\right]^3\right) \tag{4.14}$$

where

$$g(z) \equiv 2\sqrt{1 + \Omega_m z(3 + 3z + z^2)} + 2 + \Omega_m z(3+z)\,. \tag{4.15}$$

See Kantowski (2003) for more detail.

4.3.2 Lensing Parameters of Spherical NFW Model

Several authors have developed the lensing equations for the ordinary, spherical NFW halos (e.g. Bartelmann, 1996; Wright & Brainerd, 2000; Golse & Kneib, 2002). Following § 2.2 we can introduce a dimensionless radial coordinate in the lens plane $\mathbf{x} = (x_1, x_2) = \mathbf{R}/r_s = \theta/\theta_s$ where $\theta_s = r_s/D_d$. The surface mass density then becomes

$$\Sigma(x) = \int_{-\infty}^{+\infty} \rho(r_s\, x, z) dz = 2\delta_c \rho_c r_s F(x) \tag{4.16}$$

with

$$F(x) = \begin{cases} \dfrac{1}{x^2-1}\left(1 - \dfrac{1}{\sqrt{1-x^2}}\operatorname{arcch}\dfrac{1}{x}\right) & (x<1) \\ \dfrac{1}{3} & (x=1) \\ \dfrac{1}{x^2-1}\left(1 - \dfrac{1}{\sqrt{x^2-1}}\arccos\dfrac{1}{x}\right) & (x>1) \end{cases} \tag{4.17}$$

and the mean surface density inside the radius x can be written as

$$\overline{\Sigma}(x) = \frac{1}{\pi x^2}\int_0^x 2\pi x\Sigma(x)dx = 4\delta_c\rho_c r_s\frac{g(x)}{x^2} \tag{4.18}$$

with

$$g(x) = \begin{cases} \ln\dfrac{x}{2} + \dfrac{1}{\sqrt{1-x^2}}\operatorname{arcch}\dfrac{1}{x} & (x<1) \\ 1+\ln\dfrac{1}{2} & (x=1) \\ \ln\dfrac{x}{2} + \dfrac{1}{\sqrt{x^2-1}}\arccos\dfrac{1}{x} & (x>1) \end{cases} \tag{4.19}$$

(see Golse & Kneib (2002)).

The deflection angle α, convergence κ and shear γ turn out as

$$\begin{cases} \alpha(x) &= \theta\dfrac{\overline{\Sigma}(x)}{\Sigma_{\rm crit}} &= 4\kappa_s\dfrac{\theta}{x^2}g(x)\mathbf{e}_x \\ \kappa(x) &= \dfrac{\Sigma(x)}{\Sigma_{\rm crit}} &= 2\kappa_s F(x) \\ \gamma(x) &= \dfrac{\overline{\Sigma}(x)-\Sigma(x)}{\Sigma_{\rm crit}} &= 2\kappa_s\left(\dfrac{2g(x)}{x^2} - F(x)\right) \end{cases} \tag{4.20}$$

where $\kappa_s = \delta_c\rho_c r_s\Sigma_{\rm crit}^{-1}$, with $\Sigma_{\rm crit} \equiv \mathfrak{c}^2 D_s/(4\pi G D_d D_{ds})$.

By integrating the deflection angle, the potential $\varphi(x)$ can be found:

$$\varphi(x) = 2\kappa_s\theta_s^2\, h(x) \tag{4.21}$$

with

$$h(x) = \begin{cases} \ln^2 \frac{x}{2} - \operatorname{arcch}^2 \frac{1}{x} & (x < 1) \\ \ln^2 \frac{x}{2} + \arccos^2 \frac{1}{x} & (x \geq 1) \end{cases} \tag{4.22}$$

4.3.3 Lensing Parameters of Pseudo Elliptical NFW Model

For the particular choice of ϵ in § 2.2, the corresponding convergence and shear can be calculated:

$$\begin{aligned} \kappa_\epsilon(x) &= \frac{1}{2\theta_s^2}\left(\frac{\partial^2\varphi_\epsilon}{\partial x_1^2} + \frac{\partial^2\varphi_\epsilon}{\partial x_2^2}\right) \\ &= \kappa(x_\epsilon) + \frac{\epsilon}{2\theta_s^2}\left(\frac{\partial^2\varphi(x_\epsilon)}{\partial x_{2\epsilon}^2} - \frac{\partial^2\varphi(x_\epsilon)}{\partial x_{1\epsilon}^2}\right) \\ &= \kappa(x_\epsilon) + \epsilon\cos 2\phi_\epsilon\,\gamma(x_\epsilon). \end{aligned} \tag{4.23}$$

and

$$\begin{aligned} \gamma_\epsilon^2(x) &= \frac{1}{4\theta_s^4}\left\{\left(\frac{\partial^2\varphi_\epsilon}{\partial x_1^2} - \frac{\partial^2\varphi_\epsilon}{\partial x_2^2}\right)^2 + \left(2\frac{\partial^2\varphi_\epsilon}{\partial x_1 \partial x_2}\right)^2\right\} \\ &= \gamma^2(x_\epsilon) + 2\epsilon\cos 2\phi_\epsilon\gamma(\vec{x}_\epsilon)\kappa(x_\epsilon) + \epsilon^2(\kappa^2(x_\epsilon) - \cos^2 2\phi_\epsilon\gamma^2(x_\epsilon)). \end{aligned} \tag{4.24}$$

Also, the elliptic projected mass density reads:

$$\Sigma_\epsilon(\mathbf{x}) = \Sigma(\mathbf{x}_\epsilon) + \epsilon\cos 2\phi_\epsilon(\overline{\Sigma}(\mathbf{x}_\epsilon) - \Sigma(\mathbf{x}_\epsilon)). \tag{4.25}$$

The lensing equation now becomes (see Appendix B):

$$\begin{cases} \beta_1 &= \theta_s x_1\left(1 - 4k_s\epsilon_1\dfrac{g(x_\epsilon)}{x_\epsilon^2}\right) \\ \beta_2 &= \theta_s x_2\left(1 - 4k_s\epsilon_2\dfrac{g(x_\epsilon)}{x_\epsilon^2}\right) \end{cases} \tag{4.26}$$

and as one expects, the amplification *amp* reads:

$$amp(\mathbf{x}) = \frac{1}{(1-\kappa_\epsilon(\mathbf{x}))^2 - \gamma_\epsilon^2(\mathbf{x})} \tag{4.27}$$

It can be shown that ellipticities beyond $\epsilon = 0.2$ result in unrealistic 'peanut' shaped projected densities, hence in this work we focus on lower values of ϵ. Figure 4.2 shows the multiple images produced by a $1.0 \times 10^{14} h^{-1} M_\odot$ halo with ellipticity $\epsilon = 0.1$ (courtesy of Golse & Kneib). Dashed lines are the contours with constant surface density Σ_ϵ and the solid lines are the critical and caustic lines. Redshifts of source and deflector are 0.2 and 1.0, respectively.

4.4 The Method

The main reason for studying supernovae magnified by gravitational lensing is to investigate the chance of observing supernovae too faint to be observed in the absence of lensing, which is usually the case for cosmologically distant supernovae, specifically type Ia's. To calculate the observed rate of type Ia supernovae we use the result of predicted rates by Dahlén & Fransson (1999) for a hierarchical star formation rate model with a charactristic time of $\tau = 1$ Gyr (Fig. 4.3), which limits our calculation to the redshift depth of $z_{Max} = 5$.

In order for a supernova to be detected, its apparent magnitude m should not exceed the limiting magnitude of the survey m_{limit}. Using the definitions of the apparent magnitude and amplification, we get:

$$m_{amp} = m_o + 2.5 \log(\left|(1-\kappa)^2 - \gamma^2\right|) \tag{4.28}$$

in which, m_{amp} is the observed magnitude, and m_o is the apparent magnitude of the supernova in the absence of the lensing. We can further write m_o in terms of the

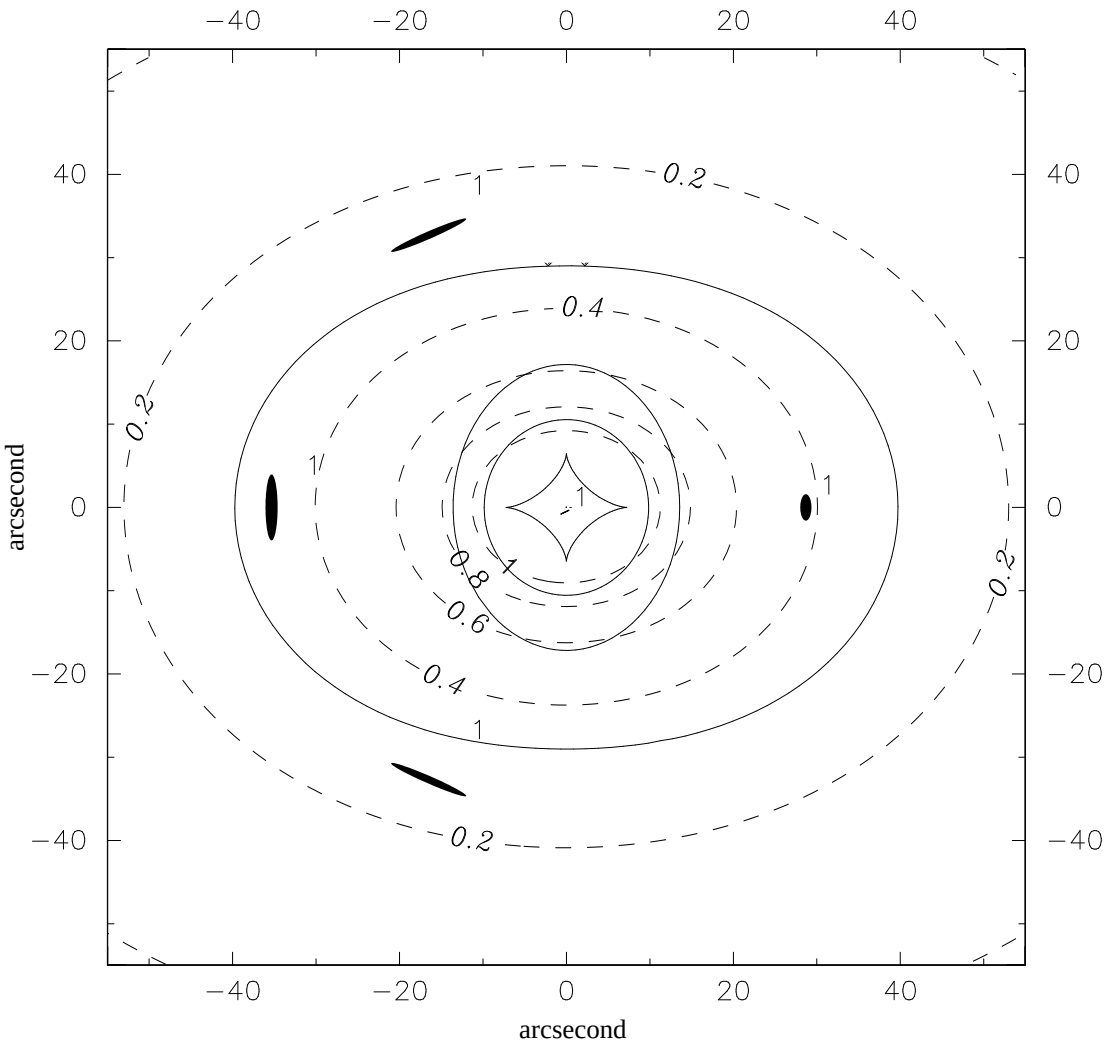


Figure 4.2: Multiple images produced by a $1.0 \times 10^{14} h^{-1} M_{\odot}$ halo with ellipticity $\epsilon = 0.1$. Dashed lines are the contours with constant surface density and the solid lines are the critical and caustic lines. Redshifts of deflector and source are 0.2 and 1.0, respectively (courtesy of Golse & Kneib).

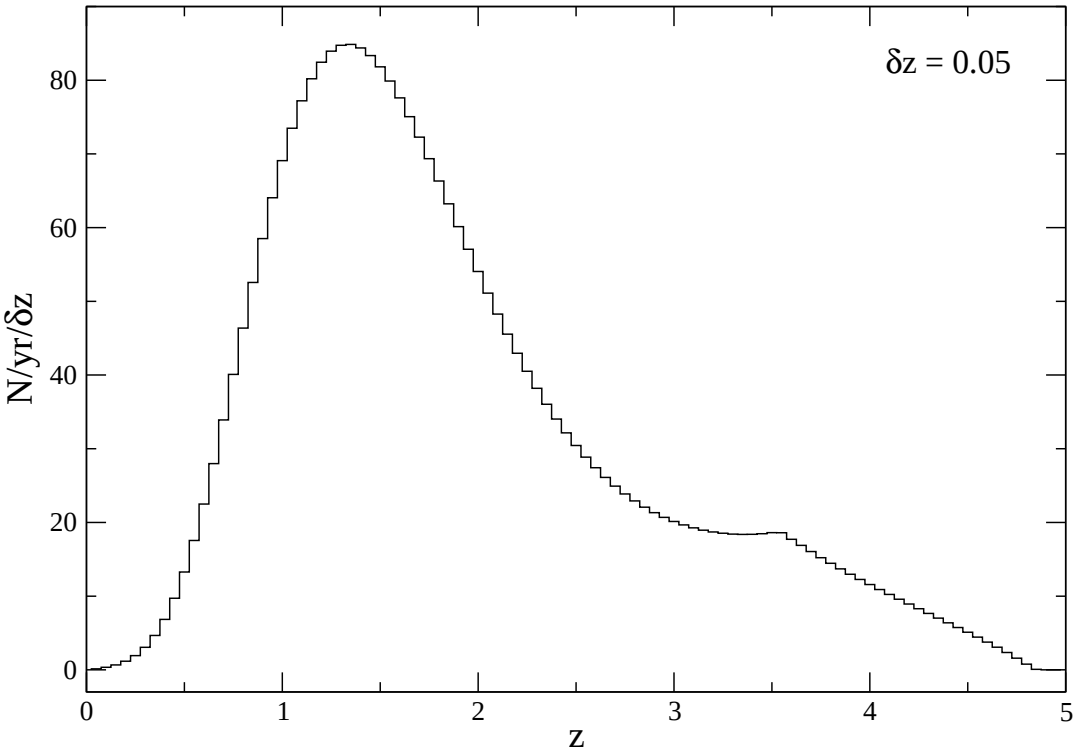


Figure 4.3: Rates of type Ia supernovae per squared degree in intervalls of $\delta z = 0.05$. Dilution factor of $1 + z$ is taken into account (courtesy of Gunnarsson & Goobar).

absolute magnitude M_{abs} of the supernova and rewrite the detection criterion as

$$\left((1-\kappa)^2-\gamma^2\right) D_L^2(z_s) \leqslant 10^{\left(\frac{m_{limit}-M_{abs}+5}{2.5}\right)} \tag{4.29}$$

where $D_L(z_s)$ is the luminosity distance of the supernova at redshift z_s. The absolute magnitude of type Ia SNe has a very narrow Gaussian distribution around $M_{abs} = -19.16$ at a confidence level of 89% (Richardson et al., 2002). Here, we assume that the supernova is detected as soon as its absolute magnitude becomes brighter than $M_{abs} = -18$.

We take the deflecting halo to be at redshifts $z_s = 0.2$, 0.5, and 1.0, and with virial masses of $m_{d1} = 1.0 \times 10^{12} h^{-1} M_\odot$ and $m_{d2} = 1.0 \times 10^{14} M_\odot h^{-1}$. Concentration parameter c, overdensity δ_c, and virial radius r_{200} (in units of $Kpch^{-1}$) for each case are given in Table 4.1.

The field of view is taken to be the spatial angle subtending the virial area of the halo. By breaking the projected halo into pixels with the angular size of δx_1 and δx_2 (which are taken to be smaller than the angular resolution of the observation, Figure 4.4), we calculate the amplification across the halo and hence, find the number of observable supernovae in redshift shells with the width of $\delta z = 0.05$. We find the corresponding (spatial angular) element $\delta\beta_1 \times \delta\beta_2$ in the area behind the halo (in redshift space) where the supernovae are bright enough to be detected. Assuming we

$\mathbf{m_d}$	$1.0 \times 10^{12} h^{-1} M_\odot$			$1.0 \times 10^{14} h^{-1} M_\odot$		
$\mathbf{z_d}$	$\mathbf{r_{200}}$	$\boldsymbol{\delta_c}$	**c**	$\mathbf{r_{200}}$	$\boldsymbol{\delta_c}$	**c**
0.2	152.61	38468.6	9.40	708.36	15741.7	6.46
0.5	136.24	33096.0	8.83	632.38	14426.7	6.22
1.0	111.79	25118.2	7.87	518.88	12086.5	5.77

Table 4.1: NFW halo parameters for the two halo masses m_d at the given redshifts z_d used in this chapter.

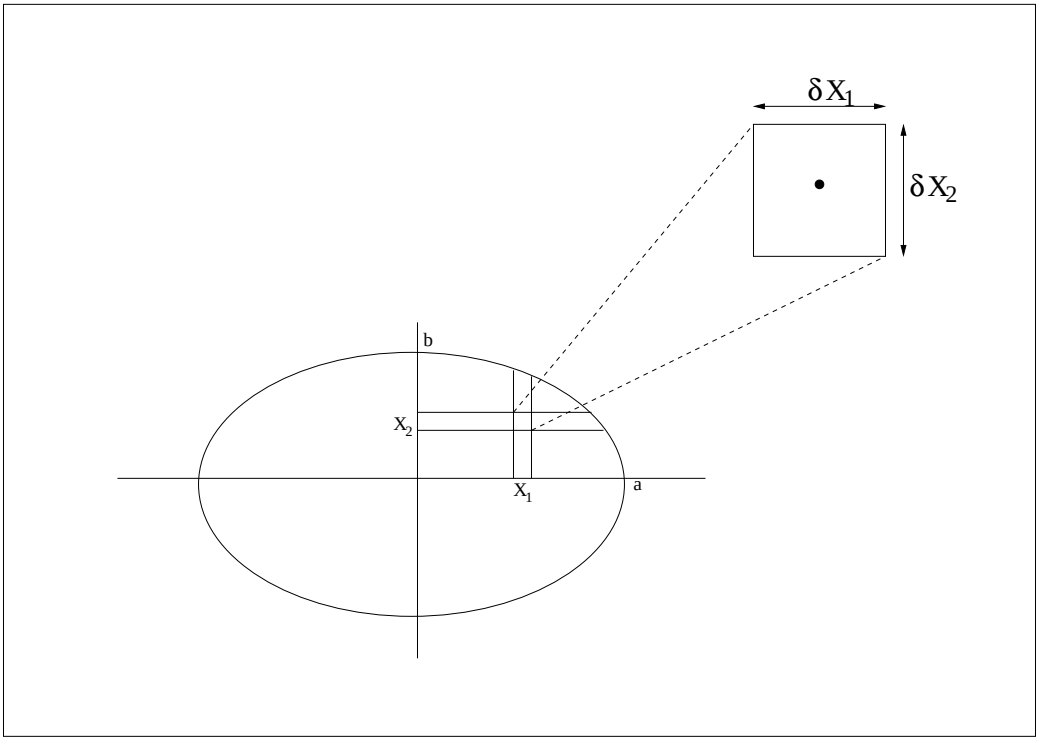


Figure 4.4: This figure shows how the projected deflector is 'pixellated' in order to calculate the observable area behind the halo. Each pixel has dimensions of $\delta\omega \times \delta\omega$ with $\delta\omega$ being (smaller than) the angular resolution of the observation.

can arbitrarily minimize δx_1 and δx_2 , we have

$$\delta\beta_1 \times \delta\beta_2 = \left|\frac{\partial \boldsymbol{\beta}}{\partial \boldsymbol{x}}\right| \delta x_1 \times \delta x_2 \tag{4.30}$$

where $\left|\frac{\partial \boldsymbol{\beta}}{\partial \boldsymbol{x}}\right|$ is the Jaccobian determinant.

The reader can refer to the Appendix B for the derivation of the Jaccobian. The gain factor, defined as the ratio of the number of observable lensed supernovae over the number of observable supernovae in the absence of lensing ($N_{lensed}/N_{NoLensing}$) can be calculated by integrating over the predicted rates of both cases across the whole observable area (Fig. 4.1) for any given lensing configuration, considering the ellipticity ϵ.

4.5 Results and Discussion

First, we consider the effect of ellipticity in the number rate of SN Ia in every redshift bin $\delta z = 0.05$. Upper panels of Figures 4.5 (m_{d1}) and 4.6 (m_{d2}) show the number of expected supernovae per year occuring in the redshift bins. We present the results for $\epsilon = 0.0$ and $\epsilon = 0.2$ with the deflecting halo at redshifts $z_d = 0.2$, 0.5, and 1.0. The survey magnitude is assumed to be $m_{lim} = 27$. The number rate peaks at around $z = 1.3$ as expected (see Fig. 4.3) and dies off rapidly beyond that. It can be seen that the farther the deflector, the slightly higher the slope of the curves up to $z = 1.3$ as a result of higher number of supernovae observed in front of the deflector.

Middle and lower panels in Figures 4.5 and 4.6 show the cumulative number rates and the gains, respectively. The dominance of amplification bias as a result of the narrowing of the field in a region immediately behind the deflectors at the assumed redshifts is clear, as the gains fall below 1. Beyond that region amplification takes over and more (lensed) supernovae are observed.

In the absence of an intercepting halo, the number rate of the survey drops to zero at the redshift limit of the survey. With the deflecting halo present, the observed

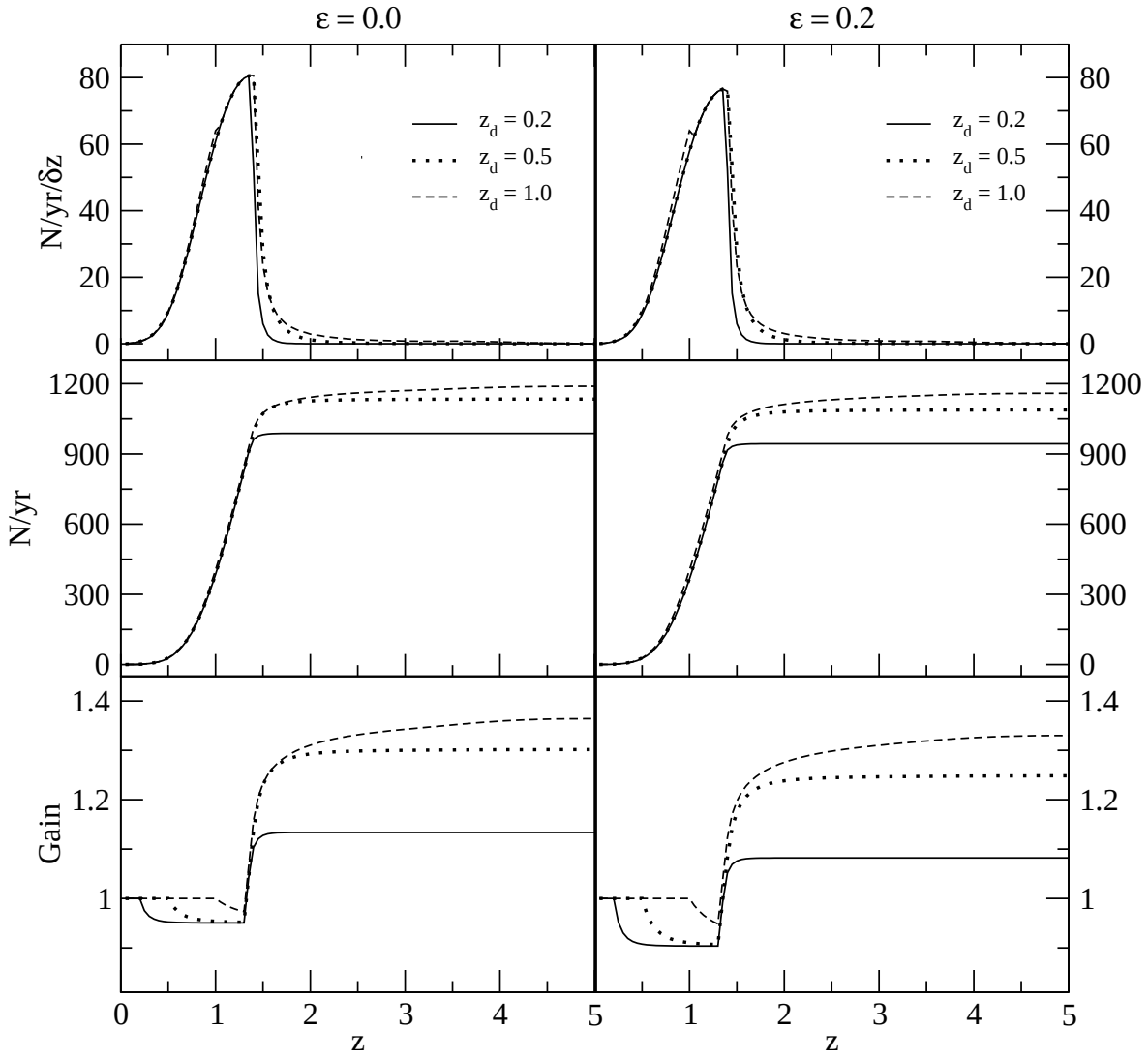


Figure 4.5: Rates of observed supernovae Ia per redshift bin $\delta_z = 0.05$ (upper panel), commulative rate (middle panel), and the lensing gain (lower panel) for a deflecting halo of mass $m_d = 1.0 \times 10^{12} h^{-1} M_\odot$ at redshifts of $z_d = 0.2$, 0.5, and 1.0 with ellipticities $\epsilon = 0.1$ and 0.2.

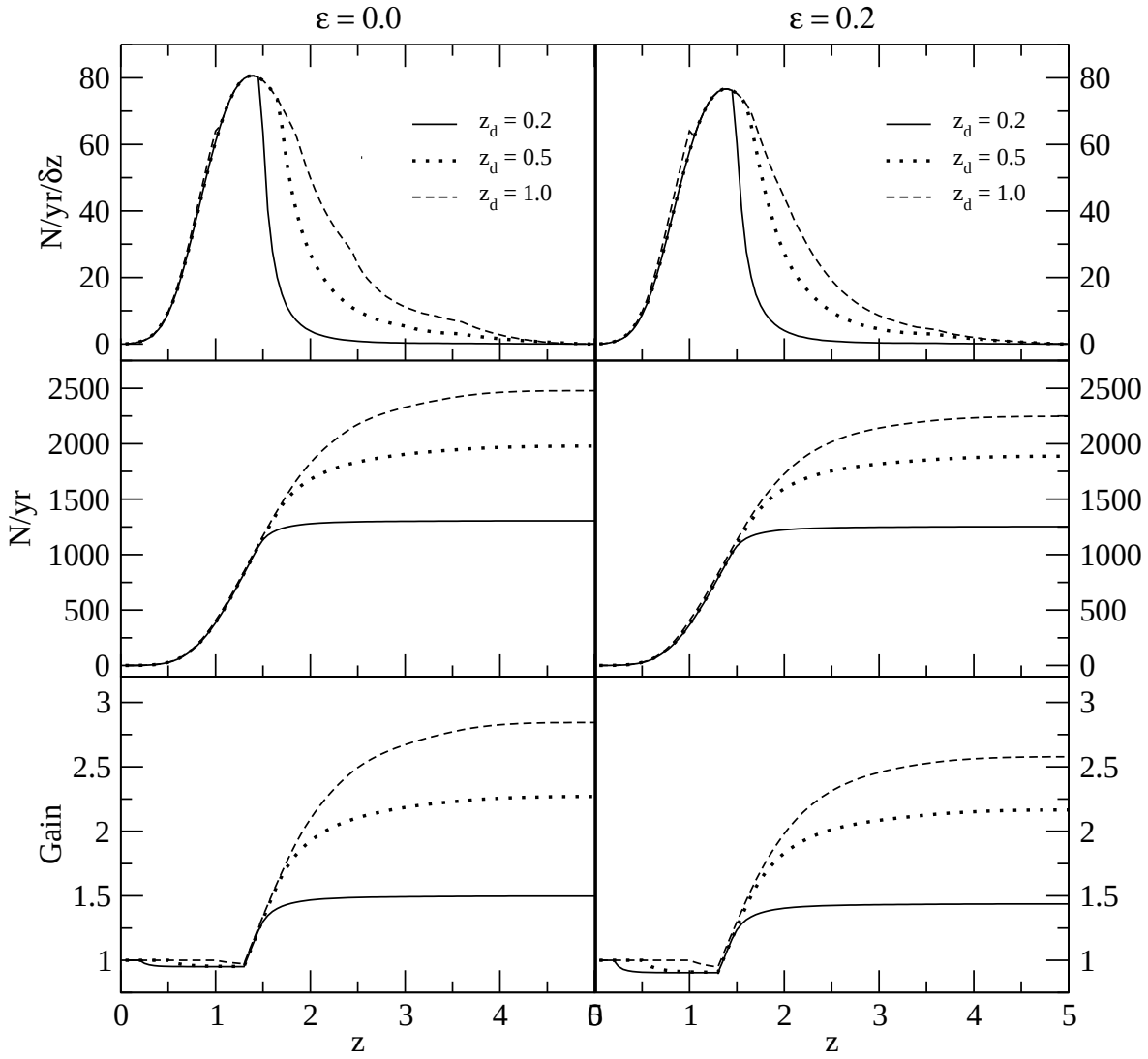


Figure 4.6: Same as Figure 5, with $m_d = 1.0 \times 10^{14} M_\odot h^{-1}$.

rate goes to zero at a higher redshift. This can be seen in figures 4.7 (m_{d1}) and 4.8 (m_{d2}) where the deflector is at redshift $z_d = 0.5$ and the survey magnitude limit is $m_{lim} = 27$. The three upper panels depict the expected rates for lensing and no-lensing scenarios for ellipticities $\epsilon = 0.0$, 0.1, and 0.2. The number rates per redshift bin (left) and the cumulative rate (right) are given. The reader can readily notice the effect of bias behind the halo. With the galactic size halo m_{d1}, the survey can detect supernovae up to redshift $z \sim 3$ (Fig. 4.7). This limit increases to $z \sim 5$ (Fig. 4.8) for the cluster-size halo m_{d2}.

The lowest panel in these two figures show the relative difference of the cases with $\epsilon = 0.1$ and $\epsilon = 0.2$ with respect to $\epsilon = 0.0$. The 2 curves do not show significant difference for the redshift bins in front of the halo. In the regime behind the halo, the difference becomes remarkable: it increases up to redshift $z = 1.4$ for m_{d1} and $z = 1.7$ for m_{d2}. The difference doesn't vary remarkably beyond the maximum point.

To further see how ellipticity changes the expected rate of observed supernovae we put the result of our calculations for different ellipticities for a given range of magnitude limits on the same plot. Figure 4.9 shows the number rate of observed type Ia supernovae (upper panel) for ellipticities $\epsilon = 0.1$ and $\epsilon = 0.2$ together with their relative difference with respect to the case with no ellipticity (lower panel). Both halo masses, m_{d1} and m_{d2} are at redshift $z_d = 0.2$. Figures 4.10 and 4.11 show the results of the same calculations with halos at redshifts $z_d = 0.5$ and $z_d = 1.0$, respectively. The number rates in each figure increase smoothly up to the magnitude limit at which the survey is deep enough to detect the supernovae as far as the halo itself, e.g, $m_{lim} = 22.4$ for a concordance cosmology of (Ω_m, Ω_{Lambda}, h_{100}) = (0.3, 0.7, 0.67). From that point on the rates increase very rapidly as the magnitude limit goes up. That is caused by the halo lensing and hence amplifying the supernovae which would otherwise be too dim to be observed. The relative differences depicted in these figures show that even at a magnitude limit of 25, effect of ellipticity cannot be ignored as it significantly changes the number/percentage of the observed supernovae;

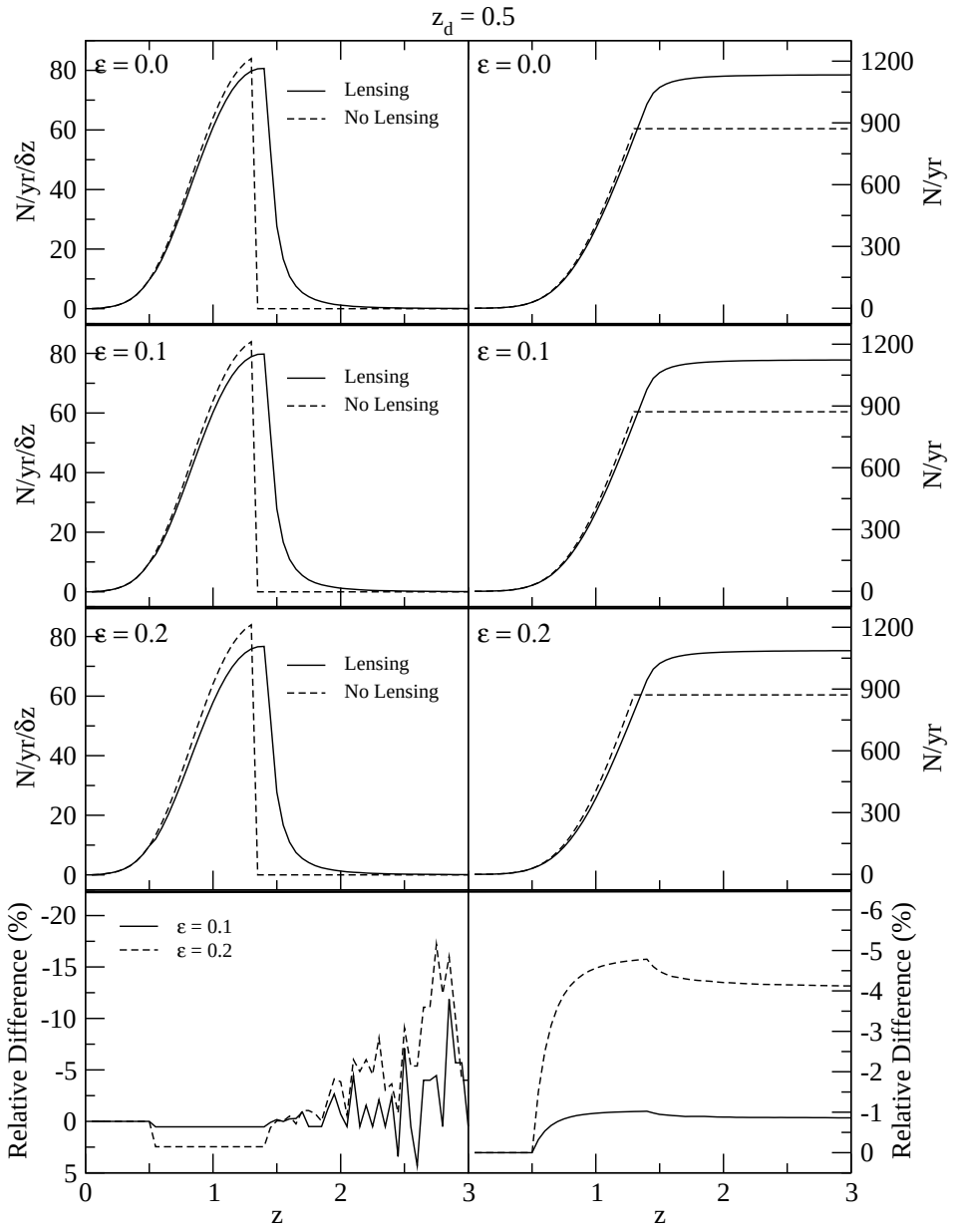


Figure 4.7: In this figure the 3 upper panels show observed rates of lensed (solid line) and unlensed (dash line) for three different ellipticies $\epsilon = 0.0$, 0.1, and 0.2. The deflecting halo has a mass of $m_d = 1.0 \times 10^{12} h^{-1} M_\odot$ and is located at redshift $z_s = 0.5$. The lowermost panel depicts the relative difference of $\epsilon = 0.1$ (solid line) and $\epsilon = 0.2$ (dash line) with respect to $\epsilon = 0.0$.

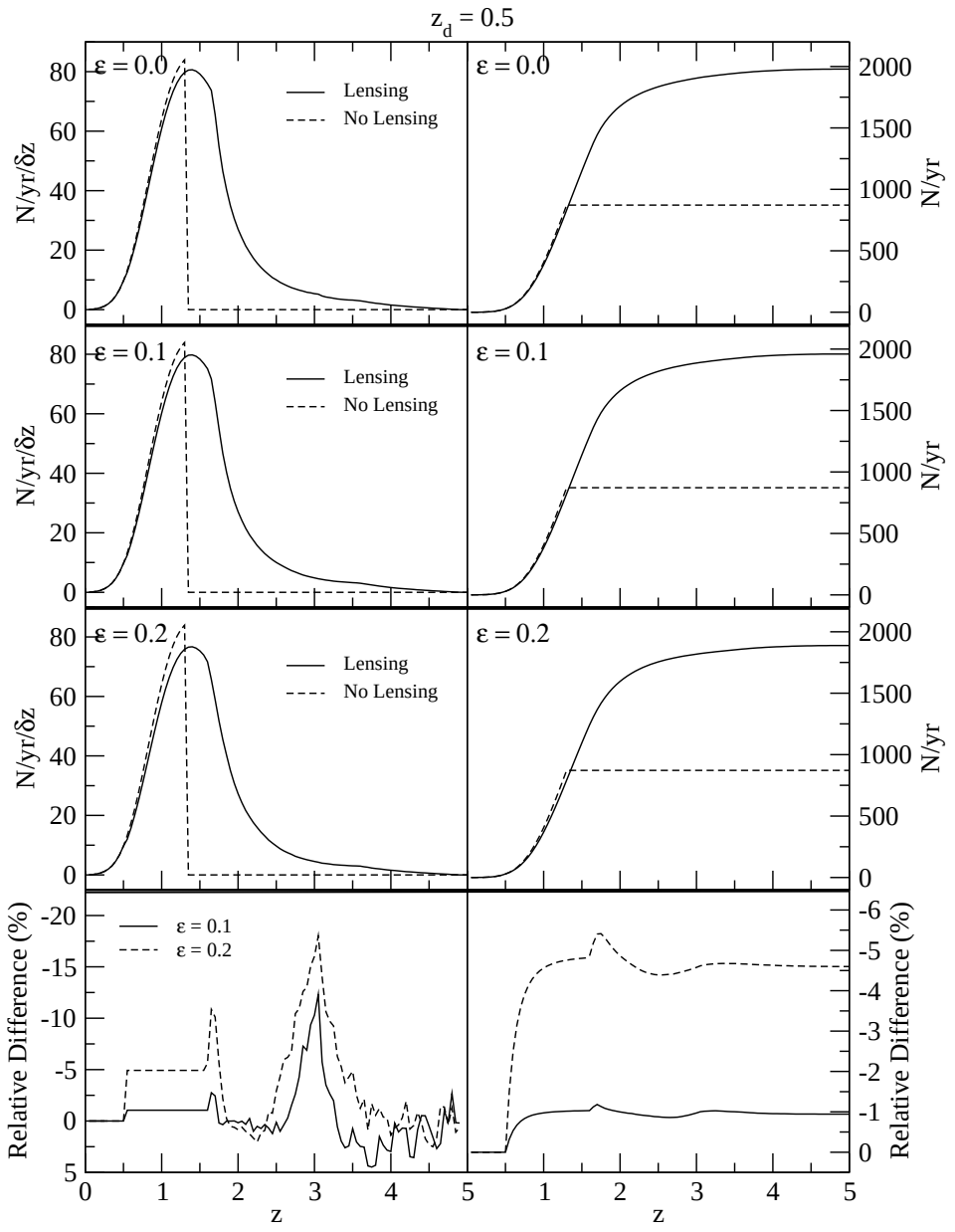


Figure 4.8: Same as Figure 7, with $m_d = 1.0 \times 10^{14} M_{\odot} h^{-1}$.

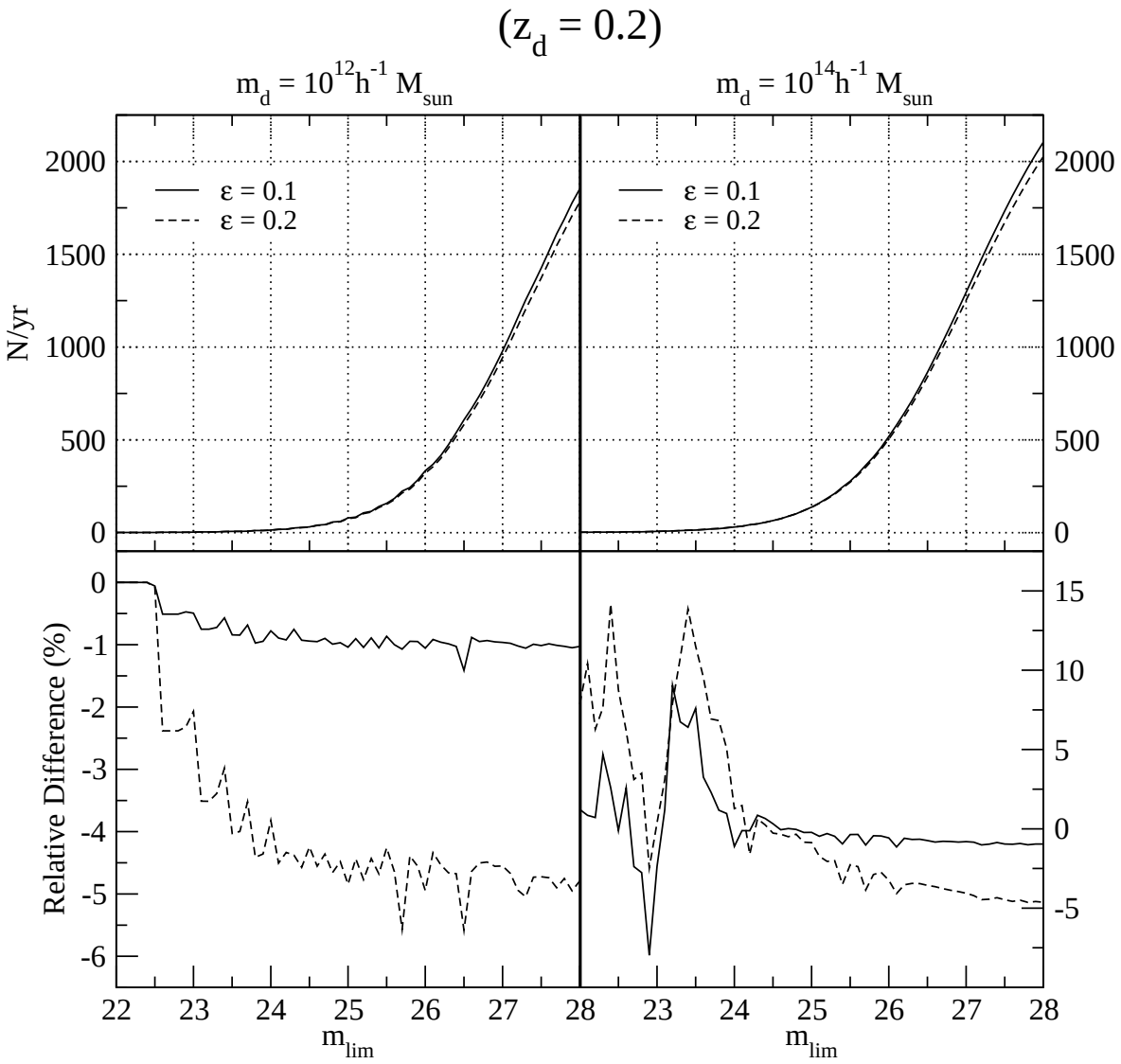


Figure 4.9: Rates of observed supernovae Ia as a function of survey magnitude limit m (upper panel). Results are shown for halo masses $m_d = 1.0 \times 10^{12} h^{-1} M_\odot$ and $m_d = 1.0 \times 10^{14} h^{-1} M_\odot$ with ellipticities $\epsilon = 0.1$ and 0.2. The halo is at redshift $z_d = 0.2$. The relative difference of cases with $\epsilon = 0.1$ and 0.2 with respect to $\epsilon = 0.0$ is given in the lower panel.

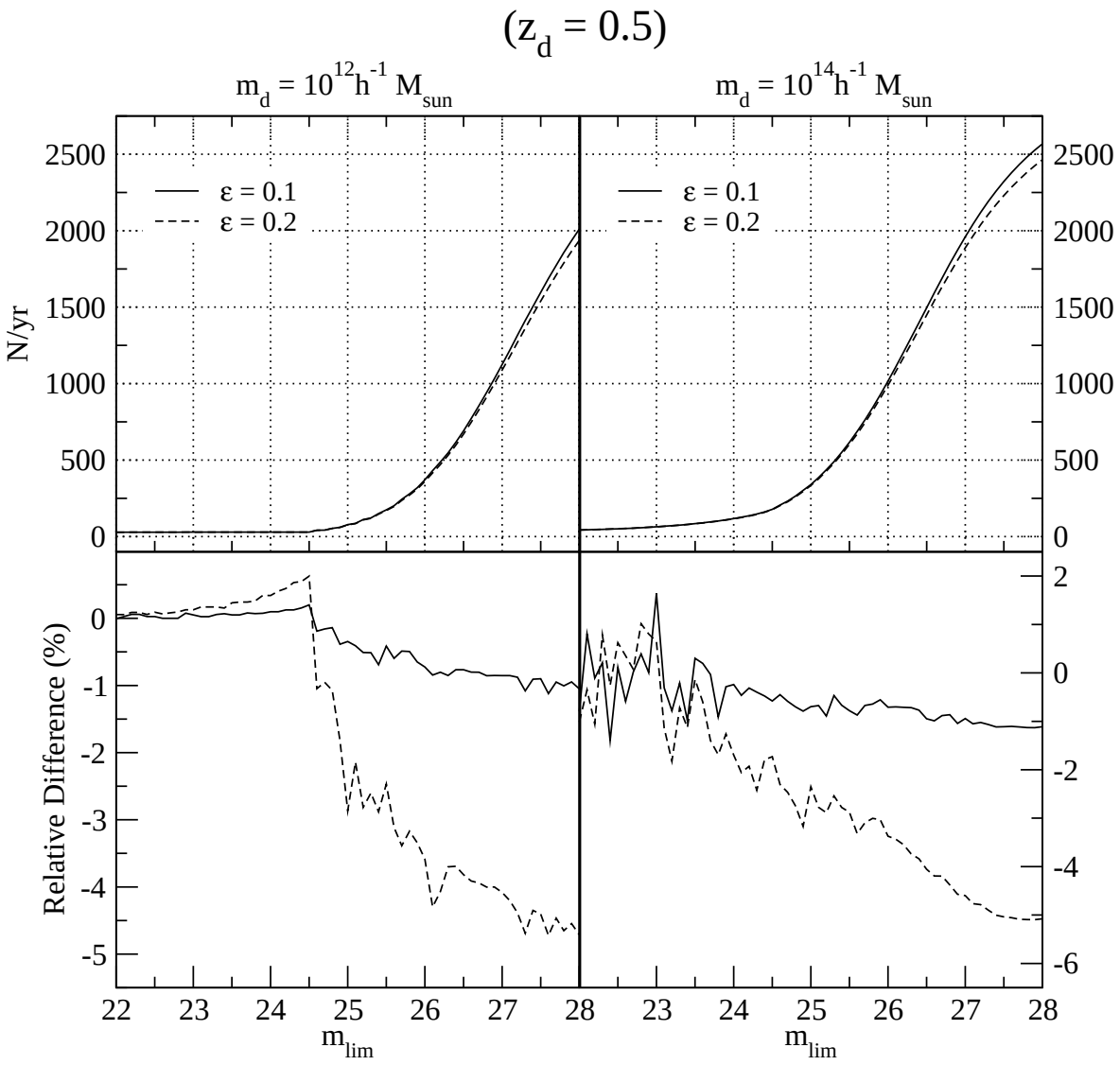


Figure 4.10: Same as Fig. 9 with $z_d = 0.5$.

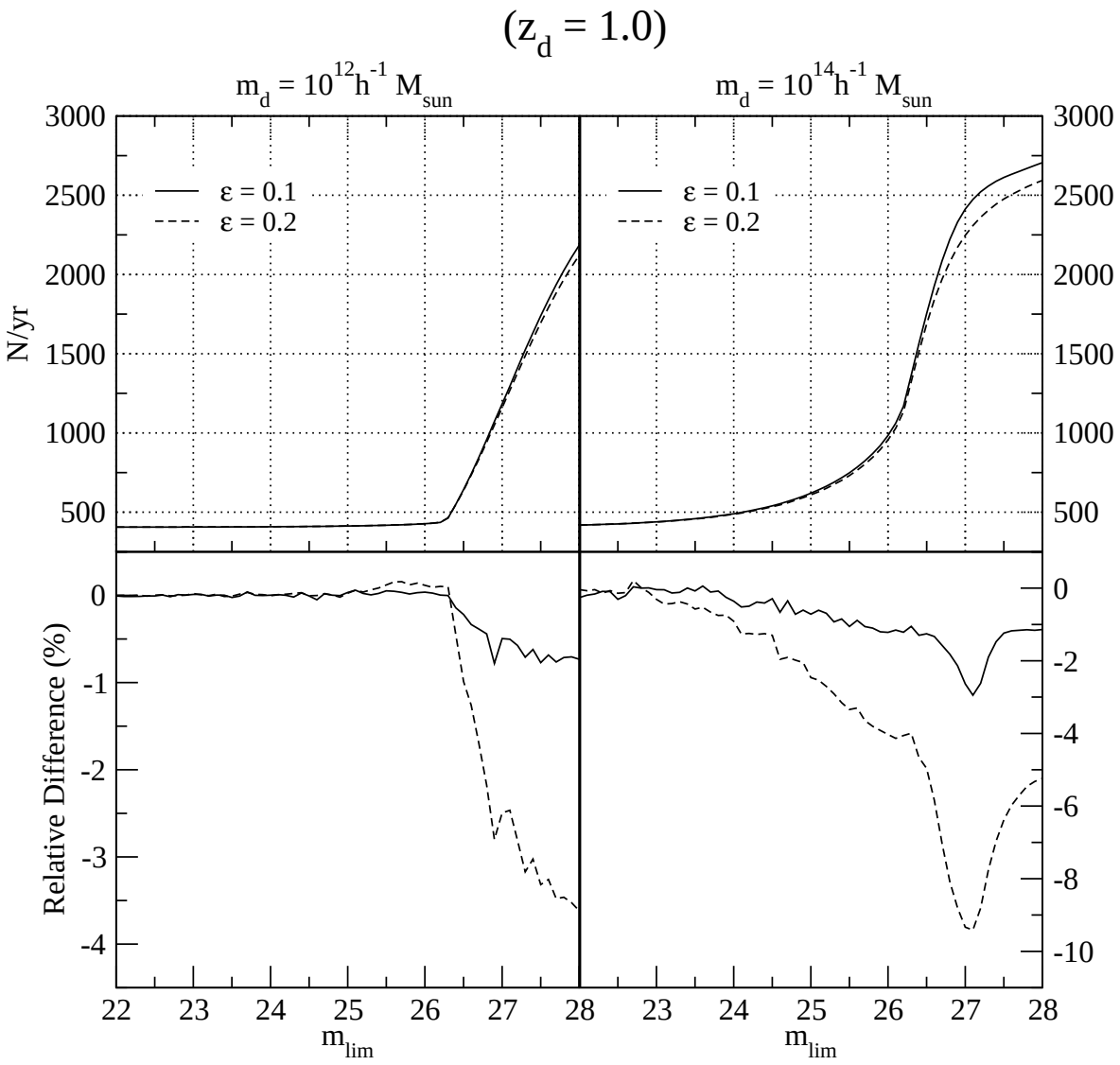


Figure 4.11: Same as Fig. 9 with $z_d = 1.0$.

for instance, the relative difference for $\epsilon = 0.2$ with deflecting halo m_{d2} at redshift $z_d = 1.0$ (Fig. 11) exceeds 9% for the magnitude limit of $m_{lim} = 27$.

4.6 Conclusion

Aiming behind massive halos seem to be a good way to enhance the high-redshift supernovae surveys. The commulative gains of such surveys seem insignificant at low redshifts ($z_s < 0.2$) but the results are remarkable at higher redshifts. For deep observations where $m_{lim} > 25$, the geometry of the intervening halo cannot be ignored. We have shown that introducing ellipticity in the (gravitational potential of) the mass distribution of a deflecting halo (here, for a galactic halo of mass $1.0 \times 10^{12} M_{\odot} h^{-1}$ as well as a middle-size cluster of galaxies with a mass of $1.0 \times 10^{14} M_{\odot} h^{-1}$) can affect the rate of observed supernovae by a few percent. It was shown that the farther the supernova survey probes, the more significant the effects of introduced ellipticity become.

It should be noted that this work does not involve a broad range of mass profiles for the halos (although we specify that the survey is limited to the virial area of the halo), nor does it address the much needed k-correction. Our calculations are actually an oversimplification due to the fact that a large, massive halo like a galaxy cluster has substructure which consists of the member galaxies, as well as large clouds of gas. A more sophisticated lens model with ellipticity should be employed to calculate the number rate of observed supernovae.

Chapter 5

Last Words

In this work we showed how microlensing by a single stellar-size deflector can distort the light curves and spectral lines of type Ia supernovae. These effects occur with a very low probability, hence they cannot be observed but through a survey detecting large number of supernovae, typically beyond 10,000 SNe per year. Proposed deep surveys like ALPACA (Corasanity et al, 2006) which are expected to detect such large number of supernovae will provide us with the opportunity to observe these effects.

We also presented the effects of introducing ellipticity in the structure of intervening massive halos (as macrolenses) on the rate of observed SNe Ia. At the time supernovae surveys do not reach high-enough redshifts in order for ellipticity to remarkably change their outcome. The intrinsic ellipticity of the foreground galaxies is too big to be ignored, and deep surveys of future will be affected by this inevitable fact.

As mentioned before, gravitational lensing manifests itself as a noise in any deep supernova survey. It compromises the use of supernovae as standard candles at high redshifts although the lensing-induced noise lies just beneath the estimate of supernova intrinsic noise (Holz, 1998). Although the effects introduced by lensing don't seem to be corrected on a case-by-case basis, it can be overcome by employing statistical models and predictions. Therefore, the results of any high-redshift supernova survey such as ACS/GOODS or SNAP (Riess, 2002) should be refined otherwise they could be compromised.

The subject of gravitational lensing is now a mature discipline, with a solid place in astronomy. The robust mass measures provided by lensing are one of the key reasons for having confidence in the standard model of structure formation. For the future, things are more challenging: the next set of interesting questions requires the measurement of small effects with non-trivial systematics. Here, the real question

will be whether lensing can overcome these problems rapidly enough that it becomes the most precise probe of the cosmological parameters, in particular the equation of state of the vacuum energy as well as its evolution.

Bibliography

Allen, C. W. 1973, Astrophysical Quantities (London: Athone)

Angonin, M., et al. 1990, A & A, 233, L5

Arnett, D. 1982, ApJ, 253, 785

Arnett, D. 1996, Supernovae and Nucleosynthesis (Princeton: Princeton University Press)

Astier, P., et al. 2006, A & A, 447, 31

Bartelmann, M. 1996, A & A, 313, 697

Beals, C. 1929, MNRAS, 90, 202

Bourassa, R. R., Kantowski, R., & Norton T. D. 1973, ApJ, 185, 747

Bourassa, R. R.,& kantowski, R. 1974, ApJ, 195, 13

Bourassa, R. R.,& kantowski, R. 1976, ApJ, 205, 674

Branch, D., et al. 2003, AJ, 126, 1489

Branch, D., et al. 2005, PASP, 117. 545

Chang, K., & Refsdal, S. 1984, A & A, 132, 168

Claret, A., Díaz-Corovés, J., & Gimémez, A. 1995, A & A, 114, 247

Cooke, J. H., & Kantowski, R. 1975, ApJ, 195, L11

Corasanity, P. S., et al. 2006, MNRAS, 369, 798

Dahlén, T., & Fransson, C. 1999, A & A, 350, 349

Fisher, A. 2000, PhD thesis, University of Oklahoma

Gal-Yam, A., Maoz, D., & Sharon, K. 2002, MNRAS, 332, 37

Golse, G., & Kneib, J. P. 2002, A & A, 390, 821

Goobar, A., & Perlmutter. S. 1995, ApJ, 450, 14

Gunnarsson, C., & Goobar, A. 2003, A & A, 405, 859

Han, C., & Gould, A. 2003, ApJ, 592, 172

Hernquist, L. 1990, ApJ, 356, 359

Höflich, P. 1990, A & A, 229, 191

Holz, D. 1998, ApJL, L506, 1998

Holz, D. 2001, ApJ, L71, 2001

Hutsemékers, D., & Surdej, J. 1990, ApJ, 361, 367

Hutsemékers, D., Surdej, J., & Van Drom, E. 1992 Lecture Notes in Physics, Gravitational Lenses, ed. R. Kayser et al. (Berlin: Springer-Verlag)

Hutsemékers, D. 1993, A & A, 280, 435

Jeffery, D. 1999, preprint (astro-ph/9907015)

Jeffery, D., & Branch, D. 1990, Jerusalem Winter School for Theoretical Physics, Vol. 6, ed. J. C. Wheeler, S. Weinberg (Singapore: World Scientific)

Jeffery, D. 1993, ApJ, 415, 734

Kantowski, R., Vaughan, T., & Branch, D. 1995, ApJ, 447, 35

Kantowski, R. 2003, PRD, 68, 123516

Kayser, R., Refsdal, S., & Stabell, R. 1986, A & A, 166, 36

Kochanek, C. S., & White, M. 2001, ApJ, 559, 531

Kolatt, T. S., & Bartelmann, M. 1998, MNRAS, 296, 763

Linder, E., Schneider, P., & Wagoner, R. V. 1988, ApJ, 324, 786

Mao, S., & Witt, H. J. 1998, MNRAS, 300, 1041

Meneghetti, M., Bartelmann, M.,& Moscardini L. 2003, MNRAS, 340, 105

Mihalas, D. 1978, Stellar Atmospheres (San Francisco: Freeman)

Myers, S. T., et al. 1995, ApJ, 447, 15

Navarro, J. F., Frenk, C.S., & White, S. D. M. 1995, MNRAS, 275, 720

Navarro, J. F., Frenk, C.S., & White, S. D. M. 1996, ApJ, 462, 563

Navarro, J. F., Frenk, C.S., & White, S. D. M. 1997, ApJ, 490, 493

Nomoto, K., Thielemann, F., & Yokoi, K. 1984, ApJ, 286, 644

Oguri, M., Suto, Y., & Turner, E. L. 2003, ApJ, 583, 584

Paczyński, B. 1986a, ApJ, 301, 503

Paczyński, B. 1986b, ApJ, 304, 1

Perlmutter, S., et al. 1999, ApJ, 517, 565

Perlmutter, S., & Schmidt B. P. 2003, Lecture Notes in Physics, ed. K. Weiler (Berlin: Springer-Verlag)

Press, W. H., & Gunn, J. E. 1973, ApJ, 185, 397

Rauch, K. P. 1991, ApJ, 374, 83

Richardson, D., et al. 2002, AJ, 123, 745

Richardson, D., Branch, D., & Baron, E. 2006, AJ, 2006, 131, 4

Riess, A., Press, W. H., & Kirshner, R. P. 1995, ApJ, 438, L17

Riess, A., et al. 2002, IAU Circ. 8012

Saini, T. D., Raychaudhary, S., & Shchekinov, Y. A. 2000, A & A, 363, 349

Shapiro, I. I. 1964, PRL, 13, 789

Schmidt, B. P., et al. 1998, ApJ, 507, 46

Schneider, P., & Wagoner, R. V. 1987, ApJ, 314, 154

Schneider, P., Ehlers, J., & Falco, E. E. 1992, Gravitational Lenses (Berlin: Springer-Verlag)

Smail, I., et al. 2002, MNRAS, 331, 495

Sobolev, V. V. 1958, Theoretical Astrophysics, ed. V A. Ambartsumyan (London: Pergamon)

Subramanian, K., & Cowling, S. A. 1986, MNRAS, 219, 333

Sullivan, M., et al. 2000, MNRAS, 319, 549

Sumi, T., et al. 2003, ApJ, 591, 204

Sumi, T., et al. 2004, MNRAS, 348, 1439

Udalski, A. 2003, ACTAA, 53, 291 (data taken from NOOS & EWS of OGLE III, http://www.astrouw.edu.pl/∼ogle/)

Witt, H. J., & Mao, S. 1994, ApJ, 430, 505

Wright, C. O., & Brainerd, T. G. 2000, ApJ, 534, 34

Wyithe, J. S. B., & Turner, E. L. 2002, ApJ, 567, 18

Zakharov, A. F., Popović, L. Č., & Jovanović, P. 2004, A & A, 420, 881

Appendix A

Probability of Distortion in a Lensed Light Curve

In this appendix we compute the probability that a source, followed for a period T, impacts a point deflector with a reduced impact parameter less than $u \equiv b/R_E$ and simultaneously moves at least a distance b during the period T. Such a time dependent impact will cause a change in the amplification of 10%-50% depending on the actual impact. The idea here is to estimate the chance of seeing a distortion in the light curve of a SN whose life time is $T_{SN} \sim 200$ days.

We start with a number density N_d of mass m deflectors (located at a distance D_d from the observer) moving with relative transverse velocities distributed according to:

$$\frac{dN_d}{dv} = N_d(D_d)\frac{v}{v_{rms}^2}e^{-v^2/2v_{rms}^2}. \tag{A.1}$$

The probability of one of these moving deflectors impacting the line of sight to a source at D_s with a reduced impact parameter $\leq u$ and moving a reduced distance $\geq u$ during a period T is:

$$\Delta Prob(u,T) = \int_0^{D_s} dD_d \int_{u\,R_E/T}^{\infty} dv N_d(D_d)(\pi u^2 R_E^2 + 2uR_E v\,T)\frac{v}{v_{rms}^2}e^{-v^2/2v_{rms}^2}. \tag{A.2}$$

The integrand is the sum over areas represented in Figure A.1. The velocity integral can be done easily, and if the deflectors are effectively confined to a plane, the result can be written as

$$\Delta Prob(u,\xi) = \frac{4G}{c^2}\,\Sigma\, D\, u^2 \left\{ (\pi+2)e^{-\xi^2/2} + \sqrt{2\pi}\frac{Erfc(\xi/\sqrt{2})}{\xi} \right\}, \tag{A.3}$$

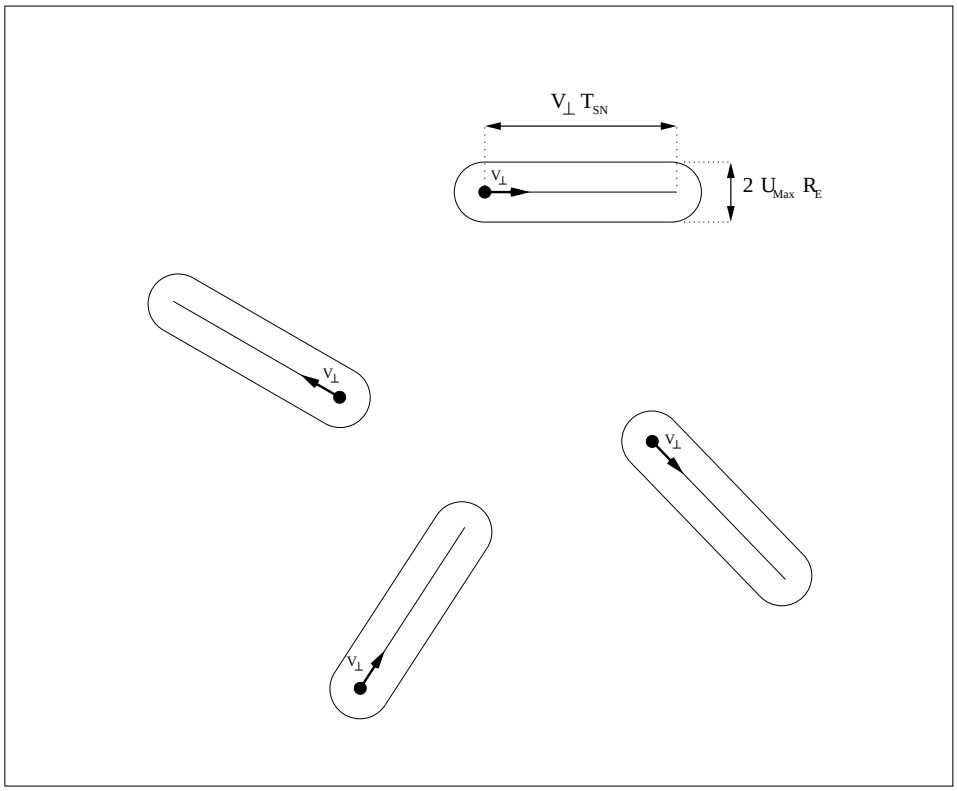


Figure A.1: Area on the deflector plane within which a microlens would be close enough to a luminous SNe Ia to cause significant changes in its lightcurve.

where

$$\xi \equiv \frac{uR_E}{v_{rms}T} = u\,\frac{T_{rms}}{T}, \tag{A.4}$$

Σ is the projected surface mass density

$$\Sigma \equiv \int_0^{D_s} m\, N_d(D_d) dD_d, \tag{A.5}$$

and $Erfc$ is an error function.

The characteristic crossing time for microlensing is defined by $T_{rms} = R_E/v_{rms} = \sqrt{2r_S D}/v_{rms}$ (see § 3 for definitions) which for Galaxy bulge-bulge lensing is about 10 days (Udalski, 2003). For a similar galaxy at redshift $z = 0.05$ lensing a distant SN through its bulge, the reduced distance D is increased by a factor of $\sim 2.7 \times 10^5$ [see § 3.3 and Han & Gould (2003)] and hence T_{rms} increases to $\sim$ 5,200 days. If $u \sim 0.05$ and $T = T_{SN} \sim 200$ days, then $\xi \sim 1.3$ and $\Delta Prob(0.05, 1.3) \sim 1.7 \times 10^{-3}$. This particular probability falls off by at least an order of magnitude when $u < 0.01$ or $u > 0.15$.

Appendix B

Lensing Equation for Elliptical NFW Haloes

Here we derive the lensing equation for an elliptical NFW halo with ellipticity of ϵ introduced in its 2-dimensional potential, and proceed to calculate Jaccobian $\frac{\partial \boldsymbol{\beta}}{\partial \boldsymbol{x}}$ needed to get the spatial angular element $\delta\beta_1 \times \delta\beta_2$ in the source frame.

Lensing Equation

Introducing the dimensionless coordinate system $\mathbf{x} = (x_1, x_2) = \mathbf{R}/r_s = \theta/\theta_s$, the lensing equation becomes

$$\begin{cases} \beta_1 &= \theta_s x_1 - \alpha_1 [x_1, x_2] \\ \beta_2 &= \theta_s x_2 - \alpha_2 [x_1, x_2] \end{cases} \tag{B.1}$$

Given the elliptical deflection angle of

$$\alpha_\epsilon(\mathbf{x}) = \begin{pmatrix} \dfrac{\partial \varphi_\epsilon}{\partial x_1} = \alpha(x_\epsilon)\sqrt{a_{1\epsilon}}\cos\phi_\epsilon \\ \dfrac{\partial \varphi_\epsilon}{\partial x_2} = \alpha(x_\epsilon)\sqrt{a_{2\epsilon}}\sin\phi_\epsilon \end{pmatrix} \tag{B.2}$$

and the deflection angle of α as

$$\boldsymbol{\alpha}(x) \;=\; \theta\,\frac{\overline{\Sigma}(x)}{\Sigma_{\rm crit}} \;=\; 4\kappa_s\,\frac{\theta}{x^2}g(x)\mathbf{e}_x \tag{B.3}$$

the lensing equation now reads

$$\begin{cases} \beta_1 &= \theta_s x_1 \left(1 - 4k_s\epsilon_1 \dfrac{g(x_\epsilon)}{x_\epsilon^2}\right) \\ \beta_2 &= \theta_s x_2 \left(1 - 4k_s\epsilon_2 \dfrac{g(x_\epsilon)}{x_\epsilon^2}\right) \end{cases} \tag{B.4}$$

Jaccobian

To calculate spatial angular element $\delta\beta_1 \times \delta\beta_2$ we use the Jaccobian equation

$$\delta\beta_1 \times \delta\beta_2 \;=\; \left|\frac{\partial \boldsymbol{\beta}}{\partial \boldsymbol{x}}\right| \delta x_1 \times \delta x_2 \;=\; \left|\frac{\partial \beta_1}{\partial x_1}.\frac{\partial \beta_2}{\partial x_2} - \frac{\partial \beta_1}{\partial x_2}.\frac{\partial \beta_2}{\partial x_1}\right| \delta x_1 \times \delta x_2 \tag{B.5}$$

Given Eq. B.4, we get:

$$\begin{cases} \dfrac{\partial \beta_1}{\partial x_1} &= \theta_s \left(1 - 4k_s a_{1\epsilon} G(x_\epsilon)\right) \theta_s x_1 \left(1 - 4k_s a_{1\epsilon} \dfrac{\partial G(x_\epsilon)}{\partial x_1}\right) \\ \dfrac{\partial \beta_2}{\partial x_1} &= \theta_s x_2 \left(1 - 4k_s a_{2\epsilon} \dfrac{\partial G(x_\epsilon)}{\partial x_1}\right) \\ \dfrac{\partial \beta_1}{\partial x_2} &= \theta_s x_1 \left(1 - 4k_s a_{1\epsilon} \dfrac{\partial G(x_\epsilon)}{\partial x_2}\right) \\ \dfrac{\partial \beta_2}{\partial x_2} &= \theta_s \left(1 - 4k_s a_{2\epsilon} G(x_\epsilon)\right) \theta_s x_2 \left(1 - 4k_s a_{2\epsilon} \dfrac{\partial G(x_\epsilon)}{\partial x_2}\right) \end{cases} \tag{B.6}$$

where function G is defined as

$$G(x_\epsilon) \equiv \frac{g(x_\epsilon)}{x_\epsilon^2} \tag{B.7}$$

and

$$\frac{g(x_\epsilon)}{x_\epsilon^2} = \begin{cases} \dfrac{x_\epsilon}{\left(1 - x_\epsilon^2\right)^{\frac{3}{2}}} \mathrm{arcch} \dfrac{1}{x_\epsilon} - \dfrac{\left(1 + x_\epsilon^2\right)}{2x_\epsilon \left(1 - x_\epsilon^2\right)} & (x_\epsilon < 1) \\ -\dfrac{1}{6} & (x_\epsilon = 1) \\ \dfrac{\left(1 + x_\epsilon^2\right)}{2x_\epsilon \left(1 - x_\epsilon^2\right)} - \dfrac{x_\epsilon}{\left(1 - x_\epsilon^2\right)^{\frac{3}{2}}} \arccos \dfrac{1}{x_\epsilon} & (x_\epsilon > 1). \end{cases} \tag{B.8}$$